

**SEVENTH FRAMEWORK PROGRAMME****Report on Y1 activities and new  
integration strategy****FP7-ICT-216863/ORC/R/PU/D15.1**

<b>Project Number:</b>	FP7-ICT-2007-1 216863
<b>Project Title:</b>	Building the Future Optical Network in Europe (BONE)
<b>Contractual Date of Deliverable:</b>	30/11/08
<b>Actual Date of Delivery:</b>	07/01/09
<b>Workpackage contributing to the Deliverable:</b>	WP15 : VCE Transmission Techniques
<b>Nature of the Deliverable</b>	R
<b>Dissemination level of Deliverable</b>	PU
<b>Editors:</b>	Partner / names
Periklis Petropoulos	ORC
Francesca Parmigiani	ORC
Juan Fernandez Palacios	TID
Giorgio Maria Tosi Beleffi	ISCOM
Salvador Sales	UPVLC
Jose Lazaro	UPC
Josep Fabrega	UPC
Francesco Matera	FUB
Nick Avlonitis	AIT
Marco Forzatti	ACREO/KTH
Antonis Bogris	UoA
Dimitrios Apostolopoulos	ICCS/NTUA
Michel Morvan	GET
Philippe Gravey	GET
Antonio Teixeira	IT



---

Rebecca Chandy	Ericsson
Yabin Ye	Huawei
Andrea Carena	POLITO

**Abstract:**

This deliverable reports the activities of the Virtual Centre of Excellence on Transmission Techniques, and the progress achieved during Year 1 of the project.

**Keyword list:** Optical communications, 100Gb/s transmission, coherent systems, regeneration, highly nonlinear fibres, semiconductor optical amplifiers, erbium doped fibre amplifiers, burst amplification, signal monitoring, Gigabit Ethernet, fibre Bragg gratings, reliability analysis

**Clarification:***Nature of the Deliverable*

R	Report
P	Prototype
D	Demonstrator
O	Other

*Dissemination level of Deliverable:*

PU	Public
PP	Restricted to other programme participants (including the Commission Services)
RE	Restricted to a group specified by the consortium (including the Commission Services)
CO	Confidential, only for members of the consortium (including the Commission Services)



## **Disclaimer**

*The information, documentation and figures available in this deliverable, is written by the BONE ("Building the Future Optical Network in Europe) – project consortium under EC co-financing contract FP7-ICT-216863 and does not necessarily reflect the views of the European Commission*



## Table of Contents

<b>CLARIFICATION:</b> .....	<b>2</b>
<i>NATURE OF THE DELIVERABLE</i> .....	2
<i>DISSEMINATION LEVEL OF DELIVERABLE:</i> .....	2
<b>DISCLAIMER</b> .....	<b>3</b>
<b>TABLE OF CONTENTS</b> .....	<b>4</b>
<b>1. EXECUTIVE SUMMARY</b> .....	<b>6</b>
<b>2. INTRODUCTION</b> .....	<b>7</b>
2.1 <i>OUTLINE OF THE REPORT</i> .....	8
<b>3. MANAGEMENT ACTIVITIES</b> .....	<b>9</b>
3.1 <i>WP TECHNICAL MEETINGS</i> .....	9
3.2 <i>VCE-T SURVEY OF AVAILABLE EXPERTISE AND FACILITIES</i> .....	10
3.3 <i>FOCUS GROUPS</i> .....	12
3.4 <i>QUANTIFIABLE MEASURES OF INTEGRATION</i> .....	12
<b>4. KEY ISSUES IN 100 GB/S TRANSMISSION</b> .....	<b>13</b>
4.1 <i>INTRODUCTION</i> .....	13
4.2 <i>SHORT REACH TRANSMISSION</i> .....	13
4.2.1 <i>Introduction</i> .....	13
4.2.2 <i>Transmitter and Receiver Issues</i> .....	14
4.2.3 <i>Results</i> .....	15
4.2.4 <i>Conclusions</i> .....	18
4.3 <i>LONG REACH TRANSMISSION</i> .....	19
4.3.1 <i>Objectives</i> .....	19
4.3.2 <i>Simulation Plan</i> .....	19
4.3.3 <i>PRELIMINARY RESULTS</i> .....	23
4.4 <i>REFERENCES</i> .....	30
<b>5. REGENERATION</b> .....	<b>32</b>
5.1 <i>FIBRE-BASED REGENERATION</i> .....	32
5.1.1 <i>Design of single channel OOK 2R regenerators</i> .....	32
5.1.2 <i>Multi channel OOK 2R regenerators</i> .....	41
5.1.3 <i>3R Regeneration OOK</i> .....	47
5.2 <i>SOA-BASED REGENERATION</i> .....	52
5.2.1 <i>SOA-based all-optical regeneration principle</i> .....	52
5.2.2 <i>Integrated SOA-MZIs 2R regenerators</i> .....	54
5.2.3 <i>GC-SOA format converter regenerator</i> .....	56
5.3 <i>ANALYSIS OF LONG-HAUL TRANSMISSION SYSTEM WITH PHASE-SENSITIVE AMPLIFIERS: BER PERFORMANCE ESTIMATION</i> .....	57
5.3.1 <i>Introduction</i> .....	57
5.3.2 <i>Theory</i> .....	58
5.3.3 <i>Semi-analytical results</i> .....	59
5.3.4 <i>Conclusions</i> .....	61
5.4 <i>REFERENCES</i> .....	61
<b>6. AMPLIFICATION IN TRANSMISSION</b> .....	<b>63</b>
6.1 <i>EXTENSION OF BLACK BOX MODEL OF EDFAS TO INCLUDE VARIATION OF THE EDF'S LENGTH</i> .....	63
6.1.1 <i>Introduction</i> .....	63
6.1.2 <i>Theoretical Modelling</i> .....	63
6.1.3 <i>Experimental Measurements and Theoretical Expression Verification</i> .....	65



6.1.4	References .....	67
<b>6.2</b>	<b>STATE OF THE ART ON BURSTY AMPLIFIED SYSTEMS .....</b>	<b>68</b>
6.2.1	References .....	69
<b>6.3</b>	<b>AMPLIFICATION IN DIFFERENT KINDS OF AMPLIFICATION SYSTEMS.....</b>	<b>70</b>
<b>7.</b>	<b>MONITORING.....</b>	<b>73</b>
7.1	<b>CHROMATIC-DISPERSION MONITORING BASED ON PM-AM CONVERSION .....</b>	<b>73</b>
7.1.1	Introduction.....	73
7.1.2	Principle.....	73
7.1.3	Theoretical Analysis.....	74
7.1.4	Experiment and Discussion.....	75
7.1.5	Conclusion .....	77
7.1.6	References .....	77
7.2	<b>EVOLUTION OF AN OPM PROTOTYPE FOR OSNR MEASUREMENTS.....</b>	<b>78</b>
7.2.1	Introduction.....	78
7.2.2	Status of the prototype.....	78
7.2.3	Introducing in-band OSNR measurement in the OPM prototype .....	79
7.2.4	References .....	82
<b>8.</b>	<b>OTHER TRANSMISSION-RELATED JOINT ACTIVITIES WITHIN BONE.....</b>	<b>83</b>
8.1	<b>POLARISATION-RELATED PHENOMENA IN FIBRE BRAGG GRATINGS .....</b>	<b>83</b>
8.1.1	Introduction.....	83
8.1.2	Influence of the grating parameters on the polarization properties of fiber Bragg gratings.....	83
8.1.3	Reduction of birefringence in fiber Bragg gratings by using a twisted fiber for inscription.....	85
8.1.4	Application of the study of the polarization properties to sensing of transversal loads. ....	85
8.1.5	References .....	86
8.2	<b>ALGORITHMS FOR TUNING AND CONTROLLING LOCAL WAVELENGTH IN COHERENT DETECTION OF MULTILEVEL PSK SIGNALS .....</b>	<b>87</b>
8.2.1	Introduction.....	87
8.2.2	Off-line .....	87
8.2.3	Digital Realtime .....	87
8.2.4	Analogue approach .....	88
8.2.5	References .....	97
8.3	<b>TRANSMISSION PERFORMANCE OF GBE TRANSMISSION IN WIDE AREA NETWORKS .....</b>	<b>97</b>
8.4	<b>RELIABILITY ANALYSIS OF OPTICAL MODULES FOR FUTURE OPTICAL TRANSMISSION NETWORKS.....</b>	<b>101</b>
8.4.1	Introduction.....	101
8.4.2	Reliability of optical PIN Receiver.....	102
8.4.3	Failure Mode Analysis .....	104
8.4.4	Network Reliability tests.....	105
8.4.5	Conclusion .....	105
8.4.6	References .....	105
<b>9.</b>	<b>CONCLUSIONS .....</b>	<b>106</b>
	<b>TABLE OF FIGURES .....</b>	<b>107</b>



## **1. Executive Summary**

This document provides a presentation of the activities of the Virtual Centre of Excellence in Transmission Techniques (VCE-T) during the first year of the BONE project. The report starts with an outline of the measures that have been taken centrally within the VCE in order to encourage integration among the partners. The technical activities of VCE-T have been centered around four Focus Groups which reflect research interests which are shared among several of the VCE-T partners. These Focus Groups relate to (a) key issues on 100 Gb/s transmission, (b) signal regeneration, (c) signal amplification and (d) signal monitoring. The four Sections that follow present in detail the work that has been carried out within these Focus Groups, whereas a separate Section is devoted to joint activities relating to transmission-related topics which are not covered within the Focus Groups.



## 2. Introduction

*Table 1: Acronyms of the VCE-T partners*

FPMs	HHI	UC3M	UPVLC	FT	GET
AIT	ICCS-NTUA	UoA	UOP	FUB	CORITEL
ISCOM	POLITO	TUE	IT	PUT	ORC
UEssex	USWAN	Ericsson	UPC	KPRC/ACREO	TID

The aim of this work-package (WP) is to organize and harmonize the transmission-related activities within the BONE project. There are 24 partners participating in the VCE on Transmission Techniques – see Table 1. (It should be noted that this Table is not exclusive, and only shows the main contributors to the activities of the WP – other partners have also participated occasionally to VCE-T). Since the theme of Transmission in Optical Systems is rather broad, the interests of the various partners vary significantly. In order to address the varying background and interests of the partners participating in VCE-T, an extensive Advisory Board has been put in place. The Advisory Board is responsible for setting out the integration strategy for the WP and monitoring the progress made towards achieving its goals. The members of the Advisory Board and their affiliations are shown below:

Periklis Petropoulos (WP leader) and Francesca Parmigiani (ORC)

Karin Ennser (SWANSEA)

Pierluigi Poggiolini (POLITO)

Patrice Megret (FPMs)

Giorgio Maria Tosi Beleffi (ISCOM)

Michel Morvan (GET)

Oscar Gonzalez (TID)

Erwan Pincemin (FT)

The main activities of VCE-T have been grouped within four themes, forming four Focus Groups. The Focus Groups act as common forums of discussion within the WP, eventually leading to joint activities between their participants. The definition of the thematic areas of the Focus Groups emerged after an initial survey that collected the inventory of existing expertise among the WP partners (milestone M15.1). Although these themes reflect broad areas of research on transmission, which are shared among several of the VCE participants, they are not exclusive, as will become evident further into this deliverable. Additional joint activities are encouraged and monitored within VCE-T, and are used to dynamically steer the emphasis of the Focus Groups or even to define new Focus Groups within the VCE whenever this is deemed appropriate.

VCE-T participants have met three times during the first year of BONE. The meetings have been useful in defining or amending the general integration strategy of the WP,



communicating joint results and activities, and acting as networking events, which have actually proven extremely fruitful for the initiation of new joint activities.

## *2.1 Outline of the report*

The aim of this deliverable is to report the actions taken towards encouraging and fostering integration of the BONE groups working on transmission-related issues. It also provides a comprehensive presentation of the technical activities carried out during Y1, which highlight the level of integration already achieved. The report is organised as follows.

Section 3 presents the central activities carried out within the WP in order to encourage integration among the VCE-T participants. The outcomes of the initial inventory survey and the WP meetings are listed there. An initial presentation of the current Focus Groups is also given. Finally, some quantifiable measures of integration are outlined.

Sections 4-7 relate to the technical activities of each of the Focus Groups. They include a collection of studies, and the presentation of the joint results achieved among the WP partners in the first year of the project. Section 4 engages with issues associated with 100 Gb/s transmission, Section 5 is on signal regeneration, Section 6 is on signal amplification and Section 7 is on signal monitoring.

A selection of four further joint activities conducted among the WP partners during the reporting period is presented in Section 8. The report closes with some Conclusions in Section 9, and an outlook to Year 2 activities.



### 3. Management Activities

The central activities taking place within VCE-T have been organized so as to encourage familiarization between the various groups of the WP, and create a forum of discussion for certain key research topics within Optical Transmission, which are common to several WP partners. These activities act as a vehicle to facilitate joint actions between the participating groups, and are presented below. Mention is also given in this Section to the results achieved in terms of integration during this first year, as these can be quantified in terms of mobility actions, joint publications, etc.

#### 3.1 WP Technical Meetings

In order to augment integration and to enhance familiarisation with the research interests of the various groups, it has been considered essential that the WP partners have met in frequent intervals, especially in this starting phase of the project. Subsequently, the VCE-T partners have met three times during this year. All meetings have been collocated with events which have been heavily attended by BONE partners, and have succeeded in ensuring the participation of partners from almost all of the groups in the WP. The WP meetings have been seminal in discussing and agreeing the integration strategy of VCE-T, whereas several of the joint activities in the WP have been initiated during these events. Besides, the meetings have also been used as opportunities for technical presentations of general interest to the VCE-T partners, as well as for the communication of the progress and the results achieved in the jointly conducted experiments.

The first VCE-T meeting took place during the BONE kick-off event at Torino, in January 2008. The main objectives of the meeting were:

- Decision on the VCE-T leadership team and advisory board
- Definition of the technical objectives of VCE-T
- Agreement on initial strategy towards integration

All the meeting objectives were met. The management team of VCE-T was arranged, and the interest of the partners with respect to the WP technical thematic topics, as these have been defined within the BONE Technical Annex was confirmed. Certain modifications, clarifications and changes were noted. It was finally decided that this discussion would be used as a starting point in a survey among the VCE-T partners, which would collect the individual partners' interests and compare them (see Section 3.2 below). Completion of this survey led to accomplishment of milestone M15.1.

The second VCE-T meeting took place in Athens in June 2008, collocated with the conference ICTON'08. Participants from 23 VCE-T groups attended the meeting. The meeting succeeded a teleconference between the Advisory Board members, and aimed at both refining the integration strategy of the WP and also holding technical discussions themed around presentations from VCE-T partners. The meeting eventually turned into a useful workshop around several key issues in Optical Transmission. The agenda was organised around four longer technical presentations, whereas a number of partners gave short presentations in lieu of introductions to the activities and interests of their groups. The main technical presentations given during the meeting were:

- "Transmission roadmap: The operator's point of view", by Juan Fernandez Palacios (TID)



- “Politecnico di Torino activities on 100G coherent systems” by A. Carena, V. Curri and P. Poggiolini (POLITO)
- “ISCOM group activities” by Davide Forin (ISCOM)
- “Automatic Frequency control in Optical Coherent Systems” by Josep Prat (UPC) – reporting a joint activity between UPC and HHI.

Shorter presentations were given by CORITEL and FUB, ICCS/NTUA, UoE, FPMs, KTH/ACREO, and PUT. In addition, the findings of the VCE-T survey which had been conducted in the previous months were presented to the consortium. Following initial discussions at the Advisory Board teleconference, the presentation of the survey, and the technical presentations of the various partners, the meeting participants agreed on the formation and the topics of Focus Groups. A typical example that indicates the substantial contribution of the meeting discussions towards the VCE-T general strategy consists in the formation of the Group studying Issues Related to 100 Gb/s Transmission. Even though the general area of 100 Gb/s transmission has been included within the technical areas of interest of VCE-T, it was only after the presentations of the partners and the discussion that followed that the specific topics of interest were defined, and a task force was put in place (for a technical description of the activities of this Focus Group, please refer to Section 4 of this report).

Finally, during this 2<sup>nd</sup> VCE-T meeting it was agreed among the partners that the final outcomes of the work carried out within VCE-T would be compiled in a book, which would collect the views and expertise of the VCE-T participants. A task force for this group has already been put in place (led by Giorgio Maria Tosi Beleffi, ISCOM and Antonio Teixeira, IT).

A third VCE-T meeting took place in Rome in October 2008, collocated with the BONE Annual Plenary Meeting. Once again, the vast majority of the partners were represented in the meeting by delegates. This meeting was an opportunity for the partners to provide an update on the progress of the various mobility actions and joint experiments. There was also an update on the Focus Groups topics and activities, and finally the partners agreed on the contents of the present report. However, the main conclusion coming out of this meeting was that partners with common interests tend to group together ever more frequently, and that joint activities between partners are gaining momentum as we move towards the second year of the project.

### *3.2 VCE-T Survey of available expertise and facilities*

One of the first activities of VCE-T was to realise a survey among all WP partners in order to collect their particular interests in Optical Transmission, and gain some appreciation on their corresponding main field(s) of expertise. The survey also collected a list of facilities available in each of the groups, while a separate part asked for the expectations of each of the partners in terms of mode and area of collaboration which they were seeking. Twenty two partners in total responded to the survey, helping to generate a useful reference document for all partners.

The findings of the survey were circulated electronically to all VCE-T partners, and were presented orally during the 2<sup>nd</sup> VCE-T meeting in Athens. For reference, Table 2 lists the research topics of interest to the various partners of the consortium, as declared by them for the VCE-T survey.



**Table 2: Declared research topics of interest of the VCE-T partners (taken from the VCE-T Survey)**

Research Topic	Partner name	Research Topic	Partner name
<b>A. High-speed transmission</b>		<b>Electronic techniques</b>	TUE, PoliTO
100 Gb/s ETDM (multi-level modulation formats)	FT	Digital and analogue processing	FT, UoP
Ultra-high bit rate (>100Gbits) OTDM signals		Mitigation of transmission impairments	AIT, GET/ENST
Signal Processing (Regeneration, grooming, TSI, switching,...)	ORC, TUE, AIT, IT, USWAN, UPVLC, UoA, UESSEX, ACREO/KTH, FUB-CORITEL	<b>Transmitter-based</b>	
Clock recovery and synchronisation	TUE, UESSEX, ACREO/KTH	Technologies	Ericsson
Ultra dense WDM	FT, PUT, FPMs, ICCS-NTUA	Advanced modulation formats	USWAN, ACREO/KTH, FUB-CORITEL
	PoliTO	<b>Receiver-based</b>	TUE
OFDM		Various Techniques	ORC, Fraunhofer, PoliTO
<b>Coherent detection techniques</b>	TUE, FT, GET/ENST, PUT	<b>In-line</b>	
Amplification/Processing	ORC, UoA	Pulse shaping	ORC, UPVLC
Transmission performance of PSK/D(Q)PSK and QAM	Fraunhofer, PoliTO	Techniques- Amplification and processing of phase-sensitive signals	ORC, UoA
<b>Backward compatibility</b>	GET/ENST, ACREO/KTH	Techniques- Fibre-based regeneration	ORC, ISCOM, UoA
<b>Development of network planning models and techno-economic evaluation</b>	AIT, UESSEX	Techniques- Phase conjugation	UoA
<b>Research Topic</b>	<b>Partner name</b>	<b>Designing and fabricating new devices</b>	
<b>Simulations</b>	ORC, FT, PUT, IT, Fraunhofer, FPMs, PoliTO, ACREO/KTH, FUB-CORITEL	To mitigate the transmission impairments based on FBGs	UPVLC
Modelling metro and long haul transmission systems	AIT, USWAN	<b>Research Topic</b>	<b>Partner name</b>
SOA dynamics for phase and amplitude modulated signals	ISCOM	<b>C. Monitoring</b>	
<b>Reliability of High speed components</b>	Ericsson	<b>Distributed monitoring</b>	
		OPM prototype development	GET/ENST
<b>B. Mitigation of transmission impairments</b>		OTDR based metrology	FPMs
<b>All-Optical techniques</b>		<b>Transmission layer supervision</b>	GET/ENST, IT, FPMs
Fiber based Regeneration in step-index fibres	ORC, IT, ISCOM, FPMs, USWAN, UoA, ICCS-NTUA	<b>Pulse characterisation</b>	IT
Fiber based Regeneration in microstructure fibres	ORC, ISCOM	FROG techniques for precise pulse characterisation	ORC
SOA-based Regeneration	USWAN, UoA, ICCS-NTUA, UESSEX	<b>Performance and Reliability of ROADM, power monitors</b>	Ericsson
PMD/Dispersion compensation/emulation	ORC, GET/ENST, IT, FPMs, UPVLC, UC3M, FUB-CORITEL		
Brillouin Effects in fibres	ORC		
Optical filters	ORC, UC3M		



### 3.3 Focus Groups

The initial survey which had been conducted among the WP participants towards the beginning of the lifetime of VCE-T revealed a few research topics of interest that are shared among several groups. Based on the findings of this survey, the Advisory Board decided to define four Focus Groups that will independently investigate each of these topics. The final definition of the thematic areas of the Focus Groups was agreed among the VCE-T participants during an early WP meeting.

The role of the Focus Groups is to promote discussion and collaboration around topics of joint interest, and to define the core technical areas of the WP without however restricting the partners' activities to these areas alone. In addition, the Focus Groups are viewed as dynamic areas, the orientation of which may be reviewed as required during the lifetime of VCE-T. The definition of the four Focus Group topics and their moderators were agreed during an early WP meeting (2<sup>nd</sup> VCE-T meeting, Athens – see Section 3.1), and are as follows:

- Key issues in 100Gb/s transmission (moderator: Juan Fernando Palacios, TID)
- Signal regeneration in fibres (moderator: Periklis Petropoulos, ORC) and semiconductor optical amplifiers (moderator: Giorgio Maria Tosi Beleffi, ISCOM)
- Amplification in transmission with emphasis on burst amplification (moderator: Antonio Teixeira, IT)
- Signal monitoring (moderator: Michel Morvan, GET)

The technical activities of these Focus Groups in the first year of the project are presented in detail in this report, along with additional joint activities of the VCE-T partners (see Sections 4 through to 8).

### 3.4 Quantifiable measures of integration

The first year of VCE-T has already seen a number of joint activities being initiated, whereas the first joint publications stemming from the activities of the WP have appeared. In total, there have been five short- or longer-term mobility actions between partners, and seven joint experiments. These experiments also include those which have not required the mobilisation of human resources, but have been the result of a joint effort between two or more VCE-T partners. Seven joint papers resulting from the various joint activities have already been accepted for publication in journals or conference proceedings.

In addition, VCE-T has jointly organised with WP2 the Summer School on “Electronics and Signal Processing for Optics”, which took place at FPMs in October 2008. The members of VCE-T assisted in the organisation of the School by participating in its Organising and Technical Committees, giving lectures and also by participating with students who attended the School programme.

It is worth noting that at the end of the first year of the project, there is evidence of a gathering momentum in the integration activities of the VCE-T partners. As an indication of this evidence, it is noted that there have been a further three mobility actions in preparation, whereas there have been discussions of joint proposals being organised among partners.



## 4. Key Issues in 100 Gb/s Transmission (TID, ACREO, POLITO, AIT)

### 4.1 Introduction

The continuous and significant growth in IP traffic due to converged IP networks, forthcoming high-bandwidth services and new Internet users is expected to drive current network capacity to its limit. Therefore, carriers are seeking to improve their networks with higher bandwidth optical links. In this study we analyse the feasibility to deploy an all-optical meshed backbone at 100 Gbps.

Specifically, we investigate a suitable modulation scheme to accomplish:

- Moderate optical and electrical complexity.
- Appropriate commitment between OSNR and spectral efficiency.
- Suitability for the operator's fibre plant.

The last point is crucial for a non-disruptive evolution to 100G. The design of the links is determined by:

- Link distance: this is a deterministic parameter conditioned to physical impairments. However, it is very important to obtain a maximum link reach value regarding the operating conditions in order to implement efficient all-optical restoration techniques.
- Number of crossed nodes. Every ROADM consists of a number of filters. The effect of these filters on data signal degrades the transmission quality and, therefore, reduces the maximum distance. The quantification of this degradation is one of the aims of this study.
- Physical impairments. Attenuation and chromatic dispersion are well-known impairments. Optical amplifiers are a good solution for attenuation and chromatic dispersion is managed today by both optical and electrical modules. The critical point in 100G transmission is PMD. This sort of dispersion is non-deterministic and difficult to manage. Furthermore, the tolerance to PMD in 100G optical transmission is one tenth of 10G transmission. The influence of PMD on optical reach is also analyzed in our study.

### 4.2 Short Reach Transmission

#### 4.2.1 Introduction

Increasing capacity is a constant demand in modern optical communications. Research efforts on highly spectral efficient modulation formats, such as DQPSK [1], use of polarization multiplexing [2], SSB formats [3] etc. address this problem. Despite the advantage in transmission rate of such formats, most of the existing network architecture is designed for IM/DD systems. Moreover, the inflicted cost in upgrading of equipment provides a limiting factor to the end-customer services. A technology therefore is required to bridge the transmission rate gap between OOK and advanced modulation formats in order to enhance the development of end-customer services, while at the same time guarantee compatibility with the existing optical network.

In the past, incoherent 4-level ASK was considered as a way to increase the spectral efficiency [4]. However, in order to achieve spectral efficiency a higher order optical filtering is required [5]. This is due to the inherent back-to-back OSNR degradation of 4-ary ASK as compared to OOK due to the introduced power levels. The power leveling should be carefully adjusted according to the dominant noise factors affecting the system [6, 7]. Walklin and Conradi [8] examined 4-ary ASK performance against 10 Gbs OOK in terms of dispersion and relative intensity noise (RIN) tolerance. According to [8] the transmission distance of dispersion limited systems can be extended through the use of multilevel signalling. A comparative study [9] has also shown that the nonlinear Kerr effect affects less 4-ary ASK than OOK. Nevertheless, the enhanced tolerance to dispersion, nonlinear effects and the spectral advantages of multilevel signals are not sufficient to counterpart the initial back-to-back OSNR penalty in end-to-end long-haul communications. However, the use of 4-ary ASK was also proposed as a way of contacting amplitude multiplexing [10]. A fibre based technique based on FWM achieving this amplitude multiplexing is proposed in [11]. Recently, Kikuchi et al. [12] demonstrated a technique that minimizes intersymbol interference in multilevel signalling and through this the implementation of various 32 level systems was achieved [13]. This same technique was demonstrated to implement a multilevel ASK modulator.

In this work, we examine the potential utilization of 4-ary ASK in short high capacity optical transmissions as means to upgrade the transmission rate by taking advantage of its spectral characteristics. This study examines effectively the possibility use of 4-ary ASK in future 100 Gbps Ethernet technology. Moreover, the study also shows that multilevel signaling may be appealing under scenarios where cost effective, high-capacity, short-distance techniques are required.

#### 4.2.2 Transmitter and Receiver Issues

The simplest approach to construct a 4-level ASK optical signal a power addition of two optical fields [5]. Kikuchi et al. [12] have also suggested a reduced inter-symbol interference (ISI) method by using two BPSK modulators in order to synthesize coherently a 4-ary ASK. In all cases, the level spacing should be carefully set so as to minimize the effect of physical impairments [6, 7]. In this paragraph, we extend the design strategies by proposing a minimal all optical 4-level ASK transmitter design. The design is based on a basic MZI modulator which is appropriately imbalanced to result in a quadratic level spacing.

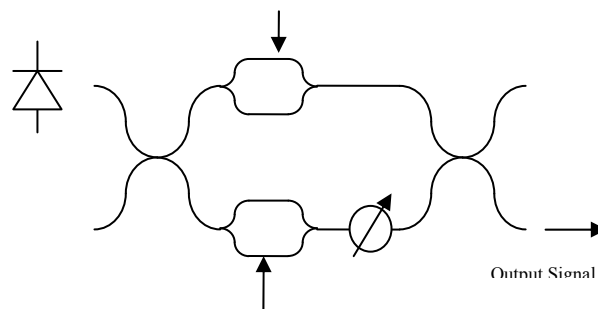


Figure 1: Proposed Transmitter design

Briefly, we consider an imbalanced MZI (Figure 1) utilizing nested MZIs operating as intensity modulators at each arm and a 3-dB attenuator is introduced at the lower arm. The

MZI imbalance is driven by the coupling coefficient  $c$  at the input of the MZI. The amplitude of the optical field at the output of the MZI is then:

$$E(t) = \frac{cA(t)}{2} - \frac{\sqrt{2}}{4} \sqrt{1-c^2} B(t) \quad (1)$$

where  $A(t)$  and  $B(t)$  correspond to the modulation of the two electrical sequences, multiplexed to give the 4-level ASK signal, on the CW. Using (1) the four possible power levels which result are plotted in Figure 2 as a function of the coupling coefficient. The dashed lines correspond to the required quadratic level spacing as defined by the highest power level. Evidently, there are 2 regions of operation, at  $c = 0.33$  and  $0.81$ , corresponding to an alternative mapping of input sequence bits to symbols. Note also that another set of solutions exists for the through port of the transmitter, however the power efficiency is greater for the cross port.

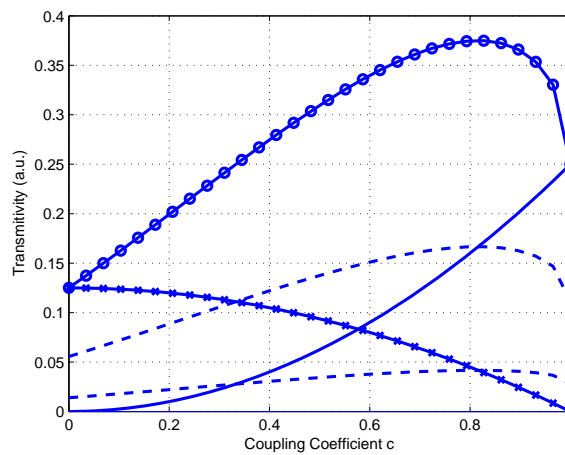


Figure 2: Power levels vs coupling coefficient. Circles: Power Level 3, Crosses: Power Level 2, Solid line: Power Level 1, Dashed lines: required quadratic levels relative to Power Level 3.

At the receiver, an electronic logic circuit implementing a priority encoder is required for the decoding. In the past, Walkling and Conradi [5] have utilized a priority encoder operating at 5 Gbaud. It should be noted that the current technology supports 50 GHz D type flip flops and comparators and therefore the technology for 100 Gbps Ethernet using multilevel ASK is already accessible and cost effective.

### 4.2.3 Results

#### 4.2.3.1 4-ary ASK

In order to examine the reach of 4-ary ASK transmissions we simulated a basic link as shown in Figure 3. The optical and electrical filters assumed were 3<sup>rd</sup> order Gaussian and 3<sup>rd</sup> order Bessel filters, respectively, and no optical amplification was assumed. The optimum cut-off frequencies for optical and electrical filtering were found to be 120 GHz and 50 GHz, respectively, as shown in Figure 4. In Figure 5 the BER as a function of the OSNR is plotted for 100, 160 and 200 Gbps in the back to back case. Note that for the OSNR measurements the noise power is measured within 0.1 nm. According to the figure, high OSNR levels are required for error free transmission at BER = 10<sup>-9</sup>. However, for an OSNR equal to 43.8 dB a transmission rate of 200 Gbps could be attained for short transmissions.

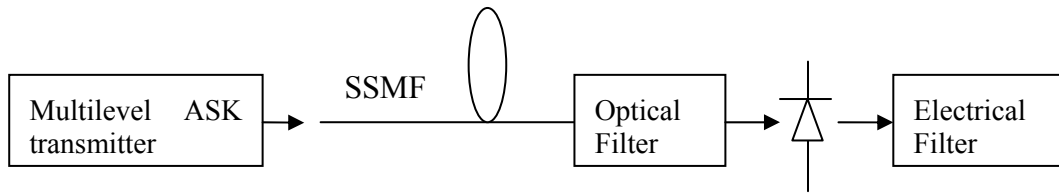


Figure 3: Basic link model

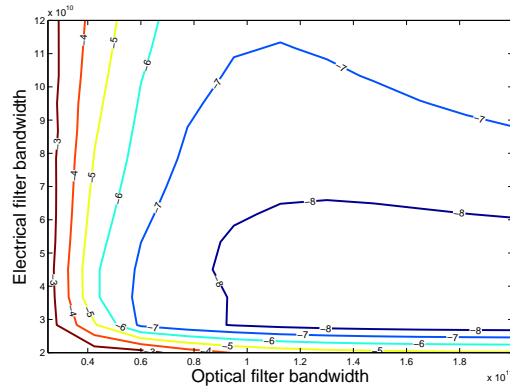


Figure 4: BER vs Electrical and Optical filter 3-dB cut-off frequencies for 100 Gbps 4-ary ASK.

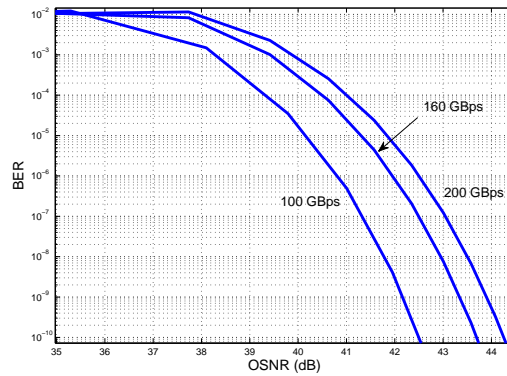


Figure 5: BER vs OSNR for 100, 160 and 200 Gbps 4-ary ASK.

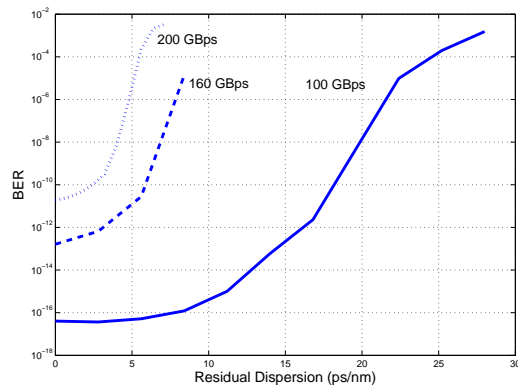


Figure 6: BER vs Residual Dispersion for 100, 160 and 200 Gbps 4-ary ASK (OSNR = 45 dB).



Next, we examine the effect of dispersion on high speed 4-ary ASK. In Figure 6, the dispersion tolerance of 4-ary ASK is examined. According to the figure, error free transmission at BER =  $10^{-9}$  and for an OSNR of 45 dB can be achieved without dispersion compensation at distances of 180m, 350m and 1050m of SMF for 200, 160 and 100 GBps, respectively. Longer reach can be attained either by using FEC or alternative fiber types (i.e. NZDSF).

#### A4.2.3.2 Higher Level ASK

In this paragraph we examine the benefit that can be obtained by utilizing more power signaling levels. Using the methodology described in [8] we simulated an 8-level ASK system. In Figure 7, the effect of the temporal pulse width in a 128.1 Gbps 8-ary ASK system is shown for the back-to-back case. The optimum pulse width is in the range 0.75 to 0.80 times the symbol period, however the exact value depends on the optical and electrical filter bandwidths.

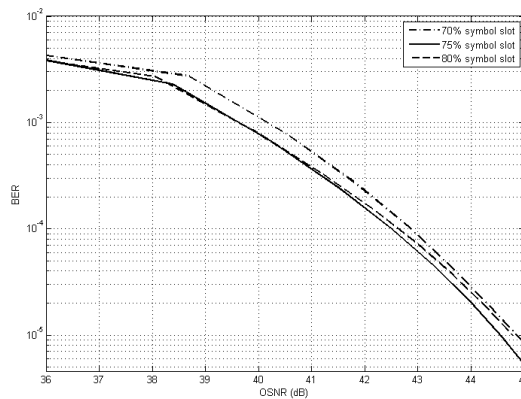


Figure 7: BER vs OSNR for a 128.1 GBps 8-ary ASK utilizing pulses of different temporal widths.

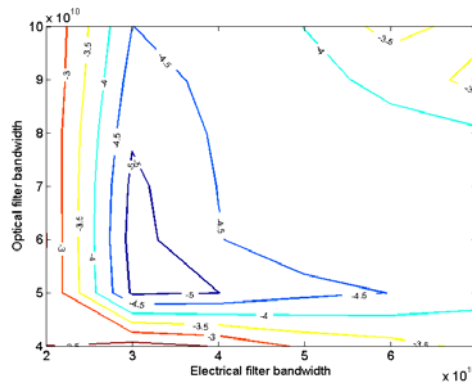


Figure 8:  $\log_{10}(\text{BER})$  vs Optical and Electrical filters' 3dB bandwidth for 128.1 GBps 8-ary ASK (OSNR = 45 dB, Pulse Width= 75% Symbol Slot).

In Figure 8, the optimum optical and electrical 3 dB cut-off frequencies for the case of a 128.1 Gbps (3x42.7 Gbps) 8 level ASK system with pulses of temporal width 75% to the symbol period are identified. These are 50 GHz and 30 GHz for optical and electrical filters respectively, corresponding to 1.17 and 0.70 times the baud rate. Comparing these figures to the 4-ary ASK case, we conclude that the optimal electrical filter bandwidth is slightly higher for the 8-ary ASK case. Moreover, the sensitivity in both optical and electrical filter bandwidths is greater in the 8-ary case than the 4-ary case. Therefore the transmitter and the filters are required to have greater stability in terms of frequency drift. Another conclusion



from the graphs is that the BER values obtained show that the use of FEC is required to achieve error free transmissions at  $10^{-9}$ .

Next we consider the case where multiple channels are transmitted inside SMF without dispersion compensation. We simulated a 9 channel system with 150 GHz channel spacing. In Figure 9 the BER of the centre channel as a function of SMF length is shown. The optimum optical and electrical filter 3-dB bandwidths were found to be stable through the 600m to 850m range and their values were 100 GHz and 30 GHz, respectively. Commenting on the graph we conclude that the performance is almost linearly decreasing in the range 600m to 850m. Moreover, the absolute values of BER are low enough to allow the use of FEC.

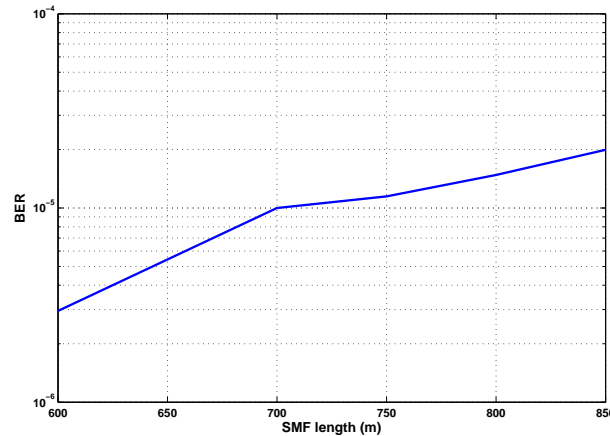


Figure 9: BER vs SMF length for 128.1 Gbps 8-ary ASK 9 channel system (OSNR = 45 dB, Pulse Width= 75% Symbol Slot).

#### 4.2.4 Conclusions

In this study we examined the feasibility of using 4-ary and 8-ary ASK as a candidate for 100 Gbps short optical links. According to the analysis multilevel ASK requires high OSNR values in order to achieve error free transmissions. We focused on the filtering effects and we managed to identify the optimum 3 dB bandwidth values for both electrical and optical filters under various scenarios. We studied the influence of pulse width on BER performance and found that an optimum is obtained at around 75% the symbol rate. We also examined the reach of a 9 channel optical network utilizing 8-level ASK with a 0.66 spectral efficiency without using polarization multiplexing. Our findings show that BER performance decreases linearly in the range 600m to 850m SMF but the absolute BER values found are sufficient in order for the systems to be used in conjunction with FEC.

From the above we conclude that 8-ary ASK is an attractive solution for 100 Gbps Ethernet where short links are required. The main advantage of this format is that it requires no extra costly optical components. Moreover, the reach can be extended by the use of electrical equalization, forward error correction and finally the use of NZDSF fiber.



## 4.3 Long Reach Transmission

### 4.3.1 Objectives

#### 4.3.1.1 Main goal

The main objective of the working group on 100Gbps simulation is to determine the maximum reach for a 100 GbE link with a 111Gbps bitrate

Therefore, we are interested in the joint effect of these elements:

- **Transmitter characteristics:** modulation formats DQPSK and PM-QPSK.
- **Fibre characteristics:** chromatic dispersion, polarization mode dispersion, attenuation and non-linear effects.
- **Nodes characteristics:** cascaded ROADM.
- **Receiver characteristics:** sensibility and FEC techniques.

#### 4.3.1.2 Other studies

After the study and description of a single link, our purpose is to investigate the interaction among different channels in the same fibre. Especially, we focus on:

- Inter-channel non linear effects.
- Effect of multirate and multiple modulations in different channels. We are mainly interested in the coexistence of 100G and 40G lambdas in the same fibre.

### 4.3.2 Simulation Plan

Our simulation plan is based on different simulation platforms (e.g VPI photonics). The common parameters for every simulation are the following:

- **Fibres:**

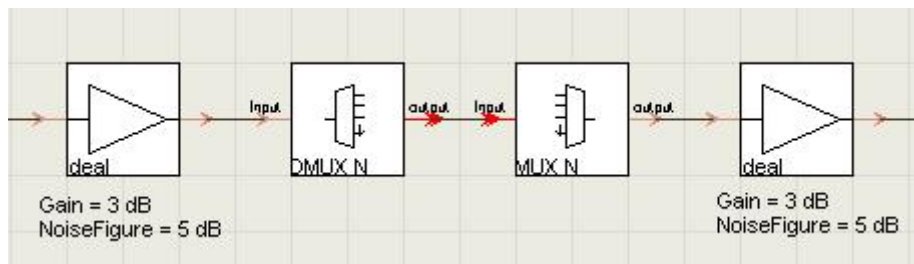
	SMF	DFC
Attenuation [dB/km]	0,35	0,5
Chromatic dispersion [ps/nm·km]	20	-100
PMD [ps/(km) <sup>1/2</sup> ]	Variable	

Chromatic dispersion is compensated by means of DFC.

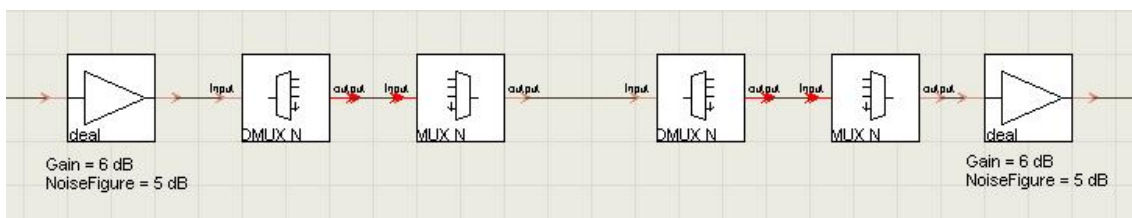
- **Amplification:** We assume the use of EDFA when necessary. The parameters to characterize optical amplification are:
  - Noise Figure: 5dB.
  - Gain: the necessary to compensate losses:



- Booster: 16dB
- In-line amplification: 2x18dB (amplification span: 80km.)
- Pre-amplifier: 10dB.
  - Saturation Power: 18dBm.
- **ROADM. MUX/DEMUX characteristics:**
  - Filter type: pass band
  - Transfer function: Gaussian.
  - Filter order: 3
  - Insertion loss: 3dB
  - Bandwidth:  $0.75 \cdot \text{BitRate}$ .
  - Channel spacing:
    - 40Gbps: 50GHz.
    - 100Gbps: 100GHz.
  - 2 configurations:
    - 1 MUX and 1 DEMUX (1 WSS):



- 2 MUX and 2 DEMUX (2 WSS):



The scheduled activities are outlined below.

#### A4.3.2.1 Maximum optical reach for DQPSK and POLMUX-QPSK.

The first stage in the study is to obtain the maximum all-optical reach for a point-to-point link (No ROADMs in the link). This reach will be determined by optical impairments and the characteristics of the transmitter.

N lambdas are considered in the optical link. Therefore, the study is aimed to evaluate how many 100G channels can be delivered in one fibre according to the maximum allowable power. Optical conditions are:

- Transmitter power: variable from -11dBm to 0dBm. (Joint to a commercial booster).
- Maximum optical BER at the receiver:  $10^{-4}$ .



The study will include the following tasks:

Task	BitRate [Gbps]	Modulation	PMD ps/(km) <sup>1/2</sup>
3.1.a	40	DQPSK	0.1, 0.3, 0.5, 0.7, 1
3.1.b	100	DQPSK	0.1, 0.3, 0.5, 0.7, 1
3.1.c	40	POLMUX-QPSK	0.1, 0.3, 0.5, 0.7, 1
3.1.d	100	POLMUX-QPSK	0.1, 0.3, 0.5, 0.7, 1

*A4.3.2.2 Maximum number of ROADM when separated 80km.*

This activity aims to obtain the maximum number of ROADM in an optical link when they are as close as an amplification span (80 km). This will be the worst case in an optical mesh. The purpose of the study is to evaluate the effect of the filters on optical transmission.

Optical conditions are:

- Transmitter power: variable from -11dBm to 0dBm. (Joint to a commercial booster).
- Maximum optical BER at the receiver: 10<sup>-4</sup>.

The study will include the following tasks:

Task	Number of MUX/DEMUX per ROADM	BitRate [Gbps]	Modulation	PMD ps/(km) <sup>1/2</sup>
3.2.a	1	40	DQPSK	0.1, 0.3, 0.5, 0.7, 1
3.2.b	2	40	DQPSK	0.1, 0.3, 0.5, 0.7, 1
3.2.c	1	100	DQPSK	0.1, 0.3, 0.5, 0.7, 1
3.2.d	2	100	DQPSK	0.1, 0.3, 0.5, 0.7, 1
3.2.e	1	40	POLMUX-QPSK	0.1, 0.3, 0.5, 0.7, 1
3.2.f	2	40	POLMUX-QPSK	0.1, 0.3, 0.5, 0.7, 1
3.2.g	1	100	POLMUX-QPSK	0.1, 0.3, 0.5, 0.7, 1
3.2.h	2	100	POLMUX-QPSK	0.1, 0.3, 0.5, 0.7, 1

*A4.3.2.3 Influence of the ROADM placement in the link.*

Taking into account the maximum reach for an optical link without ROADMs, the next step is to evaluate the distance reduction because of the introduction of ROADM in the link.

Given that PMD is not compensated in-line, it will be necessary to determine if ROADM placement in the link is important enough for the achieved optical reach.

The objectives for this activity are the following:



- To determine if ROADMs placement in the link is important in optical reach.
- To determine the optical signal quality at the receiver when going through N ROADMs (with different distances between ROADMs), being N lower than the maximum number of ROADMs obtained in section 3.2.

Optical conditions are:

- Transmitter power: variable from -11dBm to 0dBm. (Joint to a commercial booster).
- Maximum optical BER at the receiver:  $10^{-4}$ .

The study will include the following tasks:

Task	Number of MUX/DEMUX per ROADM	BitRate [Gbps]	Modulation	PMD ps/(km) <sup>1/2</sup>
3.3.a	1	40	DQPSK	0.1, 0.3, 0.5, 0.7, 1
3.3.b	2	40	DQPSK	0.1, 0.3, 0.5, 0.7, 1
3.3.c	1	100	DQPSK	0.1, 0.3, 0.5, 0.7, 1
3.3.d	2	100	DQPSK	0.1, 0.3, 0.5, 0.7, 1
3.3.e	1	40	POLMUX-QPSK	0.1, 0.3, 0.5, 0.7, 1
3.3.f	2	40	POLMUX-QPSK	0.1, 0.3, 0.5, 0.7, 1
3.3.g	1	100	POLMUX-QPSK	0.1, 0.3, 0.5, 0.7, 1
3.3.h	2	100	POLMUX-QPSK	0.1, 0.3, 0.5, 0.7, 1

*A4.3.2.4 Multi-rate coexistence in the same fibre.*

The Optical coexistence of different modulation formats and different bitrates supposes degradation in optical transmission quality due to interchannel impairments.

This activity aims to perform a quantitative and qualitative analysis of such degradation for different modulation formats:

Optical conditions are:

- Transmitter power: variable from -11dBm to 0dBm. (Joint to a commercial booster).
- Maximum optical BER at the receiver:  $10^{-4}$ .

The study will include the following tasks:

Task	Intermediate ROADM?	Number of channels (BitRate)			PMD ps/(km) <sup>1/2</sup>
		NRZ	DQPSK	PM-QPSK	
3.4.a	NO	X (10G)	Y (40G)	-	0.1, 0.5, 1
3.4.b	NO	X (10G)	-	Z (40G)	0.1, 0.5, 1



3.4.c	NO	X (40G)	Y (100G)		0.1, 0.5, 1
3.4.d	NO	X (40G)	-	Z (100G)	0.1, 0.5, 1
3.4.e	YES	X (10G)	Y (40G)	-	0.1, 0.5, 1
3.4.f	YES	X (10G)	-	Z (40G)	0.1, 0.5, 1
3.4.g	YES	X (40G)	Y (100G)		0.1, 0.5, 1
3.4.h	YES	X (40G)	-	Z (100G)	0.1, 0.5, 1
3.4.i	NO	X (10G)	Y (40G)	Z (40G)	0.1, 0.5, 1
3.4.j	NO	X (40G)	Y (100G)	Z (100G)	0.1, 0.5, 1
3.4.k	YES	X (10G)	Y (40G)	Z (40G)	0.1, 0.5, 1
3.4.l	YES	X (40G)	Y (100G)	Z (100G)	0.1, 0.5, 1

Where X, Y and Z are an appropriate number of channels to observe the interchannel effect. For these simulations we could simulate links of the Spanish photonic mesh (end to end distance, ROADM location, etc)

**4.3.3 PRELIMINARY RESULTS**

*A4.3.3.1 Maximum Reach for DQPSK at 100G*

Next figures show the main results of the simulations carried out by ACREO, TID and POLITO.

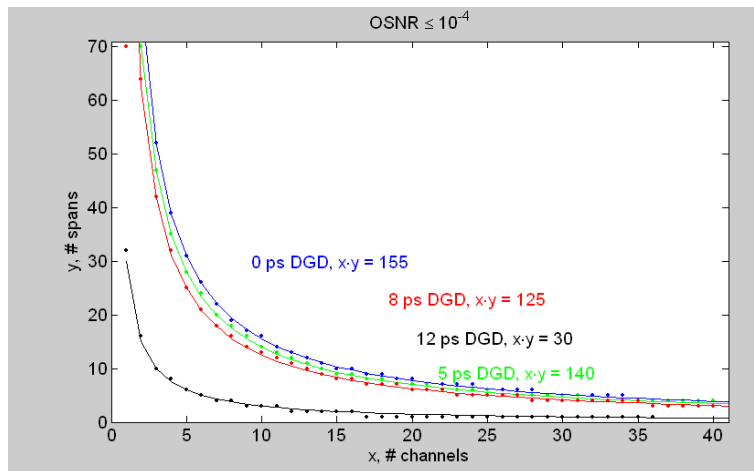


Figure 10: Maximum number of spans for different PMD values (source: Acreo)

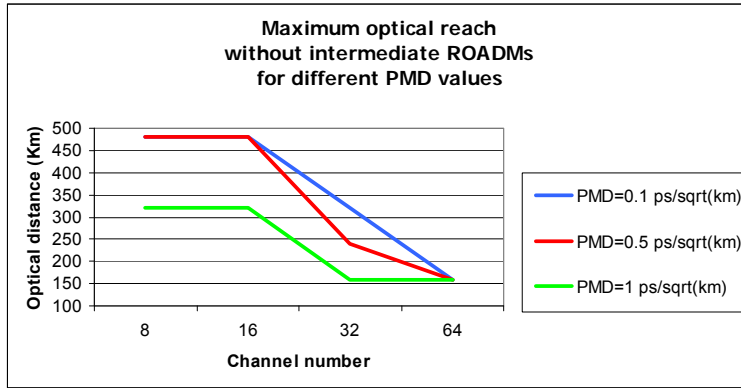


Figure 11: Maximum reach without intermediate ROADMs for different PMD values (high order PMD, one outcome) (source: TID)

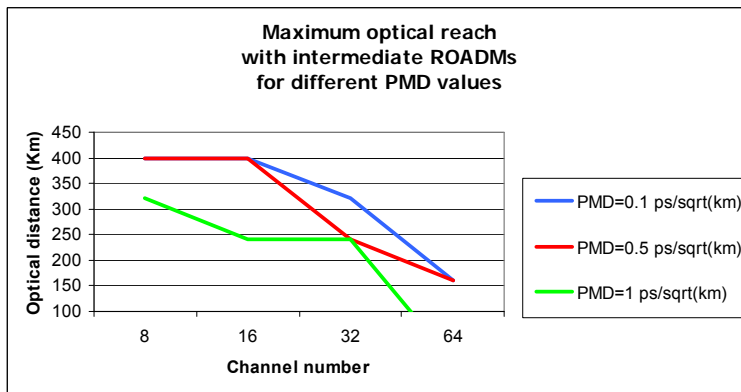


Figure 12: Maximum reach with intermediate ROADMs for different PMD values (high order PMD, one outcome) (source: TID)

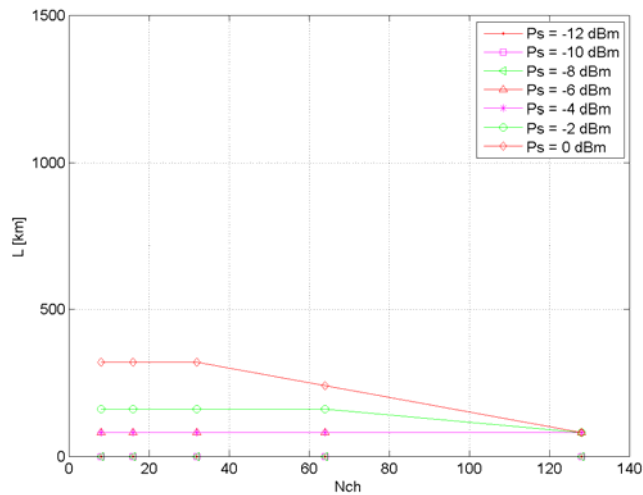


Figure 13: Maximum reach without ROADMs in absence of PMD as a function of number of channels and for different launch power per channel. Considering a maximum booster power of +17 dBm (source: POLITO).

Taking a look on the above figures we can check that the maximum reach without regeneration strongly depends on both PMD and the number of channels per fibre.

The following figures show some of the simulation schemes used by ACREO, TID and POLITO.

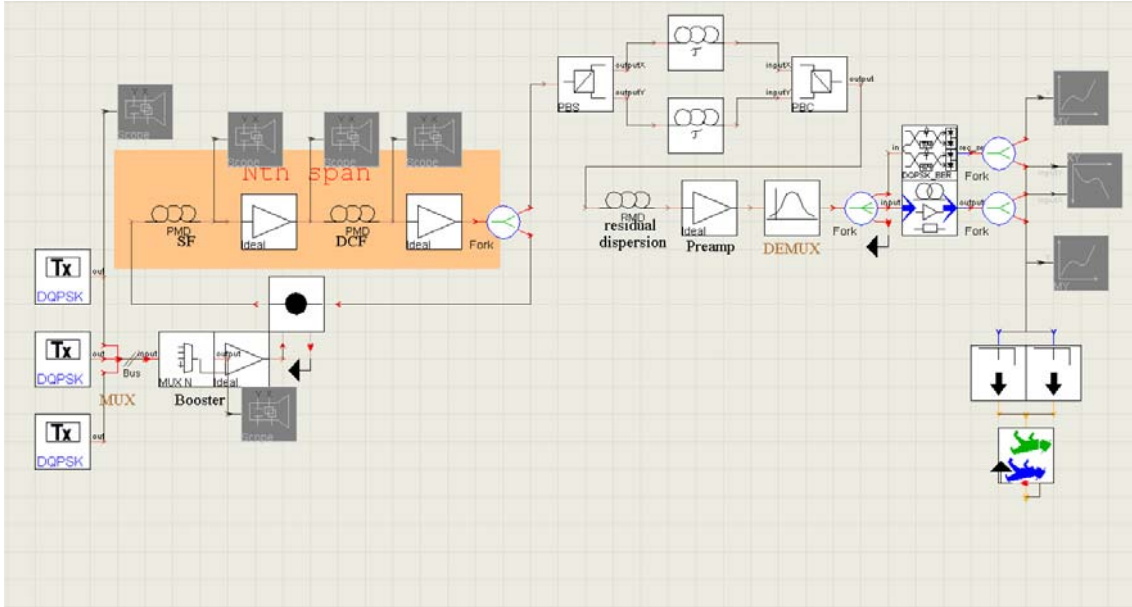


Figure 14: DQPSK Simulation Scheme in VPI Transmission Maker (source: ACREO)

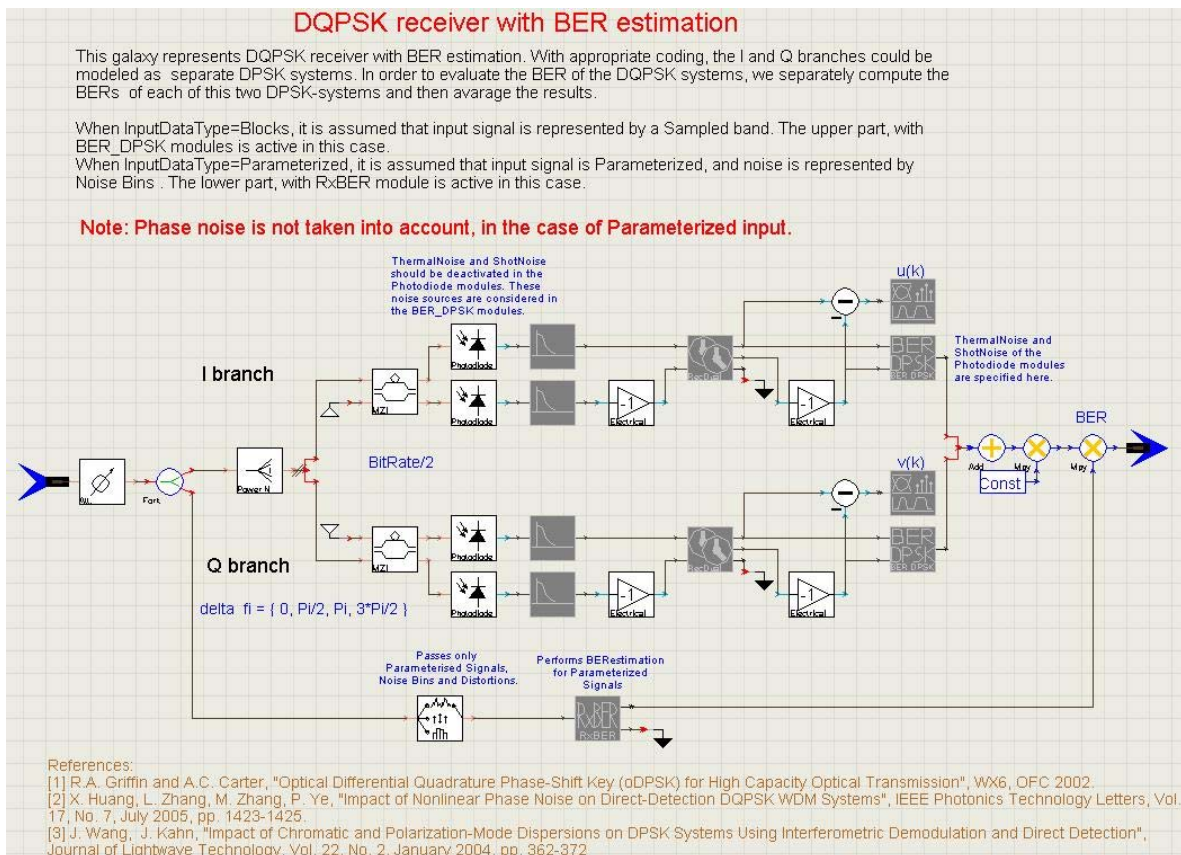


Figure 15: DQPSK Receiver Scheme in VPI Transmission Maker (source: TID)

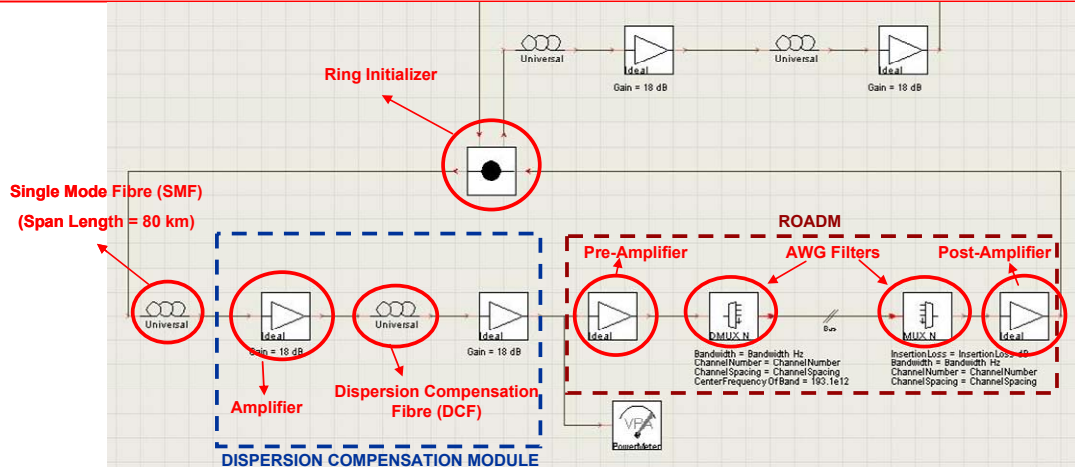


Figure 16: Optical links with intermediate ROADMs in VPI Transmission Maker (source: TID)

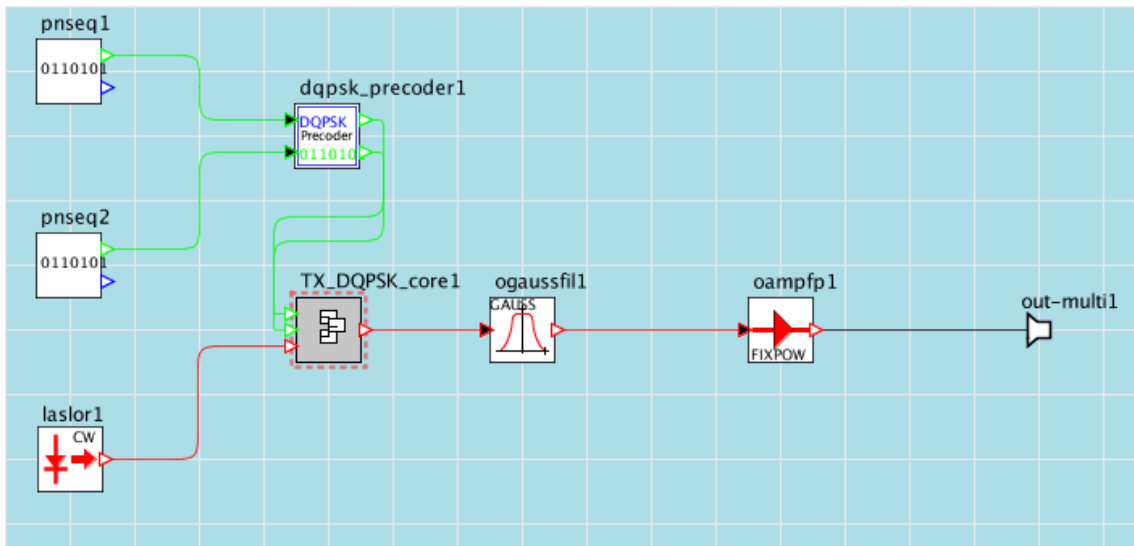


Figure 17: DQPSK Transmitter Scheme in OptSim (source: POLITO).

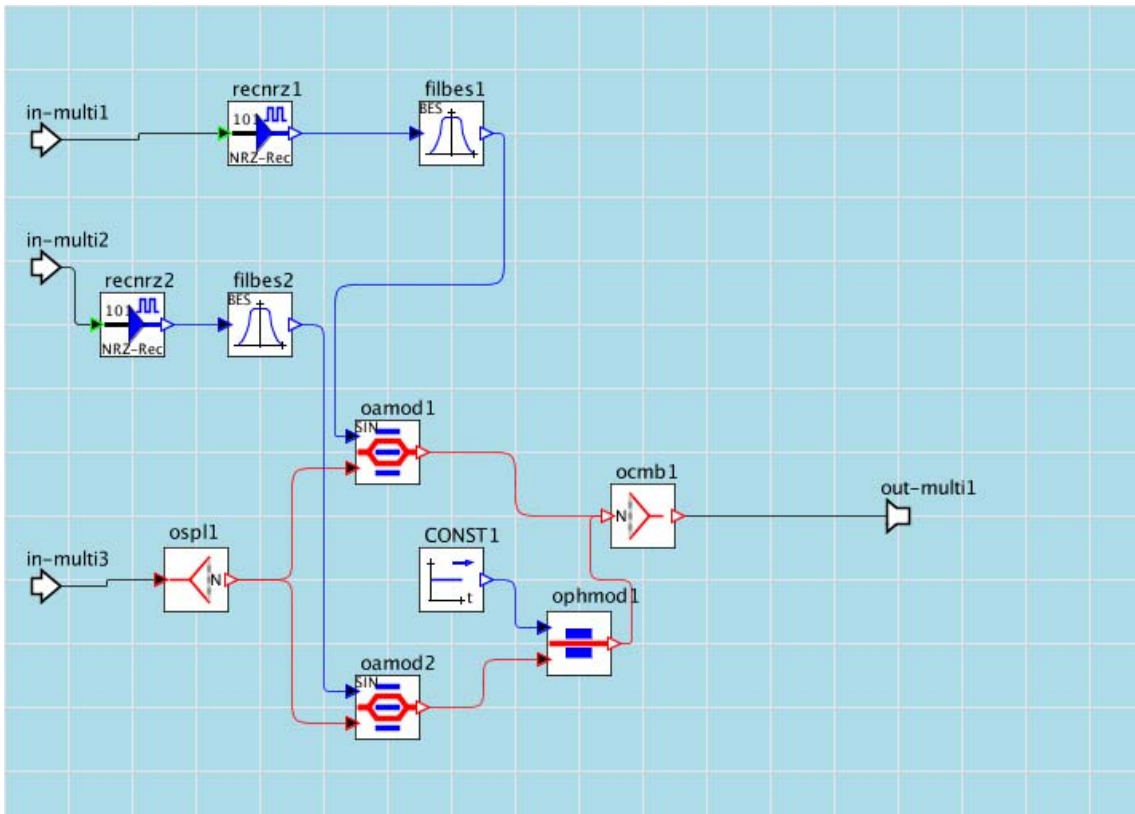


Figure 18: DQPSK Modulator Scheme in OptSim (source: POLITO).

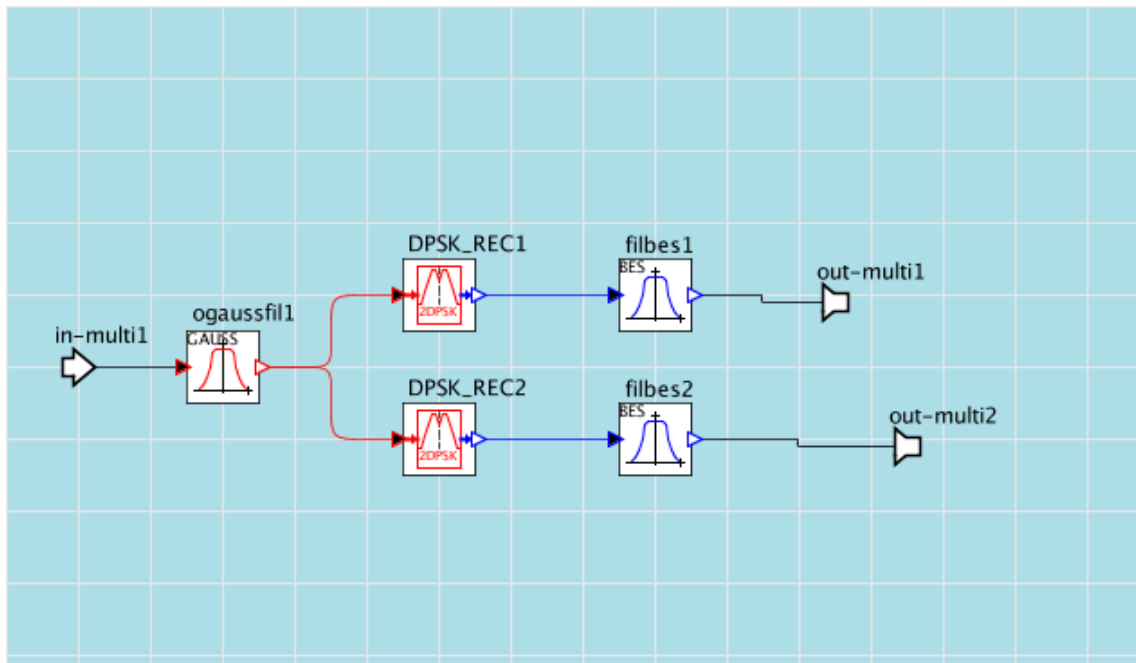


Figure 19: DQPSK Receiver Scheme in OptSim (source: POLITO).

### A4.3.3.2 Maximum Reach for PM-QPSK at 100G

POLITO also studied PM-QPSK with coherent receiver for polarization, frequency and phase recovery applied through electronic DSP processing of the received signal. In the next figure is shown the maximum reach for this modulation format.

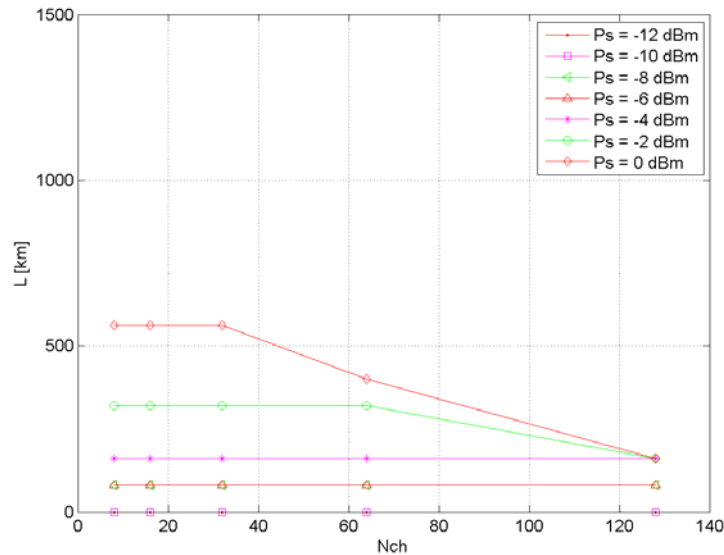


Figure 20: Maximum reach without ROADM in absence of PMD as a function of number of channels and for different launch power per channel. Considering a maximum booster power of +17 dBm (source: POLITO).

In the following we report some of the simulation schemes used by POLITO for PM-QPSK.

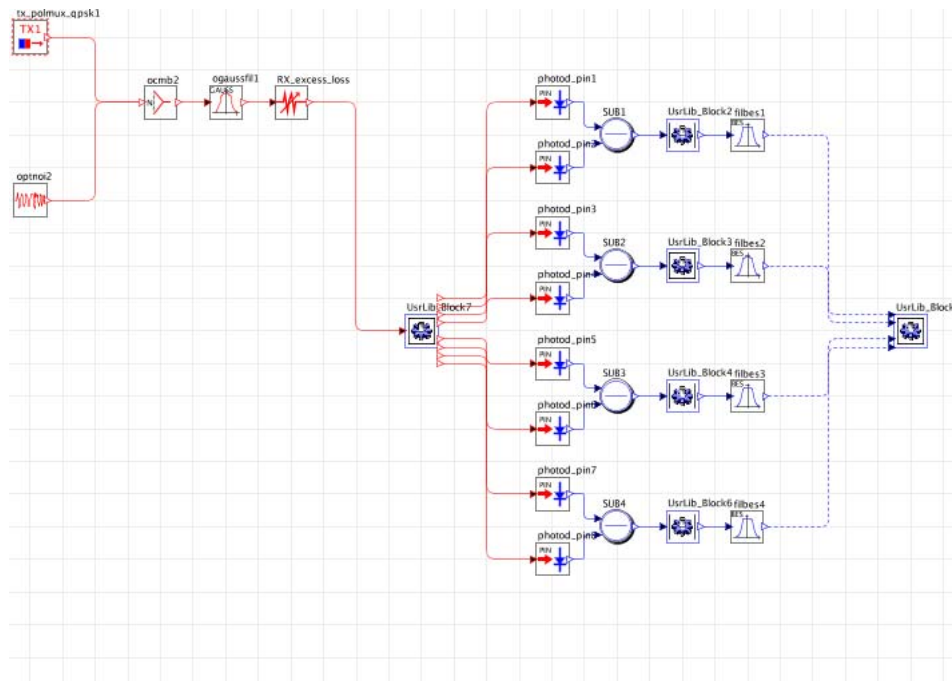


Figure 21: PM-QPSK Simulation Scheme in OptSim (source: POLITO). The UsrLib block in the middle of the layout is a custom block for simulating the 90-degree optical hybrid and the local oscillator. Then, it is followed by four balanced photodiodes. The UsrLib block on the right is for simulating the DSP processing of the four electrical signals coming out of the system.

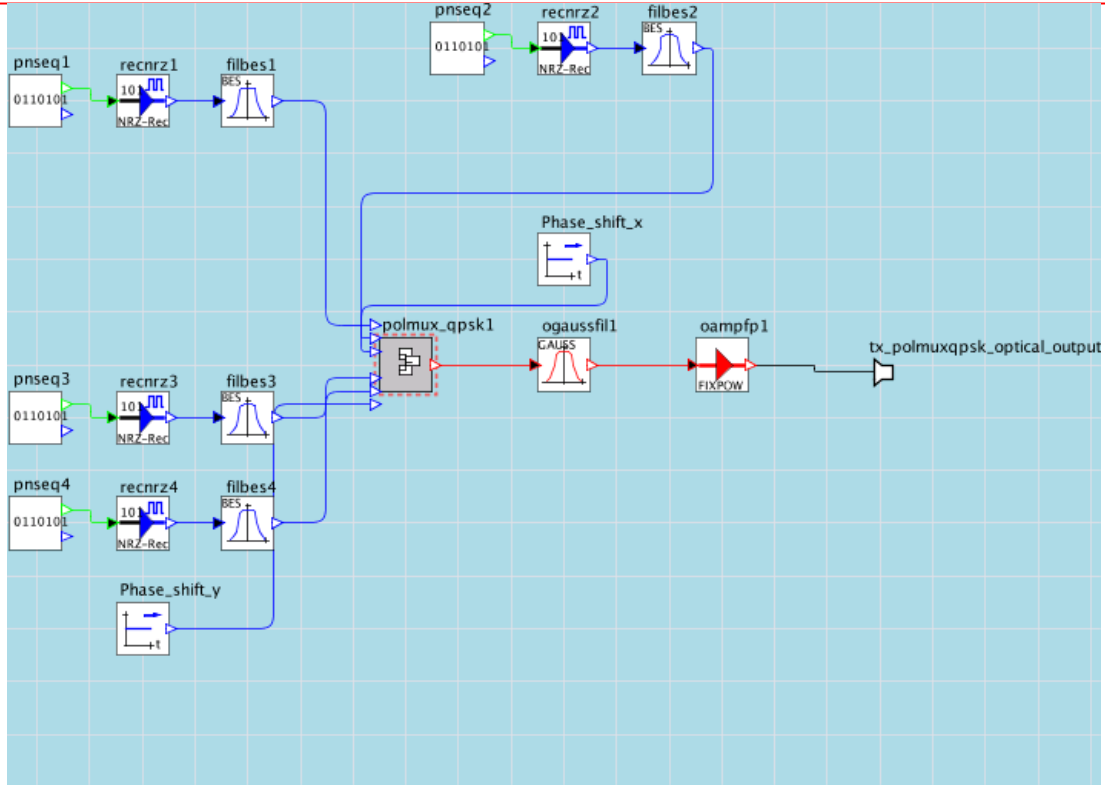


Figure 22: PM-QPSK transmitter Simulation Scheme in OptSim: the four data stream reaching the PM-QPSK modulator. (source: POLITO).

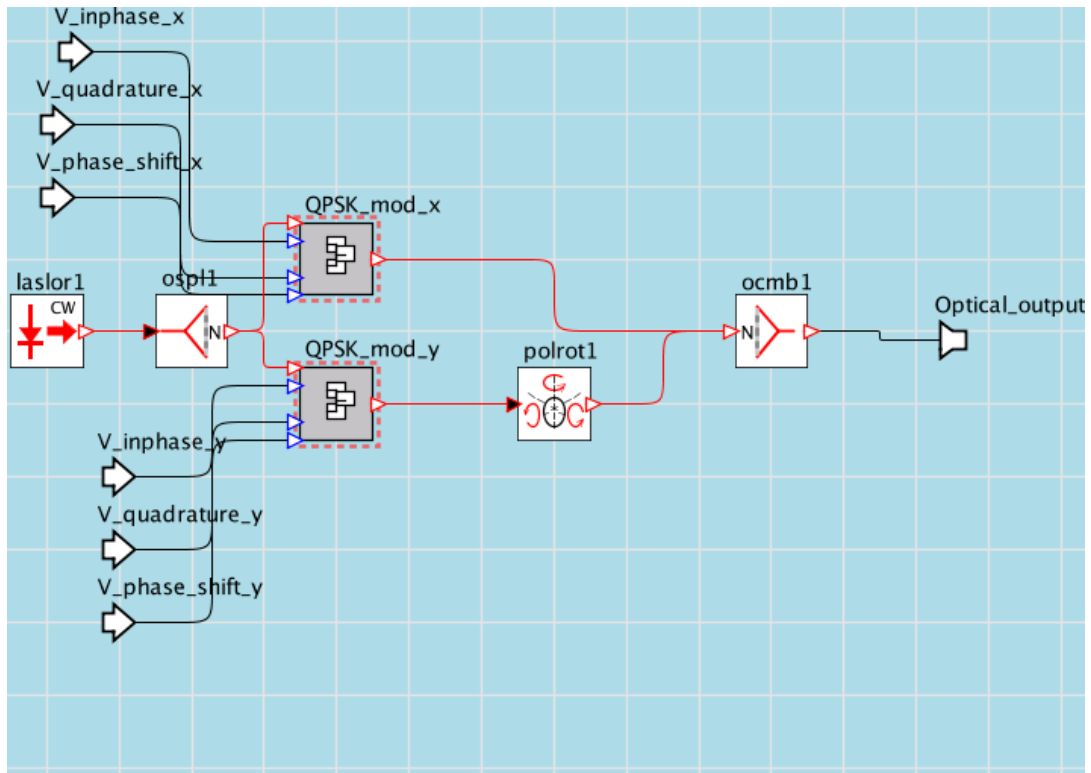


Figure 23: PM-QPSK modulator with the laser source in OptSim (source: POLITO).

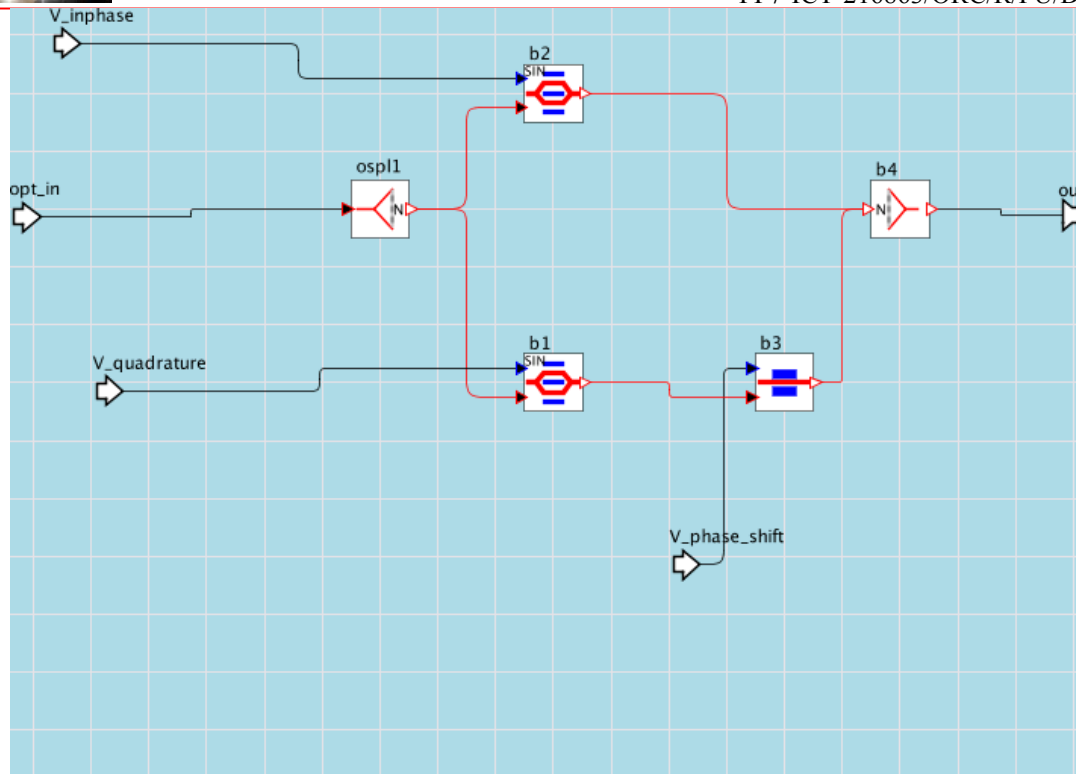


Figure 24: QPSK modulator in OptSim (source: POLITO).

#### 4.4 References

- [1] C. Wree et al., "High Spectral Efficiency 1.6-b/s/Hz Transmission (8 x 40 Gb/s With a 25-GHz Grid) Over 200-km SSMF Using RZ-DQPSK and Polarization Multiplexing," *IEEE Photon. Technol. Lett.*, vol. 15, no. 9, pp. 1303–1305, Sep. 2003.
- [2] A. H. Gnauck et al., "25.6-Tb/s WDM Transmission of Polarization-Multiplexed RZ-DQPSK Signals," *J. Lightw. Technol.*, vol. 26, no. 1, pp. 79–84, Jan. 2008.
- [3] Pedro M. A. Charrua and Adolfo V. T. Cartaxo, "Optimized Filtering for AMI-RZ and DCS-RZ SSB Signals in 40-Gb/s/ch-Based UDWDM Systems," *IEEE Photon. Technol. Lett.*, vol. 17, no.1, pp. 223–225, Jan. 2005.
- [4] L. J. Cimini and G J Foschini, "Can multilevel Signaling Improve the Spectral Efficiency of ASK Optical FDM Systems?," *IEEE Transactions on Communications*, vo. 41,no.7, pp. 1084 – 1090, July1993.
- [5] N. S. Avlonitis, "Multilevel signaling for increasing the spectral efficiency of modern optical communications systems", MSc Thesis, Imperial College London, Sep. 2000.
- [6] J. Rebola and A. V. T. Cartaxo, "On the Quaternary level spacing signalling optimisation for increasing the transmission distance in optical communication systems," 3rd Conferencia Nacional de Telecomunicacoes," pp. 514 – 518, 23 – 24 April 2001.
- [7] N. S. Avlonitis and E. M. Yeatman, "Performance of 4-ary ASK for optical communication systems in dispersive, nonlinear environments," in 8th IEEE High Frequency Postgraduate Colloquium, Belfast, U.K., 2003, pp. 56–59.
- [8] S. Walklin and J. Conradi, "Multilevel signaling for increasing the reach of 10 Gb/S lightwave systems," *J. Lightw. Technol.*, vol. 17, no. 11, pp. 2235–2248, Nov. 1999.
- [9] N. S. Avlonitis and E. M Yeatman, "Performance of 4-ary ASK in Nonlinear, Multi-Channel Environments," *Proc. London Communications Symposium*, pp. 45 – 48, London, Sept 13-14, 2004.
- [10] David Gutierrez, Fu-Tai An, Jung Woo Lee and Leonid G. Kazovsky, "Increasing the Upstream Capacity of Passive Optical Networks by Pulse Amplitude Multiplexing", *Proceedings of IASTED OCSN WOC 2006*, July 2006.
- [11] M. L. F. Abbade, E. A. M. Fagotto, R. S. Braga, I. E. Fonseca, E. Moschim, and F. R. Barbosa, "Optical Amplitude Multiplexing Through Four-Wave Mixing in Optical Fibers," *IEEE Photon. Technol. Lett.*, vol. 17, no. 1, pp. 151–153, Jan. 2005.



- [12] Nobuhiko Kikuchi, "Intersymbol Interference (ISI) Suppression Technique for Optical Binary and Multilevel Signal Generation," *J. Lightw. Technol.*, vol. 28, no. 8, pp. 2060–2068, Aug. 2007.
- [13] N. Kikuchi, Member, K. Mandai, K. Sekine, and Shinya Sasaki, "Incoherent 32-Level Optical Multilevel Signaling Technologies," *J. Lightw. Technol.*, vol. 26, no. 1, pp. 150–157, Jan. 2008.



## 5. Regeneration (ORC, ISCOM, UoA, ICCS/NTUA)

### 5.1 Fibre-based regeneration

In present-day networks the regeneration functions are performed in electronic devices and therefore an O/E/O conversion is necessary. Thus the effort to develop the Reshaping and Retiming functions in a pure optical device is essential to enhance transparency, scalability, and flexibility in optical networks [1]. 2R and 3R regeneration preserves data quality and allows for improved transmission distances, thus enhancing transparency, scalability, and flexibility of optical networks. Moreover, wavelength conversion is important to avoid wavelength blocking at nodes of the optical networks.

Fiber-based schemes represent one of the most promising approaches to optical regeneration due to their ultrafast nonlinear response and design versatility [2].

The argumentation for the motivation behind simultaneous processing of multiple channels within the same device is also quite straight-forward, since it may potentially offer major technical and economic benefits. However, direct extension of the technique to the multi-channel regime is generally restricted by the presence of nonlinear interactions of the various wavelength channels as they are transmitted simultaneously through the same fibre, competing directly with SPM. These effects result in distortions of the broadened spectra which manifest themselves as large bit-pattern-dependent signal power fluctuations at the output of the system. These effects can be reduced to tolerable levels by ensuring complete and rapid “walk-through” of the data pulses – either by exploiting some form of specific chromatic dispersion management within complex fiber assemblies [3, 4, 5], by using dispersion decreasing fiber [6], or by using bi-directional propagation [7].

#### 5.1.1 Design of single channel OOK 2R regenerators

##### 5.1.1.1 Self-phase modulation based regenerator

The original all-optical signal regeneration scheme based on SPM in optical fibres was first reported by Mamyshev in [8], and is schematically illustrated in the block diagram of Figure 25. The degraded optical pulse streams are first fed into an optical amplifier which is used to boost the power to a suitable level at the input of the HNLF. The amplified pulses are then propagated in the HNLF where they experience spectral broadening due to Kerr-induced SPM. A narrow-band filter is used to carve into the broadened spectrum at the output of the HNLF discriminating high from low input peak power pulses and thus providing a pulse reshaping operation, as shown in Figure 25.

In the work reported herein, we consider transform-limited Gaussian pulses at the input, with a variable peak power  $P_{in}$  and a half-width at the  $1/e$ -intensity point  $T_0$ . Figure 25 lists the remaining parameters of the regenerator. The customizable parameters of the HNLF are the chromatic dispersion ( $D$  or  $\beta_2$ ), the nonlinearity coefficient  $\gamma$ , the fibre length  $L$ , and the attenuation coefficient  $\alpha$ . The output optical band-pass filter (OBPF) is detuned from the carrier frequency by an offset value  $\Delta F$ . In order to distinguish the impact of the amplified spontaneous emission (ASE) noise from the intrinsic ability of the regenerator to eliminate ghost pulses, we have not considered any ASE noise in our simulations.

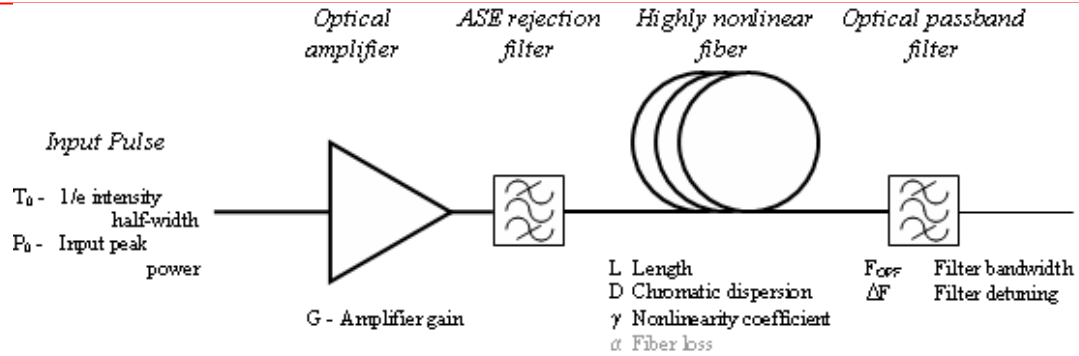


Figure 25: Schematic of a typical optical regenerator based on SPM.

The general performance of a 2R regenerator can be quantified by means of the power Transfer Function (TF) (output vs. input pulse peak power) of the system. Depending on the interplay between the broadened pulse spectrum and the detuned filter position, we distinguish three possible forms of TF behaviour depending on the detailed nonlinear pulse evolution and the resulting interplay with the filtering process (see Figure 26): A) non-monotonic variation; B) locally flat; or C) a monotonic variation with input peak power [9]. Generally speaking, a B-type TF will give optimum performance in terms of amplitude noise suppression on the ones. However, apart from this requirement, the optimal regenerator must also be designed to provide i) sufficient extinction for the zeros; and ii) reasonable energy efficiency. In order to parameterise the TF, we first set the nominal input peak power for the one bits  $P_1^{in}$  at the point where the absolute value of the derivative of the TF is minimised. We can then define  $\rho$  as the relative output power variation for input pulse powers ranging by  $\pm 7.5\%$  around  $P_1^{in}$ , and  $ER_{out}$  as the output extinction ratio value between one and zero bits when the input extinction ratio  $ER_{in}=0.1$ . These parameters are shown schematically in Figure 27.

As discussed in [9], the key TF parameters of the regenerator can be related to its physical properties. These relationships are shown in the multidimensional contour plot of Figure 4 [9], where  $L_{eff}$ ,  $L_D$  and  $N$  are the effective length, dispersion length and soliton number respectively, defined in [9].

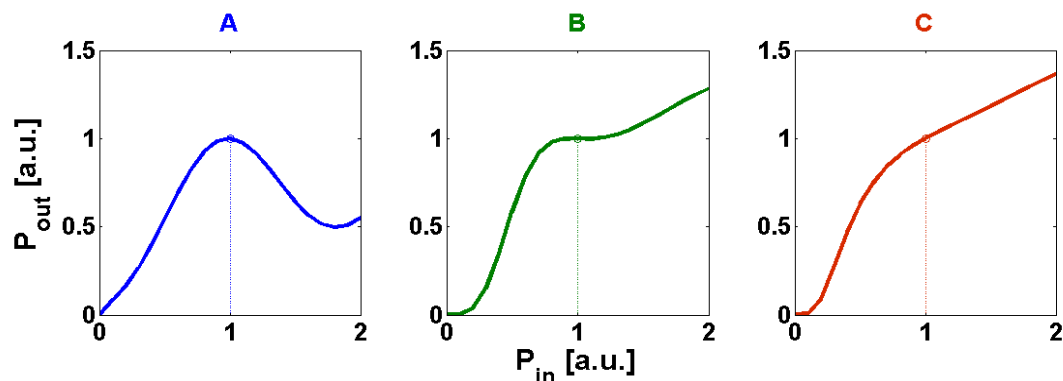


Figure 26: Illustration of the three possible TF types for the SPM-based regenerator: non-monotonic evolution (A), locally flat evolution (B), or monotonous variation (C).

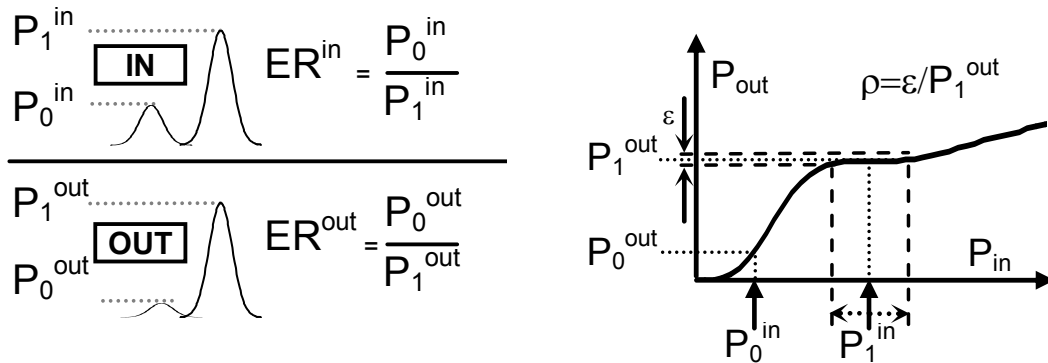


Figure 27: Definition of the parameters used to parameterize the power TF of the regenerator. Left: Definition of the input ( $ER_{in}$ ) and output ( $ER_{out}$ ) extinction ratios. Right: Example showing these corresponding parameters on a model TF.

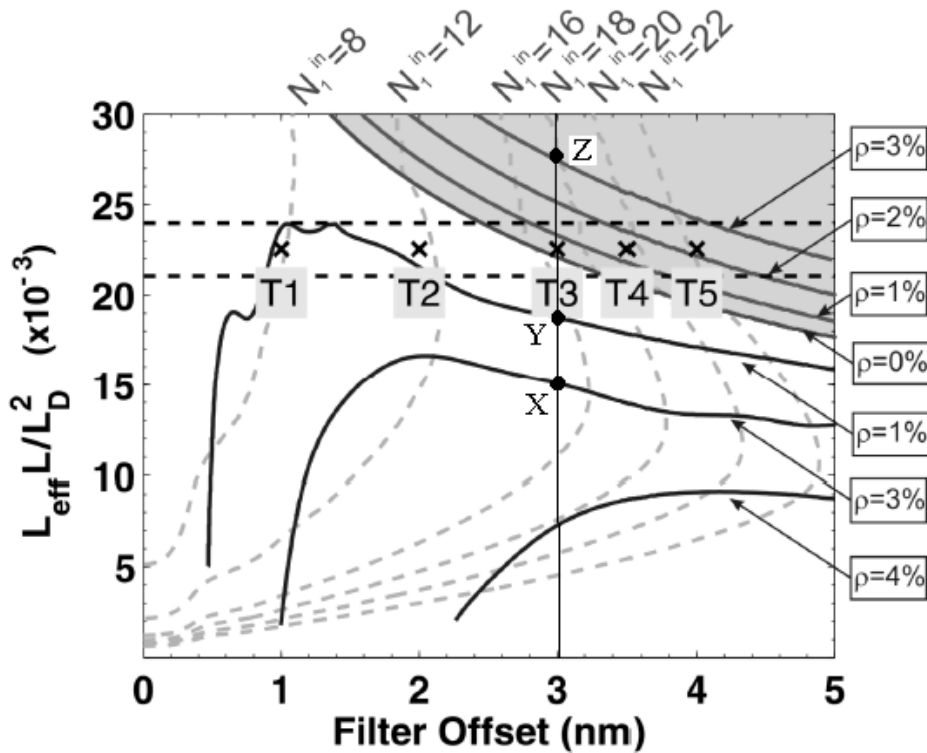


Figure 28: Contour map of a 2R regenerator based on a HNLF with 2.1 dB/km attenuation.

Although the effect of dispersion on the regenerator performance is evident in Figure 28, the map does not contain the effects of dispersion slope  $S$ , which are investigated in this deliverable. For this purpose, we chose three different operating points on the map, X, Y and Z, corresponding to the three different types of TFs, A, B and C respectively (see Figure 28), and study how the TFs of each of these points change as we vary  $S$ . For these simulations, we consider 6.7 ps Gaussian pulses at the input, and a HNLF with a  $\gamma$  of  $18 \text{ W}^{-1} \cdot \text{km}^{-1}$ ,  $D$  of  $-3 \text{ ps} \cdot \text{nm}^{-1} \cdot \text{km}^{-1}$  at the input wavelength, and  $\alpha$  of  $2.1 \text{ dB} \cdot \text{km}^{-1}$ . The 0.57 nm Gaussian filter is centred at a 3-nm offset (on the short-wavelength side) relative to the input. Considering these parameters, it is possible to move among the various points simply varying the length of HNLF: 0.56 km for point X, 0.59 km for point Y and 0.78 km for point Z. Points X and Z

have been chosen to give similar nominal value of the output peak power compression  $\rho$  (3%) when the dispersion slope is neglected.

Figure 29 shows an example of the temporal and spectral profiles of the pulses at the output of the HNLF for various values of  $S$ . The input peak power is 36.5 dBm and the length of HNLF is 0.6 km, whereas the remaining system parameters are the same as mentioned above. As expected, an increase of the dispersion slope gives rise to an asymmetric spectrum and hence the power on the two sides of the central wavelength is not equal. In particular, as the magnitude of  $S$  increases, the side of the spectrum that corresponds to higher power components in the temporal profiles of Figure 29(a) experiences a broader spectral broadening (longer wavelengths in Figure 29(b)), while opposite behaviour takes place for the lower power components. This effect causes the value of  $\rho$  to vary, allowing us to improve or worsen the shape of the TF. In the simulations, the filter position is arbitrarily chosen to be on the short-wavelength side of the spectrum. It is worth noting, that should we wish to place the filter on the long-wavelength side, then we would need to invert the sign of  $S$  in the calculations, in order to obtain the same conclusions.

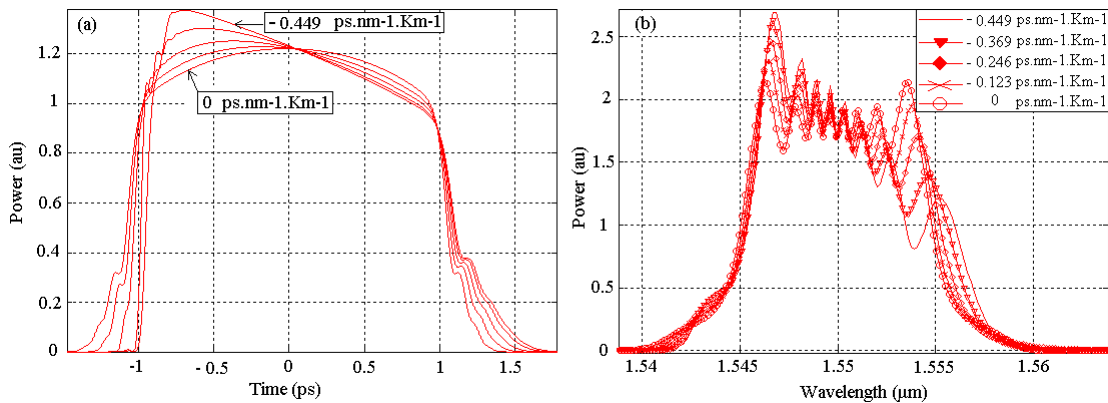


Figure 29: Effect of dispersion slope on the (a) temporal and (b) spectral profile of pulses at the output of the HNLF.

We first study the evolution of the TFs for point X. The results are shown in Figure 30(a) for various dispersion slopes, where only the top sections of the TFs (corresponding to the power equalisation of the ones) are displayed. We focus on this part of the TF, since a change in  $S$  is not expected to have a great effect on the equalisation of zeros. From Figure 30(a) it can be seen that increasing the magnitude of  $S$ , we move from an A- type TF to a B- and C- type TF. Correspondingly, the output peak power compression improves as the magnitude of  $S$  increases, reaching the minimum value of  $\rho=0\%$  for  $S = -0.123 \text{ ps/nm}^2.\text{km}$  to degrade again if  $S$  is further increased, moving to C-Type TFs.

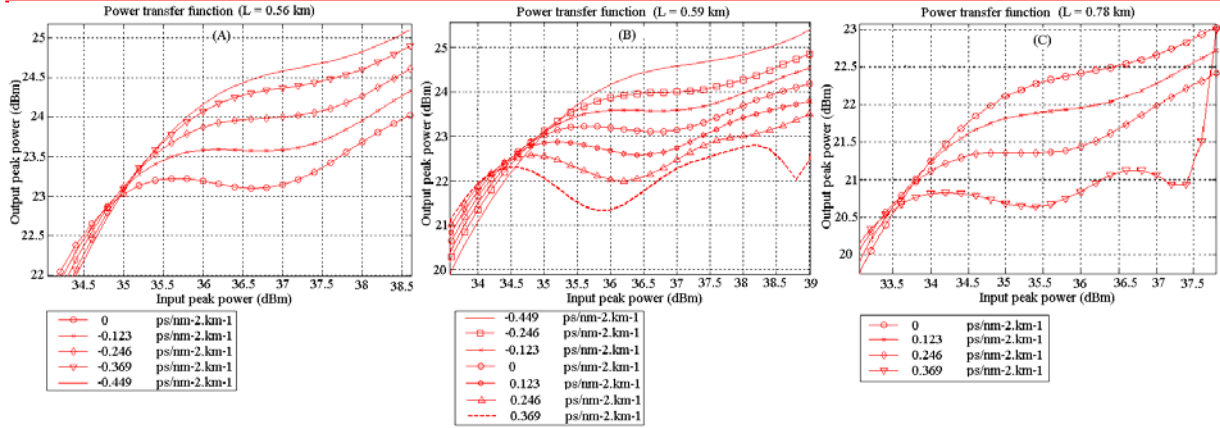


Figure 30: Power TFs for varying values of  $S$ . (a) Point X. (b) Point Y. (c) Point Z.

We next consider point Y, which corresponds to a B-type TF ( $\rho = 0\%$ ) when  $S = 0$ . As shown in Figure 30(b), as we increase the magnitude of  $S$ ,  $\rho$  increases, and the TF becomes either of an A- or C-Type, depending on the sign of  $S$ . As an indication,  $\rho = 1\%$  when  $S = 0.123$  ps/nm<sup>2</sup>.km, and  $0.5\%$  when  $S = -0.123$  ps/nm<sup>2</sup>.km.

By further increasing the length of fibre, we move to point Z on the contour plot of Figure 28, which corresponds to a C-Type curve with  $\rho = 3\%$  when  $S = 0$ . As shown in Figure 30(c), the TFs tend towards a B-Type curve as the value of  $S$  increases, whereas further increase of  $S$  gives rise to a non-monotonic TF (Type A). For this to happen of course, the sign of  $S$  needs to be opposite than that applied previously for point X. In this case, to achieve a B-type TF with  $\rho = 0\%$ , the dispersion slope has to be  $S = 0.246$  ps/nm<sup>2</sup>.km.

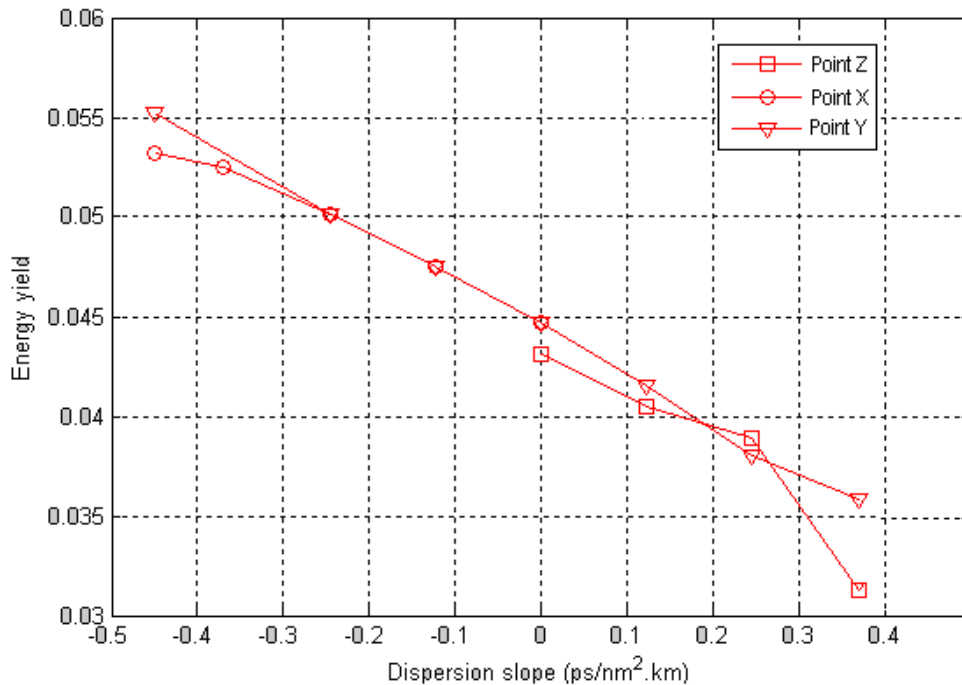


Figure 31: Energy yield at P1 in as a function of the dispersion slope

As mention above, the possibility of varying the dispersion slope allows us to move along the x-axis of the contour map of Figure 28, while keeping the other parameters constant. Its magnitude increase is beneficial in the case of a relatively short HNLFF which exhibits a Type B TF by virtue of a high  $S$  (such as in the case of point X). Indeed, this regenerator will exhibit an increased energy yield, since the filter is placed on the high-power side of the spectrum. Note that the energy yield is defined as the ratio of the power at the output of the filter to the power at the input of the HNLFF. On the other hand, a relatively long HNLFF with a high value of  $S$  may exhibit a Type B TF (point Z in the above discussion). However, since the filter sits on the low-power part of the spectrum, the corresponding energy yield of the regenerator decreases. Figure 30 summarises these results by showing the variation in energy yield at the nominal input peak power as a function of the dispersion slope for the three points considered above.

In conclusion, when a HNLFF with a high dispersion slope is used for regeneration, it is important that the value of  $S$  is taken into account in the system design, since it can play an important role to improve the regenerator performance.

#### A5.1.1.2 Induced phase modulation on an Auxiliary Carrier

##### A5.1.1.2.1 Experimental Set-up

The main element in the experimental demonstration shown below is a dispersion shifted (DS) fiber which acts as the nonlinear element (loss  $\alpha=0.2$  dB/km, nonlinear coefficient  $\gamma=2.2$   $[\text{W}\cdot\text{km}]^{-1}$ , chromatic dispersion  $D=0.19$  ps/nm km @1542.14 nm, dispersion slope  $S_0=0.0634$  ps/nm<sup>2</sup>km and differential group delay (PMD factor) DGD=0.13 ps, overall length of 10 km). This special fibre is obtained in a single fabrication process, without splicing. This feature limits the fluctuation of the zero dispersion wavelength (around 1539 nm) responsible for the reduction of parametric gain and gain bandwidth and also for issues relating to maintenance of a fixed phase relation between the interacting waves [10]. Figure 32 shows the set-up. The signal is generated by the Transmitter, constituted by a DFB laser ( $\lambda=1542.9$  nm) and an intensity modulator (IM) driven by a 10 Gbps PRBS generator (PRBS length  $2^{31}-1$ ). After attenuator ATT1 the modulated signal is fed to the 2R regenerator. The optical amplifier allows us to set the value of signal power for optimum reshaping function.

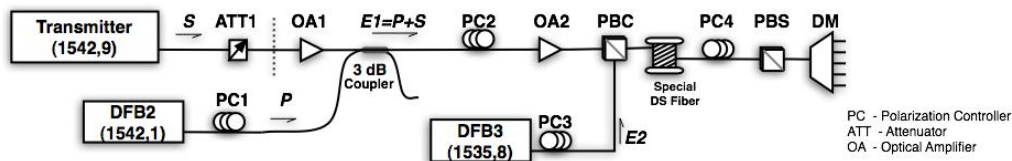


Figure 32: Set-up of the experimental device

DFB2 generates the pump at  $\lambda=1542.1$  nm; polarization controller PC1 brings the pump on the same state of polarization as the signal. A 3dB coupler couples pump and signal. The overall optical field ( $E1=S+P$ ) is then processed by a block made up of a polarization controller (PC2) and an optical amplifier (OA2) that increases the power of the pump and the signal up to the power needed in the non-linear process ( $\sim 80$  mW). A polarization beam combiner (PBC) is used to couple, at the entrance of the DS fiber,  $E1$  with a new auxiliary carrier signal  $E2$  ( $\sim 5$  mW - 1535.8 nm). In this way, these fields are both forced to be on linear orthogonal States Of Polarization (SOPs) by means of PC2, PC3 and the PBC. Another



polarization controller (PC4) and a polarization beam splitter (PBS), placed at the DS output, allow us to filter one state of polarization of the output.

The beating of signal and pump near  $\lambda_0$  in non-linear regime causes, via the optical Kerr effect, modulation of the fiber refractive index. The whole field propagating along the fiber will consequently be phase modulated with a modulation frequency equal to the pump-signal detuning ( $\omega_p - \omega_s$ ) [11, 12 and 13].

It is well known that an angular modulated signal may be resolvable as the summation of infinite sinusoidal terms with the general pulsation of  $\omega_0 + n(\omega_p - \omega_s)$  and amplitude  $J_n(x)$ , where  $J_n$  is the Bessel function of the first kind and  $x$  is the modulation index. In our case the modulation index depends on the geometric average of the power of pump and signal, the non-linear coefficient  $\gamma$ , and the length of the non-linear medium (the DS fiber). This phenomenon can be modelled from the non linear Schrödinger equation. Concentrating the attention on the non-linear element, we obtain the expression of the approximated field subject to the non-linear effect

$$E(z, t) = E_0(t) \exp(i\gamma |E(t)|^2 z)$$

where 
$$E_0(t) = E_p e^{-i\omega_p t} + E_s e^{-i\omega_s t} + E_{ac} e^{-i\omega_{ac} t} \tag{1}$$

$E_0$  is the input field. In our system  $E_0$ , the sum of two strong components, Pump and Signal, at frequencies  $\omega_p$  and  $\omega_s$ , participating in the non-linear process, and the auxiliary carrier, at frequency  $\omega_{ac}$ ; the auxiliary carrier is too weak to take part in the generation of any non linear processes but it will be affected by it. We can express the approximated field propagating into the fiber as

$$E_0(t) = e^{i\gamma z P_{tot}} e^{2i\gamma z \sqrt{P_s P_p} \cos((\omega_p - \omega_s)t)} \left( E_p e^{-i\omega_p t} + E_s e^{-i\omega_s t} + E_{ac} e^{-i\omega_{ac} t} \right) \tag{2}$$

Where  $P_{tot}$  is the total power of the incoming signals. This expression describes a phase-modulated signal. The exponential of cosine can be expanded in Bessel Series:

$$E_0(t) = e^{i\gamma z P_{tot}} \left( E_p e^{-i\omega_p t} + E_s e^{-i\omega_s t} + E_{ac} e^{-i\omega_{ac} t} \right) \left( J_0(2\sqrt{P_p P_s} z \gamma) + \sum_{n=1}^{\infty} 2e^{\frac{i n \pi}{2}} J_n(2\sqrt{P_p P_s} z \gamma) \cos [t(\omega_p - \omega_s)] \right) \tag{3}$$

The main comb (Comb1) in the SOP of E1 is induced by the phase modulation and arises directly from the beat of P and S. In the SOP of E2, orthogonal to the first one (E1), there is a second comb (Comb2), in the area of the injected third auxiliary carrier, as reported in Figure 33; Comb2 is produced by the phase modulation induced on E2. The second comb, Comb2, reproduce the first comb but at the converted wavelength. In this way we increase the conversion range reducing, moreover, the noise extracting the converted signals from Comb2 [1].

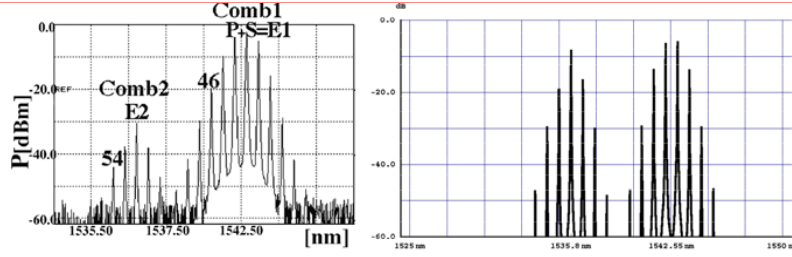


Figure 33. Comparison of real (left) and simulated (middle) optical output

From equation (3) we can perform a simulation of the output field, Figure 33, and obtain the theoretical description of the transfer functions of each replica of the two combs, equations (4) and (5).

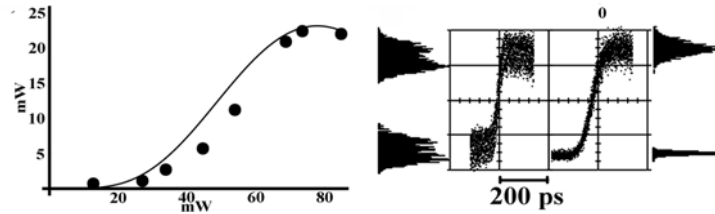


Figure 34 Transfer function and the measure of noise reduction (right)

$$P_n(P_s)_{Comb 1} = P_p \left[ J_{n-1} \left( 2\gamma z \sqrt{P_s P_p} \right) \right]^2 + P_s \left[ J_n \left( 2\gamma z \sqrt{P_s P_p} \right) \right]^2, \quad n=1,2,3,\dots \quad (4)$$

$$P_m(P_s)_{Comb 2} = P_{AC} \left[ J_m \left( 2\gamma z \sqrt{P_s P_p} \right) \right]^2, \quad m=1,2,3,\dots \quad (5)$$

The Bessel-like behaviour of the transfer functions (Pout vs. Pin) has been demonstrated and in Figure 34 we report a measurement of the capacity of the higher order characteristics in reshaping the signal. This feature depends on a non-zero threshold and a spread maximum that we can exploit for reshaping use. In fact, by adjusting the signal and pump power ( $P_p, P_s$ ), at the DS fiber input, it is possible to choose the better working point in order to erase the noise of an incoming corrupted signal over both the zeros and the ones [1, 12, 13, 14].

#### A5.1.1.2.2 Discussion

The non-linearity at the base of the process is able to phase-modulate not only the optical beating field, that induces the non-linearity itself, but any kind of other optical carrier propagating through the fiber 1535.8 nm in this case. Subsequently, the optical spectrum of this new carrier will present a series of components, each one reproducing the high data rate amplitude modulation of the original incoming signal and each one with the same Bessel-like transfer function.

In Figure 35 we report the BER results obtained at 10 Gbit/s, in both the back to back configuration and in propagation, for the ITU-GRID channels 54 (1534.2 nm) and 46 (1540.5 nm). The propagation was performed using a cable deployed between the cities of Rome and Pomezia encompassing different kind of fibres, G.652, G.653 and G.655. The better performance on the Ch.54 depends on the better signal to noise ratio respect to the Ch. 46.

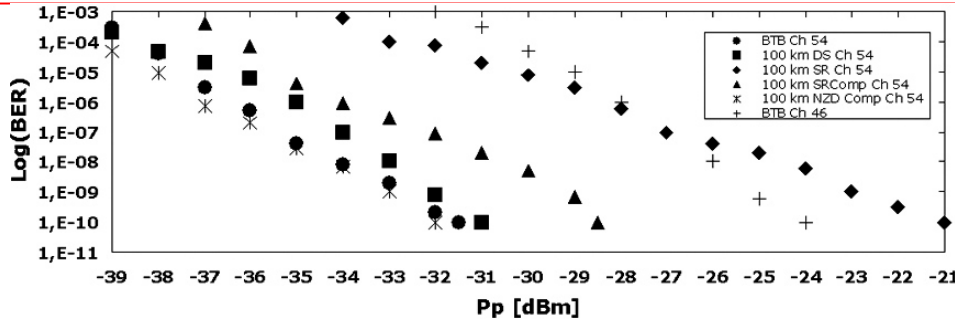


Figure 35: BTB and propagated BER measurements vs received power for ITU Ch 46 and 54.

In Figure 36 we report the measures of the amplitude of the first four replicas in function of the input signal power (dotted line). For each replica we also report (continuous line) the simulations of the correspondent characteristic derived from equations (4) and (5). It is evident that the in-out power-transfer characteristic of the  $n$ -th order replica is alike to the correspondent order Bessel function which argument is proportional to the root square of signal power through the non-linear coefficient of the fiber. The use of a low power auxiliary carrier (E2) with an orthogonal SOP, respect to E1, is a way to reduce the detrimental effects due to spurious non-linearity directly induced by high powered pump and signal. Furthermore the optical signal to noise ratio (OSNR) related to the replica of Comb2, could be simply enhanced just by increasing the power of E2 [1].

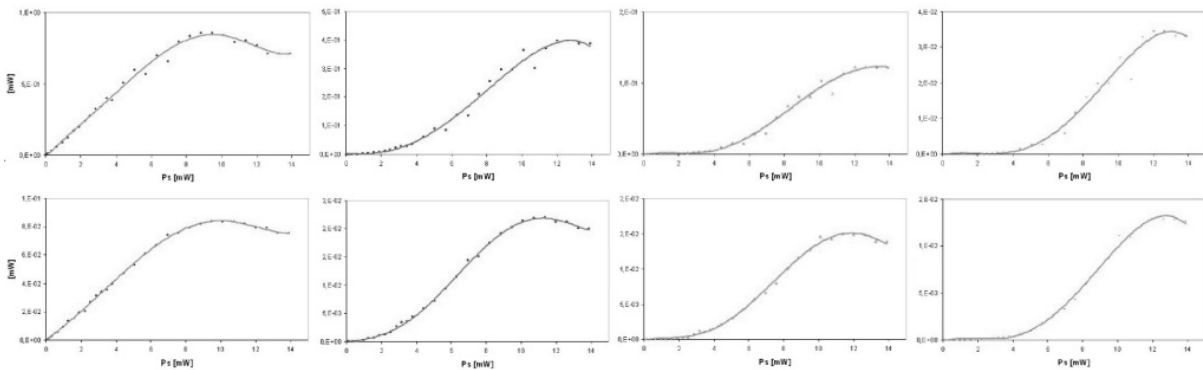


Figure 36. Measured (dot line) and simulated (continuous line) characteristics of the first four replicas of the Comb1 (superior series) and of Comb2 (inferior series).

In this kind of non-linear process where two or more signals at different wavelengths, propagate into a DS fiber with different group velocities the dispersion plays a critical role. Having the field generating the non-linearity near  $\lambda_0$  (1539 nm in our special DS fibre) reduces the phase mismatch between the two components of E1, thus enhancing the significance of the non-linear effect. Moreover the low wavelength fluctuation of  $\lambda_0$  is a further way to maximize the Multi Wave Mixing phenomena and the efficiency in the power transfer to the generated replicas.

The group velocity trend inside an optical fiber is similar to a parabolic curve with his minimum at the zero dispersion wavelength,  $\lambda_0$ . Then, the closer the group velocity of E2 (DFB3) is to the group velocity of E1 the better the efficiency of the process that induces the generation of Comb2 when the auxiliary optical carrier is injected into the DS fibre. In our special fiber the wavelength with the more suitable associated group velocity is 1533 nm.

Indeed, as reported in the Figure 37, the generation of the auxiliary carrier side bands (Comb2) has maximum efficiency around 1533 nm.

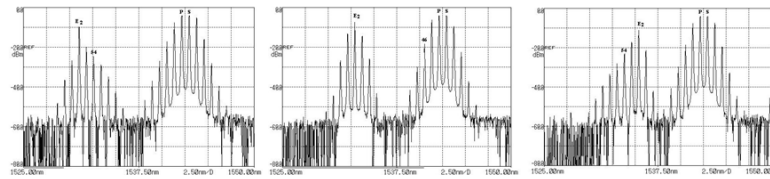


Figure 37. Different configuration of Comb2 obtained emphasizing via PC4 and PBS the SOP of E2. In the three cases we take different wavelength for E2 in the surroundings of the maximum efficiency frequency ( $E2 = 1531.4, 1533, 1534.5\text{nm}$ )

## 5.1.2 Multi channel OOK 2R regenerators

### 5.1.2.1 2R regeneration step exploiting the FWM non linear effect

In the recent years the improvement in optical device technologies and optical telecommunication systems has been remarkable. Thus, in just a short time, all optical processing of signals has become a reality. Moreover WDM and DWDM techniques, have made the simultaneous transmission of several data clients in each optical fiber possible. This permits a growth of data traffic for each optical cable of Tbit/s but, for this reason, an interruption of communication, even just for a few instants, can provoke serious damages in terms of data loss, especially using today's high bit rate. Mobile phone (GSM and UMTS), Cat-TV, internet, IP TV, P2P services, video calling and other services can require a high data rate. To the other end, there can be several kilometers of optical fibre between one data processing node and the following one, and this involves the uses of one or a chain of optical amplifiers. Every amplifier step can be equipped from a regenerator system; in this way, the data elaboration unit can offer an amplifier and regenerations section.

These kinds of systems must be able to guarantee the high bit rate demanded by the several clients; in fact the optical cables can offer robust services and a very large bandwidth. The O/E/O data conversion used to manage the data client must be, where possible, avoided because it needs more processing time with respect to the time needed from all optical systems and all optical signal management. O/E/O conversion implies electrical regeneration and this provokes a bottleneck effect in every regeneration step of the system.

In the literature there are several systems achieving 2R regeneration operation based on different theories. Supercontinuum system can be achieved to obtain a 2R regeneration operation; interferometric structures use the nonlinearity of media to realize the regeneration effect. Saturable absorbers, Q-switched lasers and semiconductor devices can be used to obtain the same noise compression and signal regeneration. Our attention is on a particular kind of optical fibre and the non linearity that this presents. Using a DS fibre, in fact, it is possible to realize a 2R regeneration step exploiting the FWM non linear effect (as shown in the previous section). This kind of system can be used also in a WDM scenario, like regenerators based on nonlinear optical loop mirrors or on dispersion compensation maps.

The systems based on a FWM non linear effect can realize also a wavelength conversion and the properties can be used when one or more systems do not accept a particular wavelength. Thus, if we want access in a network but it does not work with our wavelength, we must realize wavelength conversion before run through this network. The second characteristic of

2R system is that it is able to manage one or more signals at the same time; in fact, we can find single-channel or multi-channel 2R regeneration systems. The single-channel system can manage only one client and in a WDM scenario we must use several step, one for each client.

Our 2R regeneration system is based on a non linear optical fibre able to generate several replicas of the incoming signal. These replicas have the same modulation format as the original signal and their presence is due to the beating between pump signal and client signal. The transfer function of the replica is like the Bessel function and guarantees the compression of the noise present in the client signal. In this way, a wavelength conversion and the data regeneration is obtained. If the pump power is very high and around the zero dispersion wavelength of the optical fibre, we are able to obtain more replicas with different behaviors. Using a polarization beam splitter (PBS) is possible to handle two paths at same time starting from one modulated signal placed at one wavelength. At the output from PBS there are two orthogonal components and the pump signal is divided at 50% to each path to guarantee the reshaped function.

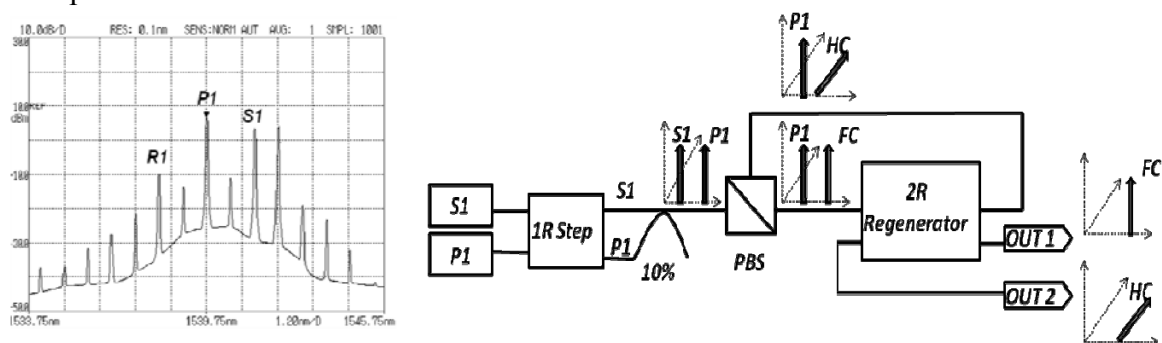


Figure 38. Set-Up used for the experiments. FC first component, HC orthogonal component. Output spectrum (on the right) referred to First Component.

The configuration reported in Figure 38 uses a DFB source placed at 1541.350 nm (S1) to simulate a client signal and an ECL source (P1) as pump signal placed at 1539.820 nm. S1 is modulated by an external Mach-Zehnder modulator at 10 Gbit/s NRZ PRBS. After 1R section, S1 and P1 are coupled with a 10% coupler; then, there is a PBS to obtain two different orthogonal paths and two polarization controllers (not in figure) are used to distribute the right pump power at two signals. The system is now able to manage two different clients using only one wavelength. Exploiting a particular DS optical fibre (present in 2R Regenerator step) and its non linear effect, each orthogonal component will send in a different way of the DS cable. In fact, FC component is send, coupled with the pump signal, from input to output of the optical DS fibre and the HC component is send, coupled with the pump signal, from output to input of the optical fibre; in this way two signals that run trough in the optical fibre will see different parameter, thus two components uses the same optical medium.

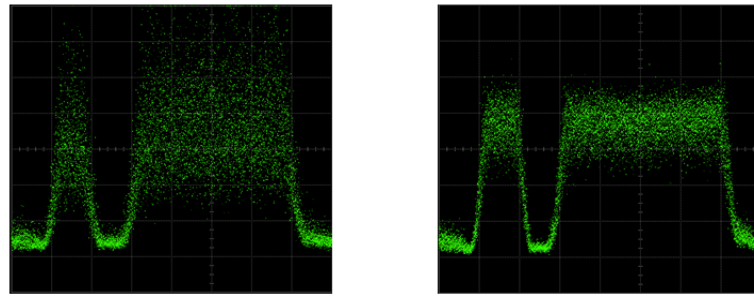


Figure 39: Noise (on the left) and regenerated signal (on the right).

A thin-film filter has been used to select the right order of replica and to remove the other unwanted signals. The first replica that we have selected, has the properties to obtain a noise compression to the mark level. The system works with two regenerated signals at the same time without interference; this is guaranteed by the orthogonal polarization state of the signals. The system uses two amplifiers for each path and a chain of amplifiers for the pump way to obtain the right pump power. To reach this result we have used a pump power value around 10 dBm distributed for each path.

Figure 39 shows the signal before and after the regeneration operations. This refers to the first components, but the result for the orthogonal signal is the same. Selecting the right working point of the replica transfer function the system is able to compress the noise on the mark level and give back a reshaped signal as shown in the figure.

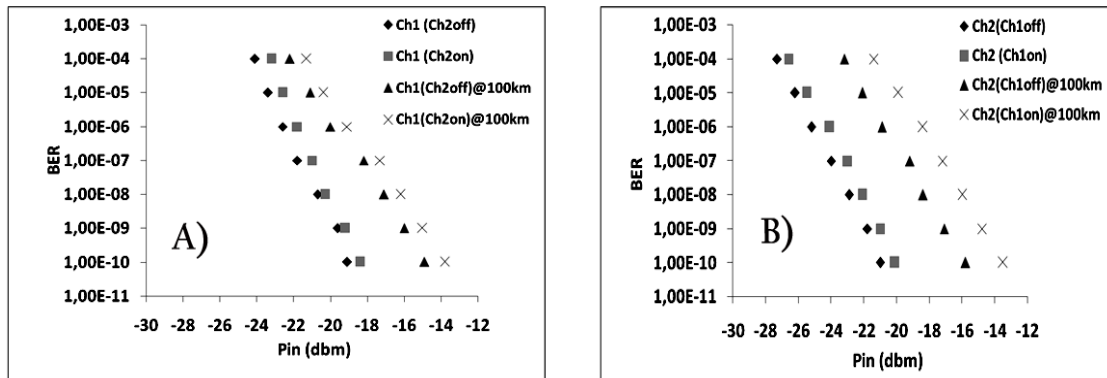


Figure 40: BER measurements.

BER measurements have been evaluated in back to back and propagation conditions. We have used 100 km deployed DS optical cable placed between Rome and Pomezia. In both conditions no error-floor has been observed. Figure 40 (a) and (b) show the BER measurements for Channel 1 and Channel 2, respectively, either in the presence or absence of the second path, in this case intended as the interfering signal. The difference between the presence or absence of interfering signals is very small, the penalty is only 0.7 dB at  $1.00 \times 10^{-10}$ ; in this way this system can manage more signals without interference. Propagation along 100 km of deployed cable is of course worse in terms of BER, with respect to the values of the regenerated signals.

In WDM and DWDM scenario, a single channel system will be replaced from multi-channel regeneration systems. In fact, our system is a first approach to the multichannel configuration which becomes a fundamental step in the context of all optical regeneration. Instead of using a 2R single channel regeneration system to each client in the WDM scenario, is it better, in

terms of cost and power consumption, to use a multichannel system for all clients present in the optical network.

#### A5.1.2.2 Four-channel extension to the Mamyshev regenerator

##### A5.1.2.2.1 Experimental set-up

In this Section we demonstrate a four-channel extension to the Mamyshev regenerator [8] and investigate its potential for the simultaneous processing of  $4 \times 10$  Gb/s return-to-zero (RZ) wavelength division multiplexed channels. As previously discussed, a direct extension of the technique to the multi-channel regime is generally restricted by the presence of nonlinear interactions of the various wavelength channels as they are transmitted simultaneously through the same fibre, competing directly with SPM. These effects result in distortions of the broadened spectra which manifest themselves as large bit-pattern-dependent signal power fluctuations at the output of the system.

In order to reduce the detrimental effects of nonlinear crosstalk, it is required that the pulses in the various channels exhibit an effectively large walk-off between them during their propagation in the nonlinear fibre. To this end, we can directly observe that the largest walk-off rate between any two signals is obtained when these propagate in opposite directions. Then the regenerating system can be optimised separately for each direction. This approach takes advantage of the rapid walk-off induced by both the large DGD of a specially developed PM-HNLF and a bi-directional architecture. Numerical and experimental results demonstrate the reduction of inter-channel cross-talk as well as the potential of the scheme for 2R regeneration.

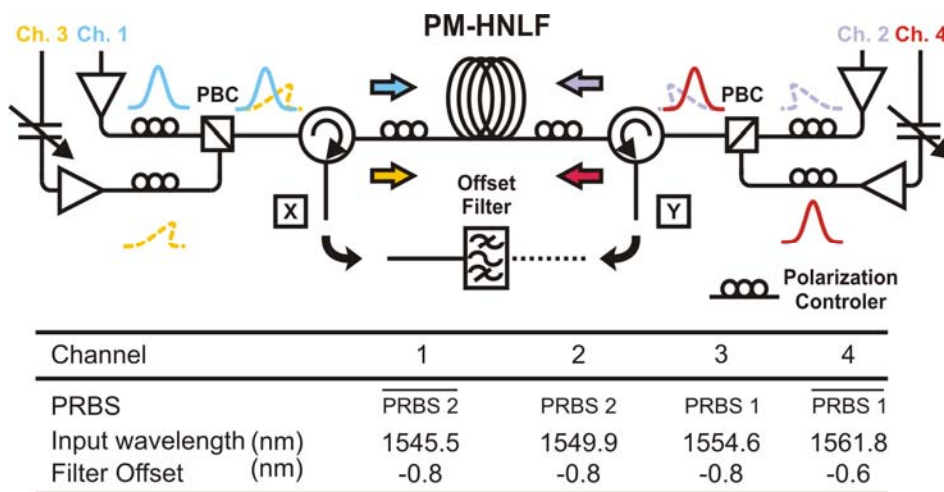


Figure 41: Experimental set-up and corresponding channel properties.

By implementing this approach in a bi-directional architecture, as previously discussed, simultaneous processing of four WDM channels is possible. The corresponding experimental set-up is reported in Figure 41. Four 10 GHz pulsed data streams were generated by Gain Switched (GS) laser diodes with pulse durations of 7-8 ps. All channels were individually amplitude modulated with  $2^{31}$ -long PRBS. The corresponding channel carrier frequency and PRBS allocation are reported in Figure 41. Each channel was then individually amplified and fed into the PM-HNLF via a polarization beam combiner (PBC). Two optical circulators separated the transmitted and the reflected signals from the HNLF at both fiber ends. Finally, a 0.53-nm bandwidth tunable optical filter at port 3 of the circulator acted as the reshaping

and decision element (see Figure 41 for the corresponding relative offsets). The PM-HLNF was 1-km long and has a chromatic dispersion value of  $-4.2$  ps/nm/km at 1550 nm (slow axis) for a nonlinear coefficient of  $\sim 20$  W<sup>-1</sup>.km<sup>-1</sup>. The birefringence value was as high as  $\sim 7 \times 10^{-4}$  corresponding to a DGD value of  $\sim 2.3$  ps/m. The fiber has a loss of 4.2 dB/km and a nominal polarization extinction ratio of -30 dB (over 100 m).

A slight difference in the spectral broadening was observed between the two axes of the fiber under single channel operation which we attribute to the opto-geometrical/loss anisotropy existing between the two polarization axes. This variation was compensated for by adjusting the input power accordingly. Due to the lack of sufficient high power amplifiers in our laboratory, we reduced the filter detuning for Channel 4 slightly and allowed a small power penalty for Channel 2, thereby permitting use of lower power amplifiers within the system.

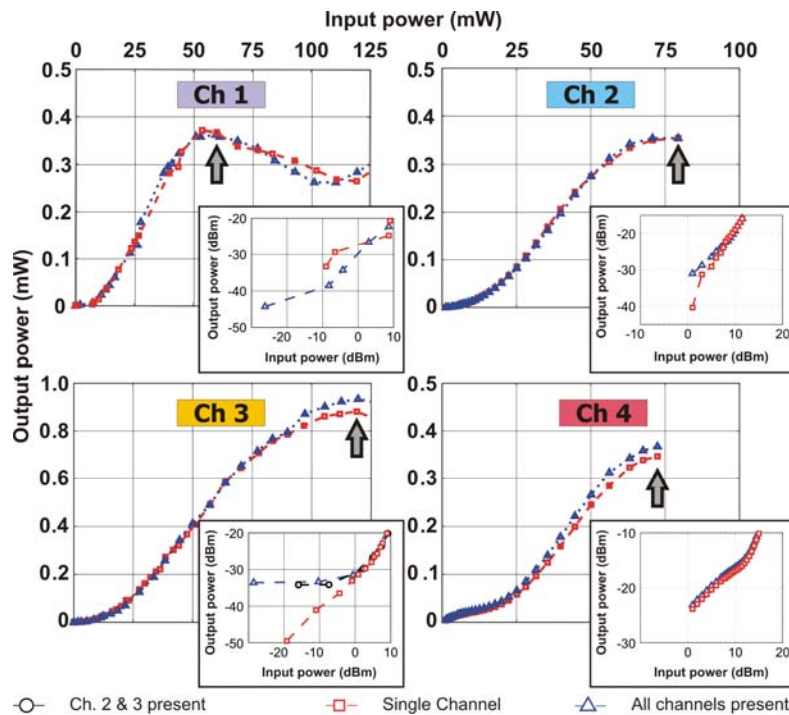


Figure 42: Experimental TF obtained for the four channels in both the absence and presence of the interfering channels. The arrows indicate the corresponding operating input powers. Inset graphs detail variations at low input powers (logarithmic scale). Input powers measured at the fiber inputs.

#### A5.1.2.2.2 Results

First, we assessed the device characteristics in terms of the static power TFs for each channel propagating in isolation. As reported in Figure 42, the four channels exhibit somewhat different TFs, which originates predominantly from the noticeably different characteristics of the input channel pulses (spectral bandwidth, presence of side-lobes and residual chirp, etc.) and which translates into noticeably different SPM-broadened spectra (see Figure 43). We then compared the TFs obtained in the presence of all interfering channels operating at the nominal operational input power. Optical delay lines were adjusted to ensure maximum pulse interaction between the co-propagating signals. This was achieved by maximizing the generated Four-Wave Mixing components, observed when the launched signals were co-polarised. As can be seen in Figure 42, the various TFs overlap well, illustrating the absence of strong inter-channel cross-talk amongst the various channels. As already pointed out in the previous sections, for low input powers, we clearly observe cross-talk that manifests itself as

a constant power floor and which has a different value according to the particular channel considered (see inset Figure 42). This is due to additional spectral components that fall within the offset filter bandwidth. Depending on the considered channel, this power floor originates either from the co-propagating signal, or from the backscattered contribution of the counter-propagating signal. A more visual illustration can be found in Figure 43 where transmitted, backscattered, and output pulse spectra are plotted. The presence of this additional collected power results in a slight decrease in the extinction ratio of the various channels, which is primarily due to the particular channel allocation chosen.

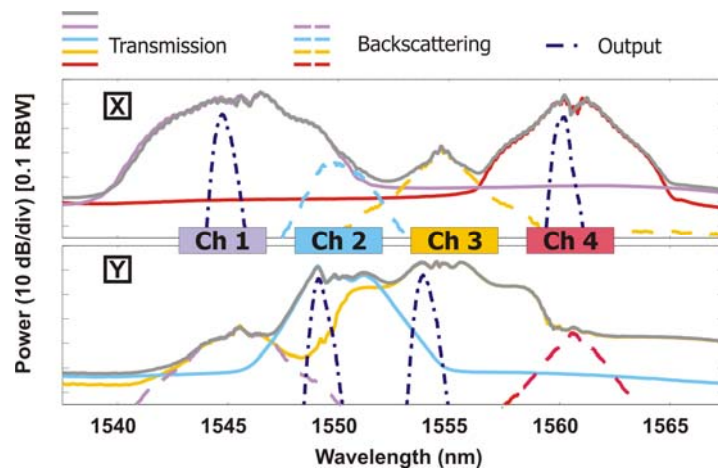


Figure 43: Single- and multi-channel spectra obtained at fiber output ports X and Y, and output channels (all channels operating at nominal input operating powers).

BER measurements were carried out for the four channels both under single- and multi-channel operation (Figure 44). As compared to the back-to-back case, our experiments confirmed that the system does not introduce any additional power penalty when operating in a single channel configuration (except for Channel 2), and similar performance is obtained when operating in the presence of the other channels. By selecting a sub-optimum bias voltage setting for the modulator, we then artificially degraded Channel 3, which we believed presented the worst cross-talk scenario. A power penalty improvement of up to  $\sim 1.8$  dB (at  $\text{BER}=10^{-9}$ ) can be obtained under both single and multi channel operation. The corresponding eye-diagrams show both simultaneous amplitude equalization and noise rejection in the empty slot.

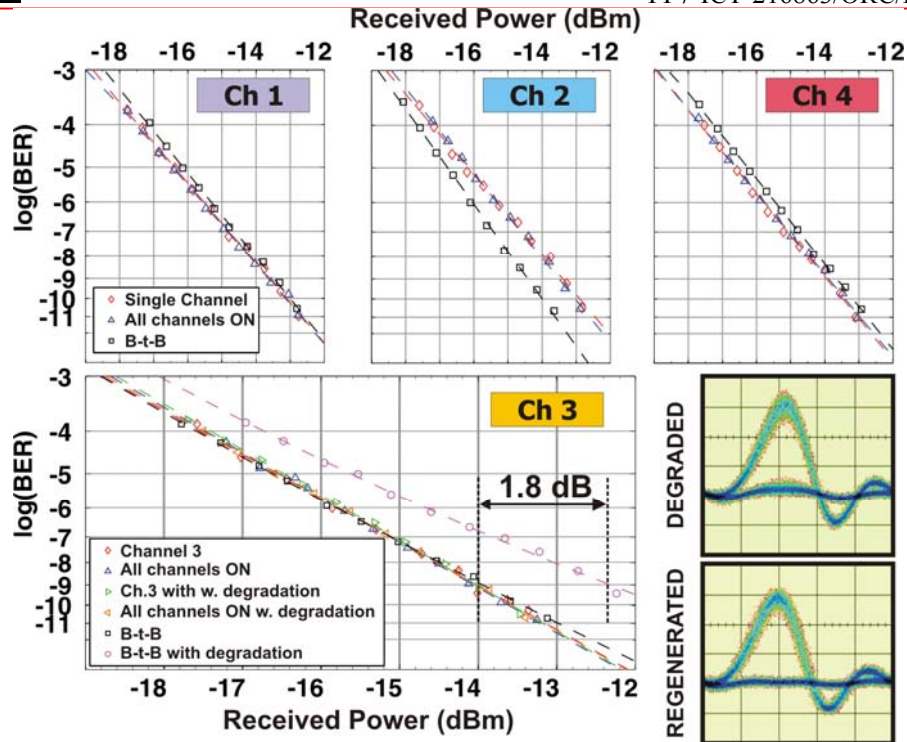


Figure 44 . BER measurements of the four channels in the absence and presence of interfering channels. The additional BER curve for Channel 3 corresponds to the degraded signal case. Corresponding eye diagrams of the input degraded and output regenerated data stream.

### 5.1.3 3R Regeneration OOK

#### 5.1.3.1 Introduction

The growth of network data traffic, mainly driven by new services and applications, has been a market driver in the TLC (Telecommunication) segment. High speed internet, email services, 2G and 3G mobile phones, video-calling and conferences, symmetric peer to peer, remote storage, e-services, avatars and community applications (facebook, linkedin) are only a few examples of new available services and applications. All these entities involve an intensive use of the network resources, thus a system able to support very high bit rates is necessary [15]. Interruptions and congestions of the networks can provoke serious damages for the users, especially at today's data rate. Thus, the O/E/O conversion must be avoided, or be extremely limited, and devices able to guarantee an efficient wavelength allocation enhancing the QoS and at the same time reducing the network congestion, without domain conversion, is the only way to create robust services [16, 17]. Using optical networks, the rates can increase also with a WDM approach, which make several optical carriers available thereby multiplying the overall capacity.

Different devices have been proposed to realize the 2R regeneration function, using interferometric structures, saturable absorber, EA modulators, parametric amplification, non linear fibers or semiconductor devices. In recent years, strong attention has been devoted to WDM signal regeneration due to the development of WDM communication systems. WDM regenerators based on nonlinear optical loop mirrors or on dispersion compensation maps have been proposed [18, 19, 20 and 21].



3R, in particular, regeneration with wavelength conversion capabilities is considered a key-function able to preserve data quality and allow for improved transmission distances, thus enhancing transparency, scalability, and flexibility of optical networks. Several groups have worked on the realization of 3R systems with and without wavelength conversion capabilities and several products are now on the market. OKI, for example, developed an all-optical 3R-Regenerator, which uses a specialized optical-repeater technology with functions for re-amplification, re-shaping to remove optical signal wave distortion, and re-timing to avoid timing jitter accumulation. The OKI 3R works at 160 Gbps on a single channel. KDDI developed a 40 Gbps 3R regenerator based on EA modulator able to assess the WDM TLC transmission needs. Our approach, in a single channel scenario, is mainly based of a dispersion shifted fibre, as 2R core, and on a SOA based ring laser, as retiming core.

Regarding the Re-shaping and the Re-amplification unit (2RU), simulations and experimental results, at 10 Gbit/s, are presented. Wavelength conversion and 2R regeneration through the characteristic non-linearity of a particular dispersion shifted optical fiber has been studied and achieved [22]. In that cases the envelope of the beating between a CW pump and a modulated signal, near the zero dispersion area (around 1539 nm), determined a phase modulation of the whole incoming optical field generating new frequencies spaced by the pump-to-signal detuning range. The non-linearity at the base of the process is able to phase-modulate not only the optical beating field that induce the non-linearity itself, but any kind of other optical carrier propagating through the fiber. Subsequently, the optical spectrum of this new carrier will present a series of components each one reproducing the high data rate amplitude modulation of the original incoming signal enhancing, in this manner, the overall device wavelength conversion range. Furthermore, because of the nature of the non-linear effect, the in-out power-transfer characteristic of the n-th order replica is alike to the correspondent order Bessel function and a reshaping function occurs.

Regarding the Clock Recovery unit (CRU), the attention has been focused on a circuit based on a fiber ring laser, which contains a single semiconductor optical amplifier (SOA), as active device, which provides both gain and modulation. The ring circuit was tested with both pseudorandom data sequences and periodic data patterns up to 10 Gb/s generating clock pulse trains across a 30 nm tuning range. The operation of the present clock recovery ring based structure relies on the fast gain saturation of the SOA, induced by the incoming data stream, that generates the modulation in the cavity and determines the injection locking of the fiber laser. The standard mode-locking SOA ring based technique has been extended introducing a Fabry-Perot cavity to select the right oscillating frequency [23]. Preliminary results, not reported here, shown that this configuration is able to works at 40 Gbit/s too. Desirable features of the CRU unit are the wide repetition frequency and wavelength locking ranges and the broad wavelength tuning range of recovered signal that it may provide.

Regarding the Re-Sampling unit (RU), a configuration based on the classical FWM non linear effect has been adopted. The incoming modulated signal, infact, is coupled with the sinusoidal-like modulated optical clock signal, recovered by the second stage, and injected into a 6 km long standard dispersion shifted fibre (DS). The net effect is a real re-sampling of the signal visible on the optical generated replica. In order to improve the performances of the non-linear effect we narrowed the optical spectrum of the clock through a cross-gain modulation effect (XGM) obtained into a semiconductor optical amplifier (SOA).

#### *A5.1.3.2 Experiments and Results*

The experiments related to the reshaping section are carried out in a 10 km long DS fiber, with loss  $\alpha=0.2$  dB/km, nonlinear coefficient  $\gamma=2.2$  [W\*km]<sup>-1</sup>, chromatic dispersion  $D=0.19$  ps/nmKm (at the pump wavelength 1542.14 nm), dispersion slope  $S_0=0.0634$  ps/nm<sup>2</sup>km and

differential group delay (PMD factor)  $DGD=0.13$  ps. This particular fibre is obtained from a single spinning fabrication process. This feature limits the fluctuation of the zero dispersion wavelength (around 1539 nm) responsible for the reduction of parametric gain and gain bandwidth and also for troubles in maintenance of a fixed phase relation between the interacting waves [24]. Moreover working close to zero dispersion area is a way to achieve a greater non-linear response using powers typical of available booster amplifiers.

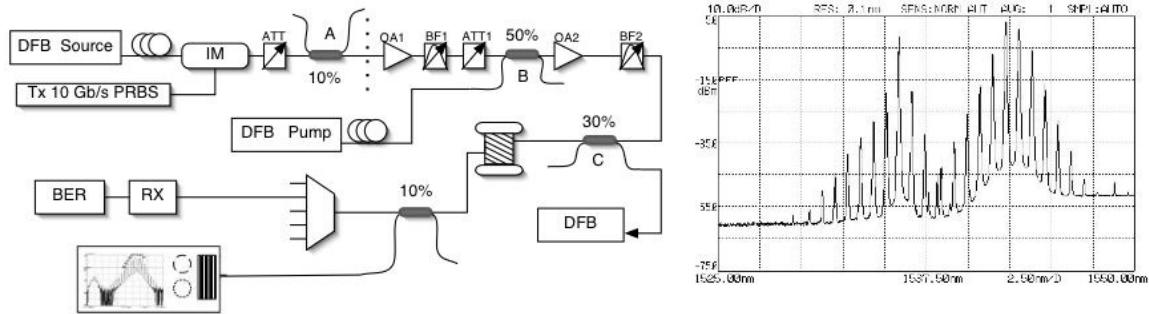


Figure 45: 2R unit set-up and optical spectrum at the DS output.

Two DFB (DFB Source and DFB pump) laser sources used to generate respectively a signal (S), at  $\lambda=1542.9$  nm, and a cw pump (CWP1), at  $\lambda=1542.1$  nm, are mixed together, in order to induce the requested non-linearity, as reported in Figure 45. In order to restrict the power depletion, due to Brillouin scattering phenomena, signal and pump are directly phase modulated. The signal, PRBS 10 Gbit/s NRZ, passes through a 10% coupler (A), preceded by an attenuator (ATT), used to measure the real optical input at the entrance of wavelength converter reshaper (WCR). After the 10% coupler there is a block made up of an EDFA (OA1) and a band pass filter (BF1) followed by an attenuator (ATT1) that allow us to set the value of signal power for optimum reshaping function. Combination of signal and pump, through 50% (B) coupler, is processed by a block made up of an erbium-doped power amplifier (OA2) and a band pass filter (BF2). This block increases the power of the pump and the signal up to the power needed in the non-linear processes.

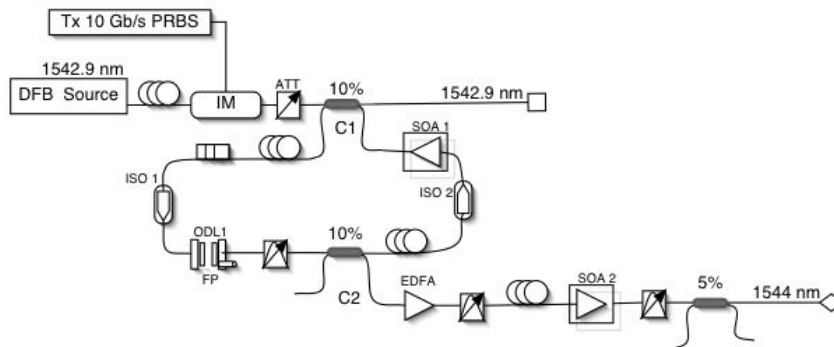


Figure 46 : Clock Recovery Unit set-up.

A third DFB (DFB) laser source is used to inject, through a 30% coupler (C), the auxiliary continuous-wave optical carrier (CW2) that, modulated along the propagation by the non-linearity, will present at the DS output a comb-like optical spectrum. The overall optical field spectrum has been reported in Figure 45.

Figure 46 shows the experimental layout related to the Timing Extraction Stage. The test data patterns were produced modulating a DFB laser source which operates at 1542.9 nm, with a

lithium niobate external modulator driven by a 10 Gbit/s PRBS pattern generator. This incoming non-return-to-zero (NRZ) data pattern, injected into the loop circuit with a 10% optical fiber coupler (C1), goes into an Alcatel M128 bulk model SOA1, with a 0.5 mm cavity length, 20 dB gain for small signal and a 40 nm amplification bandwidth, and is blocked by a first faraday isolator (ISO 1).

A second Faraday isolator (ISO2) was inserted into the ring to ensure unidirectional counter clock-wise oscillation. Starting from the ISO2, the oscillation goes into a first stage, made by a polarizer followed by a polarization controller, able to optimize the oscillating polarization state for the SOA1. This stage is followed by ISO2 and by a second block made by a Fabry-Perot cavity (FP), realised with two optical mirrors whose reflectivity is equal to 99%, and a variable optical delay line (ODL1). A subsequent 1 nm optical tunable filter is used to select the wavelength needed. The -30 dBm clock signal, extracted via a 10% coupler (C2), goes into an EDFA, a 1 nm bandwidth optical filter able to erase the ASE contribution and then is subsequently processed by an external SOA (SOA2), an Opto-Speed 1550MRI/X model with 30 dB gain for small signal and 30 nm amplification bandwidth, to obtain amplification and to simultaneously erase the amplitude noise. This particular configuration permit to obtain a sensible enhancement of the pulses train extracted.

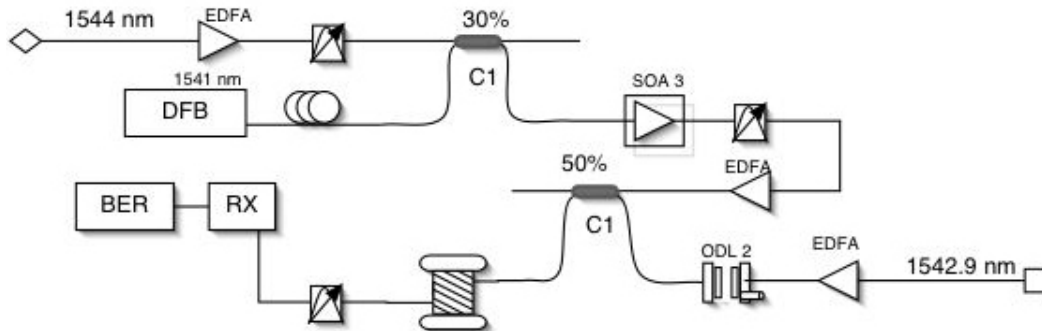


Figure 47: Re-Timing Unit set-up.

Figure 47 shows the experimental layout related to the Re-Sampling Stage. After SOA2, the recovered clock information at 1544 nm, is injected into a SOA (SOA3), an Alcatel M18 bulk model, with a CW signal through a 30% coupler. The cross gain modulation inside the SOA3 modulates the CW pump with the same information carried by the signal coming from the ring. In this manner we have a clock information with a narrower optical spectrum. At this point this signal at 1541 nm is coupled with the original 10 Gbit/s NRZ PRBS signal at 1542.9 nm, through a 50% coupler, and amplified in order to perform the retiming process inside a 6 km long DS fibre via a FWM process. An OPL2 is used to set the exact position of the data pulses in order to match it with the ones coming from the clock.

The generation of a so high number of components, at the end of 2RU, can be explained by the presence of the Kerr phase modulation process. The envelope of the beating between pump and signal, near  $\lambda_0$  (1539 nm in our case), determines a phase modulation of the whole incoming field that generates new frequencies spaced by the pump-to-signal detuning range ( $\omega_P - \omega_S$ ) [25]. The transfer function of these channels shows a non-zero threshold and a spread maximum that we can exploit for reshaper use. By adjusting the signal and pump power, at the DS fibre input, it is possible to choose the better working point in order to reshape the incoming corrupted signal, as reported in Figure 48.

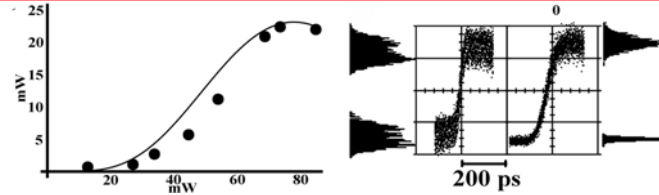


Figure 48: Comparison between experimental transfer function, dotted line, of Ch. 47 with simulation, continuous-line. Noise compression in a Non-Return-to-Zero 10 Gbit/s coded signal

The behaviour of the converted signals depends both on the SNR, due to the different generation efficiency, and to the chromatic dispersion regime seen by each channel along the device. The non-linearity at the base of the process is able to phase-modulate not only the optical beating field, that induce the non-linearity itself, but any kind of other optical carrier propagating through the fiber 1535.8 nm in this case. Subsequently, the optical spectrum of this new carrier will present a series of components each one reproducing the high data rate amplitude modulation of the original incoming signal and each one with the same Bessel-like transfer function.

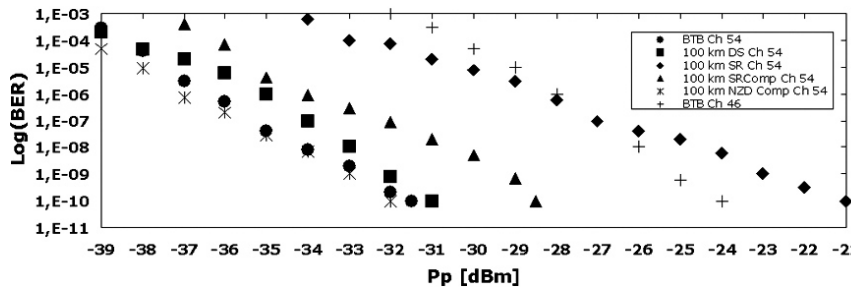


Figure 49: BTB and propagated BER measurements vs received power for ITU Ch 46 and 54.

In Figure 49 we report the BER results obtained at 10 Gbit/s, in the back to back configuration and in propagation, for the ITU-GRID channels 54 (1534.2 nm) and 46 (1540.5 nm). The propagation was performed using a cable deployed between the cities of Rome and Pomezia encompassing different kind of fibres, G.652, G.653 and G.655. The better performance on the Ch.54 depends on the better signal to noise ratio respect to the Ch. 46.

In Figure 50(a) we report the clock information at the output of the SOA2 used to obtain amplification and to simultaneously erase the amplitude noise from the ring.

Regarding the CRU unit and in the case of NRZ signals, the Fabry-Perot cavity plays a key role since it simultaneously filters out a big amount of modes, that oscillate inside the cavity, and, furthermore, by tuning the mirrors with a piezo-driver control, forces the cavity to resonate at the repetition incoming data rate. Without such resonance the locking conditions, in the case of NRZ signals, can be extremely difficult. The reasons of such behaviour stand on the large frequency band of resonance of the ring. If the FP is instead introduced in the loop and its band is tuned around the frequency of the data rate input, it will select the exact oscillating frequency giving raise to a pulse trains. The cavity fundamental frequency was 7.5 MHz and the locking bandwidth of the ring has been measured and it is equal to about 5 MHz.

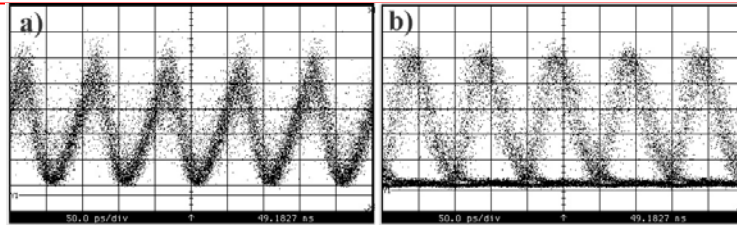


Figure 50: a) Clock recovered at the output of SOA2. b) Retiming of the incoming signal.

In Figure 50(b) we report a preliminary result concerning the converted replica at 1544.7 nm obtained at the end of the 6 km long DS fibre. The FWM is obtained by the beating of the incoming signal at 1542.9 with the clock extracted at the output of the SOA2 at 1541 nm. It is possible to see that the retiming process, due to width of the generated clock pulses, determines a format translation from NRZ to RZ format.

## 5.2 SOA-based regeneration

As already discussed previously, a key attribute of the all-optical approach is that the signals are not converted to electronics and remain in the optical domain: no broad-bandwidth electronics are necessary and only simple DC powering of the devices is required. The high-bandwidth of the all-optical technique also allows data rate independent operation, scaling easily from 2.5Gb/s to >40Gb/s operation with the same device.

The basic technique of all-optical regeneration is to use nonlinear optical materials to allow one light beam to affect another without using electronics [26]. Another very promising technique that can be applied for high-speed data signals at 10, 40 Gb/s and beyond uses nonlinear semiconductor optical amplifiers (SOAs) as the core of optical regeneration devices based on interferometric optical switching gates [27]. SOAs based on indium phosphide (InP) optoelectronic semiconductor materials [28] are practical devices because they provide optical gain (unsaturated gain >30dB at 1550nm wavelength), are compact (<2mm size), require very low optical switching energies (<100fJ), are polarization insensitive (<0.5dB) and can be incorporated in low-loss integrated optical structures [29].

### 5.2.1 SOA-based all-optical regeneration principle

The basic principle of how an SOA based all-optical regenerator operates is shown in Figure 51. This is shown for a Mach-Zehnder interferometer (MZI) structure that incorporates an SOA in each arm of the MZI. The MZI has two inputs: the degraded data and a cw beam at a different wavelength.

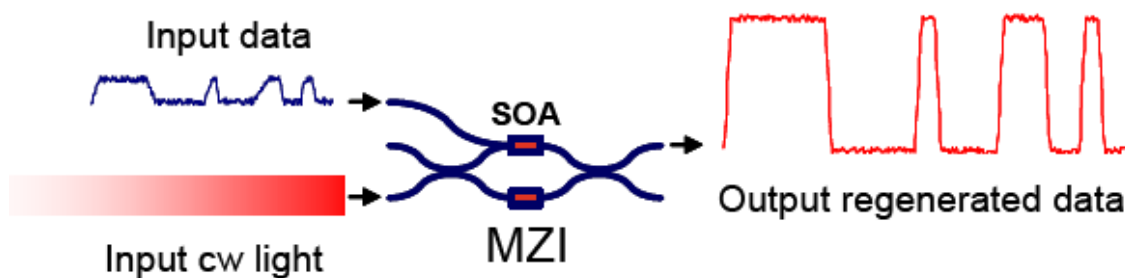


Figure 51. Schematic diagram of the operation of a MZI-based 2R regenerator.

Incoming optical data signals are configured to cause a gain reduction in one of the SOAs. This gain reduction produces an accompanying refractive index change that results in a phase change for the local cw light beam travelling through that SOA (the upper arm in Figure 51). This light beam on the upper arm of the MZI then optically interferes with the non-phase-shifted beam from the lower arm at the MZI output coupler. The induced phase difference causes the output light to be redirected from one output port to the other. As shown in Figure 52, if the phase difference is  $\pi$  radians, then all of the light appears out of the upper MZI output and no light appears from the lower MZI output. Since the shape of the phase dependent output (Figure 52) is nonlinear and has an S-shape, this effect reshapes the distribution of any amplitude noise at the input of the regenerator. The regeneration occurs by effectively ‘squeezing’ the noise so that the output optical signal to noise ratio (OSNR) can be dramatically improved.

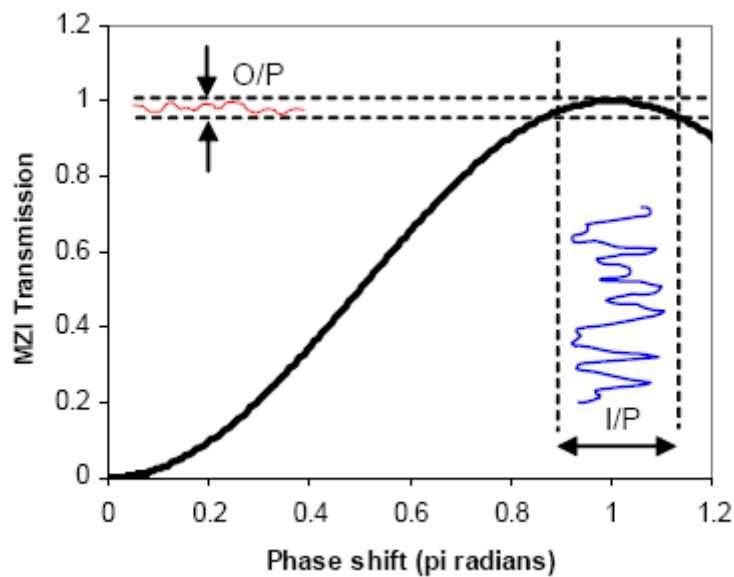


Figure 52. Relative transmission of the MZI upper output port as a function of the induced phase shift in the SOA (black line). The insets schematically show how input (I/P) amplitude noise is ‘squeezed’ on the MZI output (O/P) port when the induced phase shift is close to  $\pi$  radians.

The dynamics of this process are very important for high-speed operation and are greatly affected by the type of SOA. In particular, the SOA has an optical gain recovery time that determines how fast the incoming data signals can be and still achieve good regeneration. Recent device improvements in SOA design for fast recovery times (typically  $1/e \sim 16$ ps) [28] and techniques such as ‘push-pull’ operation [30] allow the MZI type of all-optical regenerator to be extremely effective for 40Gb/s data signals. Figure 53(a) shows a schematic diagram of how this differential switching architecture operates. The input data is split and injected into two inputs of the MZI. With correct relative time delay ( $\Delta t$ ) and powers, cancellation of the slow gain recovery component is possible, as shown in Figure 53(b).

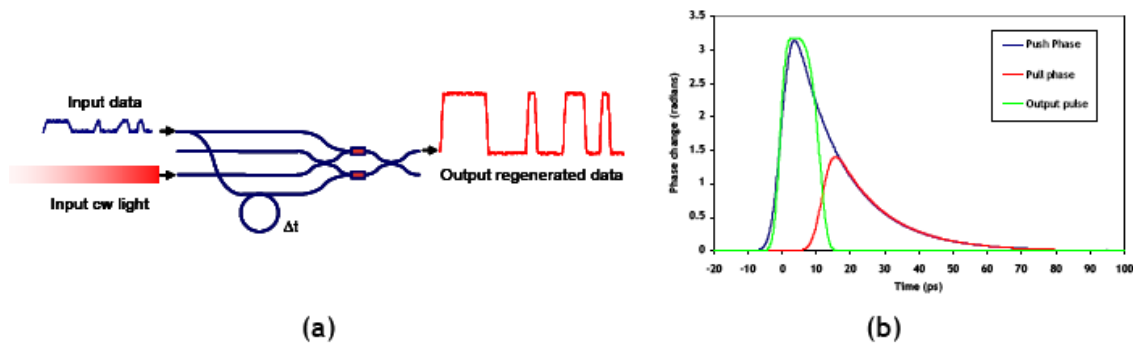


Figure 53. (a) Schematic diagram of 'push-pull' MZI operation. (b) The slow recovery of the 'push' phase is cancelled by the 'pull' phase change, creating a high-bandwidth switching window.

### 5.2.2 Integrated SOA-MZIs 2R regenerators

The evolution from bulk-component SOA regenerators to complex integrated structures was made possible by exploiting a unified integration platform based on hybrid technology [31]. This photonic integration platform is a pragmatic combination of the best available optical technologies for active and passive optical devices. The platform is uniquely designed for passive assembly of the different components in order to maintain high optical performance and low insertion losses, but at much lower cost. In a similar method to the electronic printed circuit board used in electronics, a planar silica on silicon waveguide acts as a motherboard to host both active and passive devices. Integration is achieved by plugging precision-machined silicon submounts or "daughterboards" carrying individual optical components into the motherboard. The individual components have precision cleaved features for accurate mechanical positioning on the daughterboard. In the case of the development of single-element SOA-MZI optical gates, the daughterboards are designed to host monolithic twin SOA chips and provide all suitable alignment stops. These SOAs are specially designed to have high gain and maximized nonlinearity by incorporating optical mode expanders. Figure 54 shows photographs of photonic integrated prototype devices along with the corresponding motherboard schematic designs. The fully packaged and pigtailed SOA-MZI optical gate is shown in Figure 54(a), along with the motherboard design, as shown in Figure 54(b). The fibre pigtailling is also achieved with a passive assembly approach using arrays of optical fibres in precision V-grooves on a silicon carrier. The daughterboard depicted in Figure 54(c) consists of a twin SOA array and is flip-chipped onto the motherboard [32].

As device cost is predominantly defined by packaging and pig-tailing, the easiest way to reduce it is by the integration of multi-element arrays of devices on a single chip and package. Multi-element switch arrays will also help to reduce the footprint of active elements in an all-optical processing card so that cost reduction, device availability and ease of use are likely to make switch arrays an enabler of all-optical techniques. Figure 54(d) shows the photograph of a quadruple array of optical gates integrated using hybrid integration technology. The corresponding motherboard design is shown in Figure 54(e) with two daughterboards clearly marked. In this case, each daughterboard hosts a quad array of SOAs (Figure 54(f)), forming two SOA-MZI optical gates.

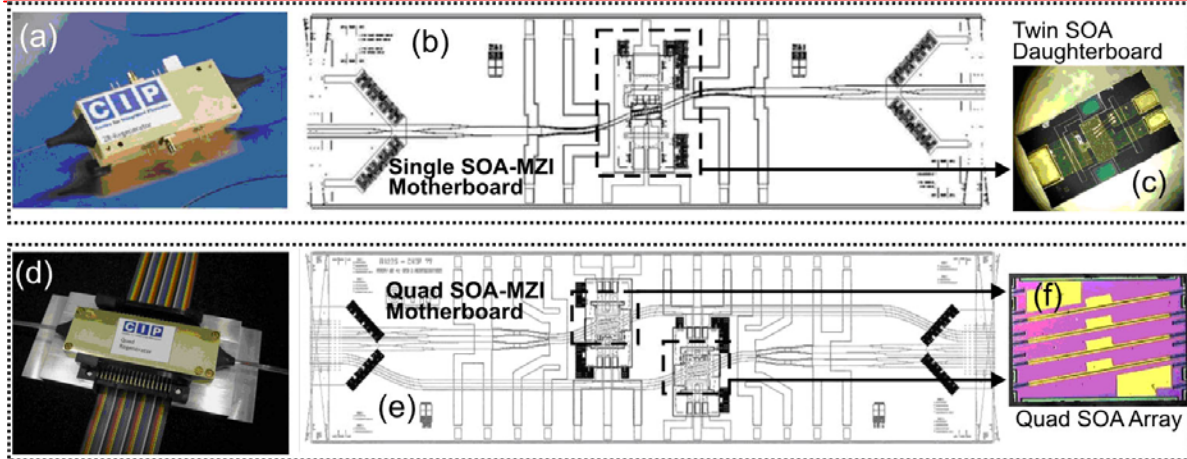


Figure 54: (a) Packaged and pigtailed SOA-MZI optical gate, (b) corresponding motherboard design and (c) twin SOA silicon submounts, (d) packaged and pigtailed prototype device containing four SOA-MZI optical gates on a single photonic chip, (e) corresponding motherboard design and (f) quad array of SOAs used for constructing each double SOA-MZI gate within the chip.

#### A5.2.2.1 Mobility action on detailed investigation of the regenerative properties of 2R SOA-MZI all-optical regenerators

The in-depth investigation of the variants of SOA-MZI based 2R regenerators will be carried out by NTUA in collaboration with UoA in regards of their regenerative properties, namely the BER performance, the sensitivity in timing jitter, the cascability performance etc. The joint activity has already started aiming at a complete theoretical, numerical and experimental evaluation of the devices. The theoretical analysis aims at BER estimation utilizing power transfer and jitter characteristics of the specific 2R regenerators. The memory effect in combination with the degree of the transfer characteristics nonlinearity effect on the jitter accumulation will be explicitly studied. Filter effects are also an important issue for detailed investigation.

The numerical analysis includes full NLSE simulation for the transmission of the high bitrate signal and full numerical simulation of the SOA-MZI regenerators. The cascability performance of the different variants of the 2R regenerator will be investigated in terms of the bit-rate, power of the transmitted signal, transfer function of the regenerator, jitter effects and dispersion management maps.

The aforementioned analysis will be supported by experimental measurements.

#### A5.2.2.2 Current Status of the joint action – Timeplan – Expected outcome

The mobility action is currently running and will be completed before 31<sup>st</sup> of December. Currently the different variants of the 2R regenerators based on SOA-MZI modules are theoretically investigated working on the development of a full model taking into account the basic phenomena taking place inside semiconductor optical amplifiers. Moreover, a theoretical model for the estimation of the BER based on the power transfer characteristics of the regenerator is in preparation. For the next period, and after the models' optimization, theoretical and numerical analysis will be carried out in order to decide on the proper operating regimes for the uppermost performance of the specific devices serving as in line regenerators in a transmission system. The next step is to carry out experiments in order to

verify the analytically and numerically derived results. The expected outcome of this activity is the preparation of at least one long paper including the results of the activity.

### 5.2.3 GC-SOA format converter regenerator

In a gain clamped SOA (GC-SOA), constant optical gain is obtained over a broad input power range by means of an internal laser. GC-SOA are attractive devices for all-optical signal processing due to several characteristics. Due to the presence of an internal laser, faster response is expected [33]; the non-linear interactions occurring between the input signal, the free carriers and the internal laser have been exploited for wavelength conversion, reshaping and format conversion [34,35]; the gain independence on the injection current is explored to obtain a regenerator with a true regeneration characteristic [36]. The linear gain curve has been exploited for all-optical WDM switching. In this work we present a review of our work regarding non-linear applications of GC-SOA for all-optical signal processing; these include format and wavelength conversion, regeneration, and signal reshaping.

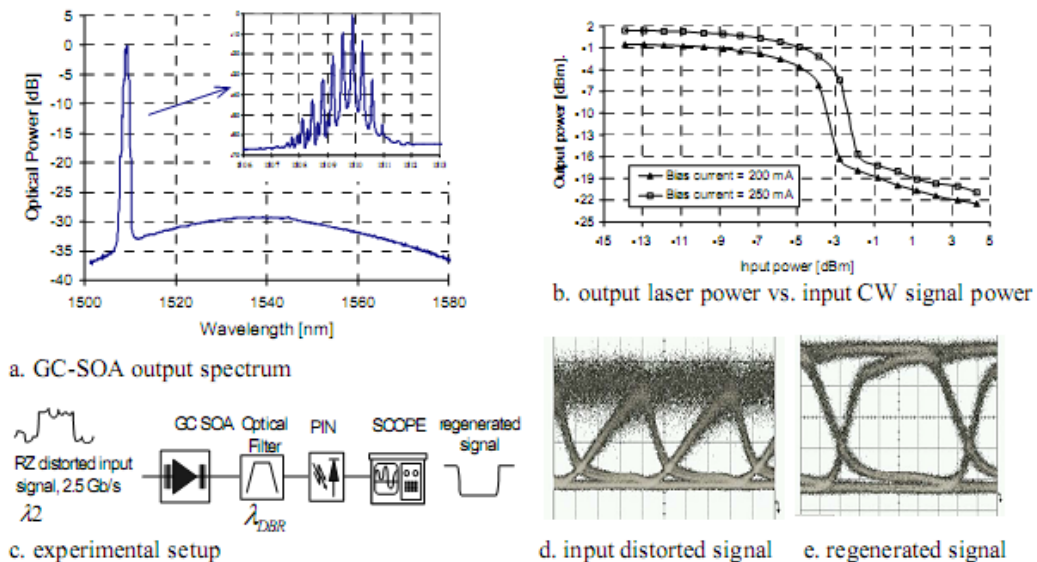


Figure 55: 2R regeneration with GC-SOA.

The GC-SOA internal laser power varies inversely to the input signal power, maintaining constant optical gain. In Figure 55(a) and Figure 55(b) the GC-SOA output optical spectrum and output power are depicted as a function of the input power. When the input signal power is in the low level, small variations are observed in the generated laser power; around the threshold power (about -2.5 dBm, for a current of 200 mA) the power of the laser drops considerably (for a variation of 2 dB in the input, the output power decreases 12 dB). For high powers of the input signal a laser power variation is verified (of about 0.6 dB per dB in the input); however, most of this power is amplified spontaneous emission (ASE) noise, since a very broadband filter was utilized. This regenerator experimental setup at 2.5 Gb/s is very simple and compact. The distorted input signal is completely regenerated and the output extinction ratio (ER) is also enhanced (11 dB, for input ER of 7.5 dB). The laser relaxation oscillations are not visible in Figure 55(e), since a photodiode with 4 GHz of bandwidth was utilized (the oscillations are around 10 GHz).

In [34] we have proposed a simple, non-inverting format converter from RZ to Non-RZ (NRZ) with eventual wavelength conversion capabilities. The operation principle is illustrated in Figure 56(a) [35], where the temporal evolutions of the GC-SOA carrier density and internal laser power are represented when two consecutive optical pulses are injected, considering a pulse spacing (TP) close to the maximum modulation rate of the GC-SOA internal laser. In the “high power” mode the internal laser is NRZ modulated with the inverted equivalent of the input logical information. This laser is generated inside the GC-SOA but is available at its output, due to the limited reflectivity of the GC-SOA facets and gratings; therefore RZ to NRZ format conversion is obtained at the GC-SOA output at the internal laser wavelength. To improve the output NRZ signal characteristics and allow eventual tunable wavelength conversion, a XGM stage in a common SOA is cascaded. Pulse width independent operation was experimentally reported at 10 Gb/s, with undistorted output signal. Conversion at higher bit rates is expected if a GC-SOA with a DBR laser with higher modulation speed is designed [36].

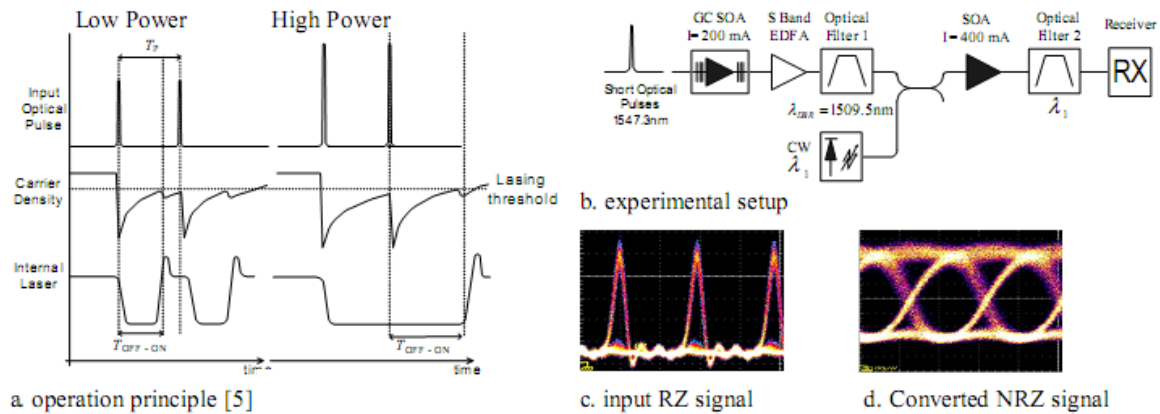


Figure 56: RZ to NRZ format conversion.

As a conclusion, Gain clamping can be used to achieve several sets of functionalities expanding the possibilities of SOA operation window. Regeneration, wavelength conversion without recurring to external lasing and format conversion are only some of the prominent possibilities of these devices.

### 5.3 Analysis of Long-haul Transmission System with Phase-Sensitive Amplifiers: BER performance estimation

The impact of phase-sensitive amplification on the BER performance of a phase-modulated link is semi-analytically estimated revealing its effectiveness in handling nonlinear phase noise.

#### 5.3.1 Introduction

In contemporary optical communications research, Phase-Shift Keying (PSK) modulation formats have emerged as one of the most prevalent solution for future long-haul optical transmission systems. The accumulation of linear and nonlinear phase noise through consecutive fiber spans, degrades the Bit Error Rate (BER) of this type of modulation formats and therefore limits the maximum transmission distance [37]. Phase-Sensitive Amplifiers

(PSAs), based on either interferometric or non-interferometric schemes [38,39] seem the most appropriate means for simultaneous amplitude and phase noise mitigation.

To evaluate the performance of a phase modulated link using a PSA, one must accurately evaluate the statistical properties of the residual phase and amplitude noise at the output of the PSA. The performance of interferometric PSAs and phase noise averaging regenerators was recently presented by Wei et. al. [40], considering however a Gaussian noise source disturbing the signal. In our work, a more detailed analysis is carried out based on the phase and amplitude input-output characteristics of a PSA based on Four Wave Mixing (FWM).

### 5.3.2 Theory

The PSA considered in this work is based on degenerate four-wave mixing in fibers. The phase-sensitivity is achieved by placing the pumps at frequencies that provide a non-frequency shifted image of the signal. The frequency pumps condition for phase-sensitive interaction is  $\omega_{p1} + \omega_{p2} = 2\omega_s$ . The accurate expressions giving the dependence of the output on input signal can be found in [39]. In Figure 57 a transmission system utilizing one such PSA is depicted.

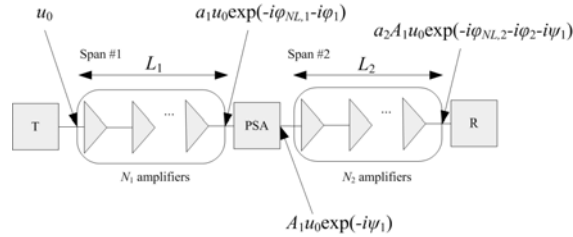


Figure 57: A transmission system with two fiber segments and a PSA placed between these two segments

Our aim is to calculate the BER at the receiver side and identify the impact of PSA on the overall BER performance.

The noise statistics along the first segment (Figure 57) are described by the joint probability density function (PDF) of phase  $\phi$  and normalized amplitude  $\alpha$  in an optical communication system [41].

$$P(\alpha_1, \phi_1) = \sum_{n=-\infty}^{\infty} \frac{\alpha_1}{\pi P_{ASE,1} T_{n,1} C_{n,1}} \exp\left(-\frac{C_{n,1}^2 \alpha_1^2 + 1}{P_{ASE,1} T_{n,1} C_{n,1}^2}\right) \times I_n\left(\frac{2\alpha_1}{P_{ASE,1} T_{n,1} C_{n,1}}\right) \times \exp\{-in[\phi_1 + \phi_{NL,1}(1 - T_{n,1})]\} \quad (6)$$

where  $P_{ASE,1}$  is the inverse of the optical signal-to-noise ratio,  $\phi_{NL,1}$  is the nonlinear phase shift,  $I_n$  is the  $n^{\text{th}}$  order of the Bessel function, and  $C_{n,1}$ ,  $T_{n,1}$  functions of  $n$ ,  $P_{ASE,1}$ ,  $\phi_{NL,1}$  [41]. Assuming that the PSA is working in the linear regime, the new joint PDF  $P_{PSA}(A_1, \psi_1)$  ( $A_1$ ,  $\psi_1$  the normalized amplitude and the phase at the output of the amplifier respectively) that corresponds to the statistics of a signal at the output of the amplifier can be straightforwardly calculated [42] applying the theorem of transformation of random variables:



$$P_{PSA}(A_1, \psi_1) = P(a_1, \varphi_1) \begin{vmatrix} \frac{\partial a_1}{\partial A_1} & \frac{\partial a_1}{\partial \psi_1} \\ \frac{\partial \varphi_1}{\partial A_1} & \frac{\partial \varphi_1}{\partial \psi_1} \end{vmatrix} \quad (7)$$

As the signal propagates inside the second span, it acquires an additional amplitude and phase noise  $a_2$  and  $\varphi_2$  respectively. The total amplitude and phase noises are therefore  $A=a_2A_1$  and  $\varphi=\varphi_1+\varphi_{NL,2}+\varphi_2$  where phase  $\varphi_{NL,2}$  is the nonlinear shift induced by the input amplitude at the second span. To calculate the joint PDF  $P_{out}(A,\varphi)$  of  $A$  and  $\varphi$ , one starts from the joint conditional PDF  $P_2(a_2,\varphi_2|A_1,\psi_1)$  of  $a_2$  and  $\varphi_2$  given the values of  $A_1$  and  $\psi_1$ . This PDF is quite similar to equation (6), the only difference being that the incident amplitude is now  $A_1|u_0|$  instead of  $|u_0|$  and that the parameters of the second span must be used:

$$P_2(a_2, \varphi_2 | A_1, \psi_1) = \sum_{n=-\infty}^{\infty} \frac{a_2}{\pi P_{ASE,2} T_{n,2} C_{n,2}} \exp\left(-\frac{C_{n,2}^2 a_2^2 + 1}{P_{ASE,2} T_{n,2} C_{n,2}^2}\right) \times I_n\left(\frac{2a_2}{P_{ASE,2} T_{n,2} C_{n,2}}\right) \times \exp\{-in[\varphi_2 + \varphi_{NL,2}(1 - T_{n,2})]\} \quad (8)$$

In (8)  $P_{ASE,2}=N_2 n_{sp} h f (G-1) B / |A_1 u_0|^2$  and the terms,  $T_{n,2}$ ,  $C_{n,2}$  are calculated according to the expressions given previously using  $P_{ASE,2}$  and  $\varphi_{NL,2}$  instead of  $P_{ASE,1}$  and  $\varphi_{NL,1}$ . Given the fact that  $a_2=A/A_1$  and  $\varphi_2=\varphi-\varphi_1-\varphi_{NL,2}$ , the unconditional joint PDF of  $A$  and  $\varphi$  at the output of the second transmission link can be as below:

$$P_{out}(A, \varphi) = \iint_{A_1, \psi_1} dA_1 d\psi_1 P_2\left(\frac{A}{A_1}, \varphi - \varphi_1 - \varphi_{NL,2} \middle| A_1, \psi_1\right) P_{PSA}(A_1, \psi_1) \quad (9)$$

Once  $P_{out}(A, \varphi)$  is evaluated, one may estimate the PDF  $P_{out}(\varphi)$  using numerical integration and the BER can be calculated by numerically integrating  $P_{out}(\varphi)$  in the interval  $[\langle\varphi\rangle + \pi/2, \langle\varphi\rangle + 3\pi/2]$  for the case of a PSK system where  $\langle\varphi\rangle$  is the average value of  $\varphi$ .

### 5.3.3 Semi-analytical results

Utilizing the above analysis, the performance for a typical PSK system is studied with and without the inclusion of a PSA regenerative module. For our numerical simulations we have considered the fiber parameters of [39] and [42]. In the calculations that follow, the transmission span consists of 5000km of single-mode fiber with attenuation coefficient  $\alpha_T=0.2$ dB/km. Dispersion effects are neglected. Optical amplifiers are placed every 50km having  $n_{sp}=1.5$ , each coupled to an ideal optical bandpass filter with bandwidth equal to 200GHz, which is broad enough to accommodate 40Gb/s phase modulated signals. Our calculations reveal that a small BER improvement is observed at the PSA output, a behavior already noticed in [42]. However, the question is if the PSA is capable to prevent phase noise accumulation along the second segment. The actual position of the PSA may greatly influence the BER performance at the receiver, depending on the transmitted signal's power. One should avoid positioning PSA right before the receiver, since the BER is only marginally improved in this case. One should also exclude positions at lengths shorter than the mid point of the link, as the PSA would not restrain the amplitude noise of the input signal since it operates in the linear regime. It would therefore seem that the PSA should be placed closer to the receiver but not on the receiver itself.

These intuitive assumptions are verified by calculations presented in Figure 58(a). The two horizontal black lines correspond to the BER performance of the conventional link (no PSA

involved) for transmitted signal power equal to 1mW and 0.5mW respectively and are included in the figure as performance reference. The solid line with dots (triangles) shows the BER at 5000km for 0.5mW (1mW). The pump power of PSA is 0.3W. It is observed that the BER performance at the receiver depends on the PSA position for the 1mW signal. The lower BER value is obtained for a PSA located 3400km away from the transmitter. For 0.5mW, the exact position of PSA is not that critical, as the effect of nonlinear phase noise is less catastrophic in this case. The regenerative properties of the PSA are also investigated in terms of the signal transmitted power in Figure 58(b). The PSA is placed at 3500km. The BER performance before and after the PSA is not substantially different; at the receiver side however, the BER is much lower when a PSA is used achieving almost a five orders of magnitude improvement for 1mW (red line with dots) compared to the uncompensated link (blue line with white triangles). This is another indication of the significant suppression of the nonlinear phase noise component inside the PSA.

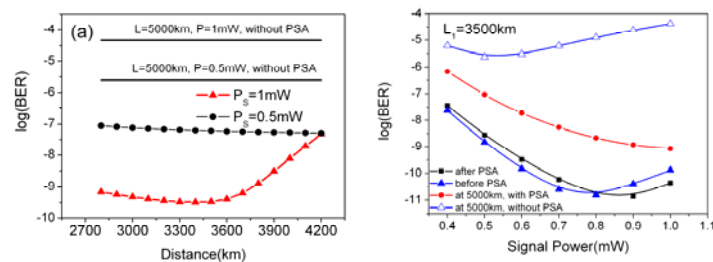


Figure 58. (a) BER at the receiver as a function of the PSA position. (b) BER as a function of signal power.

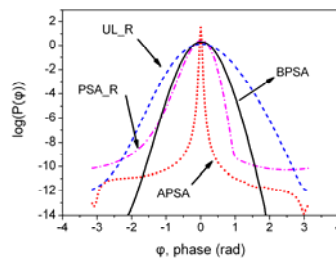


Figure 59. PDF of phase noise at different link locations: before PSA at 3500km (BPSA), right after PSA (APSA), and at the receiver (PSA\_R). The phase PDF for the uncompensated link at the receiver (UL\_R) is also plotted.

The regenerative properties of the PSA are better illustrated in Figure 59, where the phase noise PDF of the phase noise for a 1mW transmitted PSK signal is depicted in different locations, namely before the PSA (BPSA), after the PSA (APSA), and at the receiver side (PSA\_R). The PDF of for the uncompensated link (UL\_R) is also included for comparison. The PDFs are related to the BER performance depicted in Figure 58 for signal power equal to 1mW. The PDF of the phase noise at the receiver is significantly affected by the PSA presence in the link. It is evident that phase occurrence in  $[-\pi, -\pi/2]$  and  $[\pi/2, \pi]$  is less frequent when a PSA is incorporated compared to the uncompensated link. This implies that the transformation of the phase statistics prevents the rapid phase noise build-up taking place across the later stages of the long-haul transmission.



### 5.3.4 Conclusions

In summary, the statistics of phase noise along a long-haul transmission link utilizing phase-sensitive amplification were semi-analytically calculated. The PSA can provide significant BER improvement as long as nonlinear phase noise is the dominant noise source provided that it is placed closer to the receiver. Through WP-15 it is expected to develop further this activity carrying out comparative studies between phase-sensitive schemes and phase-preserving schemes that restrain the amplitude noise of phase-modulated systems. Moreover, a more detailed study taking into account PSA detrimental effects such as pump noise and Raman effect will be the subject of a future activity.

## 5.4 References

- 1 D. M. Forin, F. Curti, G. M. Tosi Beleffi and F. Matera "All Optical Fibre 2+1 Auxiliary Carrier Transponder-Regenerator" IEEE-Photonics Technology Letters, Vol. 17, Issue 2, (2005), pp. 429-431.
- 2 S. Watanabe, F. Futami, R. Okabe, Y. Takita, S. Ferber, R. Ludwig, C. Schubert, C. Schmidt-Langhorst and H. G. Weber, "160 Gb/s Optical 3R Regenerator in Fiber Transmission experiment," OFC 2003, PD16-1.
- 3 T. Ohara, H. Takara, S. Kawanishi, T. Yamada, and M. M. Fejer, "160-Gb/s all-optical limiter based on spectrally filtered optical solitons," IEEE Photon. Technol. Lett., vol. 16, pp. 2311-2313, 2004.
- 4 T. L. Lakoba, and M. Vasilyev, "A new robust regime for a dispersion managed multichannel 2R regenerator," Opt. Express 15, pp. 10061-10074, 2007.
- 5 P. Vorreau, C. Kouloumentas, L. Provost, I. Tomkos, W. Freude, J. Leuthold, "Simultaneous Processing of 43 Gb/s WDM Channels by a Fiber-Based Dispersion-Managed 2R Regenerator", ECOC 2008, Brussels, Belgium, Th.1.B.3.
- 6 D. V. Kuksenkov, S. Li, M. Sauer, and D. A. Nolan, "Nonlinear Fibre Devices Operating on Multiple WDM Channels," ECOC 2005, Glasgow, UK, Mo.3.5.1.
- 7 L. Provost, F. Parmigiani, P. Petropoulos, and D. J. Richardson, "Simultaneous 2R all-optical regeneration of two 40 Gbit/s channels", IEEE Photon. Technol. Lett., vol. 20, pp. 270-273, 2008.
- 8 P.V. Mamyshev, "All-Optical Data Regeneration based-on Self Phase Modulation Effect", ECOC98, September 1998, Spain
- 9 L. Provost, C. Finot, P. Petropoulos, K. Mukasa, D. J. Richardson, "Design scaling rules for 2R-optical self phase modulation-based regenerators", Optics Express Vol.15 pp.5100-5111, 2007.
- 10 M. Karlsson, "Four-Wave mixing in fiber with randomly varying zero-dispersion wavelength", Journal of the Optical Society of America B, Vol. 15, (1998), pp 2269-2275.
- 11 R. Thompson, R. Roy, "Nonlinear dynamics of multiple four-wave mixing processes in a single-mode fiber", Physics Review A, 43, (1991), pp. 4987-4996.
- 12 E. Ciaramella, F. Curti and S. Trillo, "All-optical signal reshaping by means of Four-Wave mixing in optical fibers", IEEE-Photonics Technology Letters, Vol. 13, (2001), pp. 142-144.
- 13 G.M. Tosi-Beleffi, F. Curti, D.M. Forin, F. Matera, "10 Gbit/s All-Optical 2R Fiber Based Regeneration" Optics Communications, 236/4-6, 323-327 (2004)
- 14 D. M. Forin, F. Curti, G. M. Tosi Beleffi et al "All Optical 2R Regenerator Based on Induced Phase Modulation on an Auxiliary Carrier" CLEO/QUELS 2005.
- 15 G. Incerti, A Teixeira, G.M. Tosi Beleffi, F. Curti, M. Guglielmucci: All Optical Multichannel Regeneration Systems Based on Non Linear Effects, ICTON07 Proceedings, Rome 1-5 July (Italy).
- 16 D. M. Forin, F. Curti, G. M. Tosi Beleffi and F. Matera "All Optical Fibre 2+1 Auxiliary Carrier Transponder-Regenerator" Photonics Technology Letters, Vol. 17, Issue 2, (2005), pp. 429-431
- 17 M. Nielsen, and J. Mork, "Recent Advancements in Semiconductor-based Optical Signal Processing", in ECOC 2006, Cannes, Sept. 2006, We2.4.1.
- 18 S. Boscolo, S. K. Turitsyn, V. K. Mezentsev, "Performance Comparison of 2R and 3R Optical Regeneration Schemes at 40 Gb/s for Application to All-Optical Networks", JLT, vol. 23 n. 1, January 2005
- 19 B. Cuenot, A. Ellis, N. Healy, D. F. Murphy, C. D. Hussey, "Optical Regeneration of WDM Signals Using Quasi-Continuous Filtering", ICTON 2006, Th.B1.1, pp.267-270.
- 20 L. Provost, F. Parmigiani, P. Petropoulos, D. J. Richardson, "Investigation of Simultaneous 2R Regeneration of Two 40-Gb/s Channels in a Single Optical Fiber", IEEE PTL, vol. 20, no. 4, February, 2008
- 21 L. Provost, et al, "Experimental Investigation of a Dispersion-Managed Multi-channel 2R Optical Regenerator", OFC/NFOEC 2008, OThJ3.



- 22 G. M. Tosi Beleffi, D. M. Forin, F. Curti, F. Matera, A. Reale, S. Betti, S. Monterosso, A. Fiorelli, M. Guglielmucci, "3R All Optical Regeneration", ICTON04 Proceedings, July Warsaw (Poland).
- 23 J.P. Turkiewicz, E. Tangdiongga, All Optical 10 Ghz Clock Recovery from 160 Gbit/s OTDM signals using a mode-locked fibre ring laser, IEEE/LEOS Benelux Chapter 2002, Amsterdam .
- 24 M. Karlsson, Four-wave mixing in fiber with randomly varying zero-dispersion wavelength, J. Opt. Soc. Am. B, vol. 15, pp. 2269-2275, 1998.
- 25 J.R. Thompson, R. Roy, "Nonlinear dynamics of multiple four-wave mixing processes in a single-mode fiber", Physical Review A, vol. 43, No. 9, pp. 4987-4996, 1991.
- 26 D. Cotter, R. J. Manning, K. J. Blow, A. D. Ellis, A. E. Kelly, D. Nasset, I. D. Phillips, A. J. Poustie, D. C. Rogers, "Nonlinear Optics for High-Speed Digital Information Processing", Science, 286, p.1433 (1999).
- 27 A. Poustie, "Semiconductor Devices for All-optical Signal Processing", ECOC 2005, paper We3.5.1, Glasgow (2005).
- 28 <http://www.wordsun.com/cip2.html>
- 29 G. Maxwell, A. Poustie, C. Ford, M. Harlow, P. Townley, M. Nield, I. Lealman, S. Oliver, L. Rivers, R. Waller, "Hybrid Integration of Monolithic Semiconductor Optical Amplifier Arrays Using Passive Assembly", 55th Electronics and Technology Conference (ECTC), Lake Buena Vista, (2005).
- 30 K. Tajima, "All-optical Switch with Switch-off Time Unrestricted by Carrier Lifetime", Jpn. J. Appl. Phys., 32, L1746 (1993).
- 31 G. Maxwell et al., "Very low coupling loss, hybrid-integrated all-optical regenerator with passive assembly", in Proc. European Conference on Optical Communication 2002, paper PD3.5.
- 32 <http://www.ciphotonics.com>
- 33 J. Manning, et al.: Enhanced recovery rates in semiconductor laser amplifiers using optical pumping, Electron. Lett., vol. 30, no. 10, pp. 787-788, May 1994.
- 34 T. Silveira, et al.: All-Optical Conversion from RZ to NRZ Using Gain Clamped SOA, IEEE Photon. Technol. Lett., vol. 19, no. 6, pp. 357-359, March 2007.
- 35 T. Silveira, et al.: All -Optical Wavelength Conversion and reshape based on a single Gain Clamped SOA, in CLEO 2006, Long Beach, May 2006.
- 36 G. Morthier, et al.: Experimental demonstration of an all-optical 2R regenerator with adjustable decision threshold and "true" regeneration characteristics, IEEE Photon. Technol. Lett., vol. 12, no. 11, pp. 1516-1518, Nov. 2000.
- 37 C. Xu, et. al, "Differential phase-shift keying for high spectral efficiency optical transmissions," IEEE JSTQE. 10, 281-293, (2004).
- 38 K. Coussore, et. al., "Phase-and-amplitude regeneration of differential phase-shift keyed signals using a phase sensitive amplifier," Opt. Express, 14, 2085-2094, (2006).
- 39 A. Bogris, et. al. "RZ-DPSK Signal Regeneration Based on Dual-Pump Phase-Sensitive Amplification in Fibers," IEEE PTL. 18, 2144-2147 (2006).
- 40 C. C. Wei, et. al., "Evaluating the performance improvement of differential phase-shift keying signals by amplitude regeneration and phase-noise suppression," Opt. Lett., 20, 1090-1092, (2008)
- 41 A. Mecozzi, "Probability density functions of the nonlinear phase noise," Opt. Lett., 29, pp. 673-675, (2004).
- 42 A. Bogris, et. al., " Transformation of nonlinear phase noise statistics in a phase-sensitive amplifier," in IEEE/LEOS WTM2008, MB1.4, (2008).



## 6. Amplification in Transmission (IT, ISCOM, UPC)

### 6.1 Extension of Black Box Model of EDFAs to include variation of the EDF's Length

#### 6.1.1 Introduction

Fiber optical Amplifiers (EDFAs) were key technology for the 4th generation of Optical Communication Systems [1]. Recently, also Passive Optical access Networks (PON) are introducing EDFAs and remotely pumped EDFs for: enhancing the maximum number of users and distances [2] and providing resilience, high capacity and scalability in fully passive optical networks [3].

The gain and noise figure of the EDFAs can be described by a set of propagation and rate equations [4]. Nevertheless, the main drawbacks of this method are: a) the difficulty to obtain certain fiber parameters, such as the erbium concentration and distribution in the fiber, cross sections, etc; b) the high time consumption to numerically solve each specific case of the pump power and signal inputs, even after considerable computation time reduction using approximate solutions based on overlapping factors [5].

Alternatively, black box models (BBM) have been proposed as a simplified model, based on experimental data obtained by simple test measurements, without knowing internal details of the amplifier [6, 7, 8]. In this section, we present an explicit extended BBM, including EDF length variations, as a powerful tool for EDFA's design and remote EDF amplification in the next generation networks [2, 3].

#### 6.1.2 Theoretical Modelling

The black-box models of EDFA presented in the literature [6, 7, 8] apply to optical amplifiers which can be modelled as a quasi-two level system with single photon transitions. They are based on the assumption of homogeneous saturation of the amplifier which means that the spectral gain is entirely determined by the average distribution of the population inversion [8]. This means that the same saturation condition and same spectral gain can be achieved with many different combinations of pump power and signal power.

Following the BBM proposed in [7], the gain characteristic  $G^{dB}(\lambda)$  of the amplifier, expressed in dBs, can be described as:

$$G^{dB}(\lambda) = T(\lambda, \lambda_{ref}) \cdot [G^{dB}(\lambda_{ref}) - G_{ref}^{dB}(\lambda_{ref})] + G_{ref}^{dB}(\lambda) \quad (1)$$

where  $\lambda_{ref}$  is a reference wavelength and,  $G_{ref}^{dB}(\lambda_{ref})$  and  $G_{ref}^{dB}(\lambda)$  are, respectively, a reference signal gain at  $\lambda_{ref}$  and a signal gain spectrum, at reference signal and pump input powers. Finally,  $T(\lambda, \lambda_{ref})$  is the named Tilt function that can be experimentally measured from two gain spectrums measured at different saturation conditions,  $G_{1}^{dB}(\lambda)$  and  $G_{2}^{dB}(\lambda)$ , without any knowledge about internal detail of the amplifier [7]:

$$T(\lambda, \lambda_{ref}) = \frac{G_1^{dB}(\lambda) - G_2^{dB}(\lambda)}{G_1^{dB}(\lambda_{ref}) - G_2^{dB}(\lambda_{ref})} = \frac{\alpha(\lambda) + \gamma(\lambda)}{\alpha(\lambda_{ref}) + \gamma(\lambda_{ref})} \quad (2)$$

where  $\alpha(\lambda)$  and  $\gamma(\lambda)$  are, correspondingly, the absorption and emission coefficients. They are related to the corresponding cross sections  $\sigma_a(\lambda)$  and  $\sigma_e(\lambda)$  by the expressions:  $\alpha(\lambda) = \sigma_a(\lambda)N_{Er}$  and  $\gamma(\lambda) = \sigma_e(\lambda)N_{Er}$ , [9] where  $N_{Er} = \int d\mathbf{r}_t n_{Er}(\mathbf{r}_t) |\Psi(\mathbf{r}_t)|^2$  represents the effective erbium concentration over the cross section of the fiber ( $\mathbf{r}_t$ ) overlapping with the signal propagation mode  $\Psi(\mathbf{r}_t)$ .

Equation (2) can be demonstrated knowing that the optical gain along the erbium doped fibers can be described by [7]:

$$G^{dB}(\lambda, L) = [\alpha(\lambda) + \gamma(\lambda)] \cdot \frac{N_2}{N_{Er}} \cdot L - \alpha(\lambda) \cdot L \quad (3)$$

where  $N_2/N_{Er}$  is the mean inversion and  $L$  is the EDF length.

On one hand, the tilt function  $T(\lambda, \lambda_{ref})$ , as shown in (2), should be independent of the length of the EDF. This is experimentally verified and shown in Figure 60. It can be seen that the differences between the two tilt functions corresponding to 10 m and 15 m EDF are less than 0.05 dB. Nevertheless, the 5 m EDF shows higher deviations (max 0.15 dB) at long wavelengths due to the experimental error in  $T(\lambda, \lambda_{ref})$  calculation, since the gain under two different saturation levels vary less at longer wavelengths.

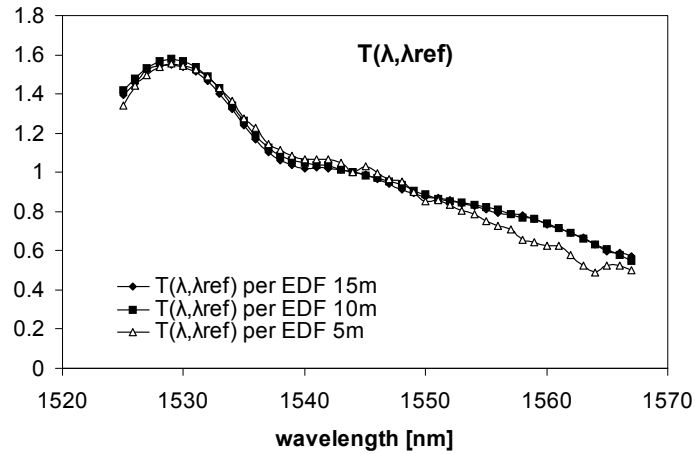


Figure 60: Values of the tilt curve  $T(\lambda, \lambda_{ref})$  for different lengths of the EDF HE980 for a pumping wavelength of 1480nm. The reference wavelength is  $\lambda_{ref} = 1543.73\text{nm}$ ,  $P_p = 12\text{ dBm}$  and  $P_{in} = 0$  and  $-10\text{ dBm}$  for each EDF length

Alternatively to (2), it can be shown, using (3) that:

$$T(\lambda, \lambda_{ref}) = \frac{G_1^{dB}(\lambda, L_1) \cdot L_2 - G_2^{dB}(\lambda, L_2) \cdot L_1}{G_1^{dB}(\lambda_{ref}, L_1) \cdot L_2 - G_2^{dB}(\lambda_{ref}, L_2) \cdot L_1} \quad (4)$$



by considering two gain spectrums  $G^{dB}_1(\lambda, L_1)$  and  $G^{dB}_2(\lambda, L_2)$  measured at different saturation conditions  $(P_{in,1}, P_{p,1})$ ,  $(P_{in,2}, P_{p,2})$  and different EDF lengths  $L_1$  and  $L_2$ .

The BBM (1) can be extended to predict the signal gain,  $G^{dB}(\lambda, P_{in}, P_p, L)$ , at any wavelength  $(\lambda)$ , input signal power  $(P_{in})$ , input pump power  $(P_p)$ , and EDF length  $(L)$ , by using (4). Identifying:  $G^{dB}_1(\lambda, L_1)$  as the signal gain spectrum at the target parameters  $(P_{in}, P_p, L)$ ;  $G^{dB}_2(\lambda, L_2)$  as the gain spectrum at a reference configuration  $(P_{in,ref}, P_{p,ref}, L_{ref})$ ;  $G^{dB}_1(\lambda_{ref}, L_1)$  and  $G^{dB}_2(\lambda_{ref}, L_2)$  as signal gain values at  $\lambda_{ref}$ , at the target and reference configurations respectively, in that case, the signal gain  $G^{dB}(\lambda, P_{in}, P_p, L)$  can be obtained from (4) as:

$$G^{dB}(\lambda, P_{in}, P_p, L) = T(\lambda, \lambda_{ref}) \cdot \left[ G^{dB}(\lambda_{ref}, P_{in}, P_p, L) - \frac{L}{L_{ref}} G^{dB}(\lambda_{ref}, P_{in,ref}, P_{p,ref}, L_{ref}) \right] + \frac{L}{L_{ref}} G^{dB}(\lambda, P_{in,ref}, P_{p,ref}, L_{ref}) \quad (5)$$

In comparison with previous BBM, an extra term, proportional to the difference between reference and target EDF lengths, is formally added to earlier expression (1).

$$G^{dB}(\lambda, P_{in}, P_p, L) = Eq(1) + \frac{(L_{ref} - L) \cdot T(\lambda, \lambda_{ref})}{L_{ref}} \cdot \left[ G^{dB}(\lambda_{ref}, P_{in,ref}, P_{p,ref}, L_{ref}) - G^{dB}(\lambda, P_{in,ref}, P_{p,ref}, L_{ref}) \right] \quad (6)$$

where (6) is an expression equivalent to (5).

The characterization of the gain  $G^{dB}(\lambda_{ref}, P_{in}, P_p, L)$  at the reference wavelength  $(\lambda_{ref})$  can be done using the well known empirical expression[10, 11]:

$$G(P_{in}, P_p, L) = \frac{G_0(P_p, L)}{1 + \left( \frac{P_{in}}{P_{sat}(P_p, L)} \right)^{\alpha(P_p, L)}} \quad (7)$$

where  $G_0$  (small signal gain),  $P_{sat}$  (saturation power) and  $\alpha$  are usually treated as fitting parameters. The values of  $G_0$ ,  $P_{sat}$  and  $\alpha$  depend on the input pump power and EDF fiber length  $(P_p, L)$ . Once a set of representative experimental values are obtained, the value of  $G^{dB}(\lambda_{ref}, P_{in}, P_p, L)$  at any arbitrary conditions can be obtained by interpolating  $G_0(P_p, L)$ ,  $P_{sat}(P_p, L)$  and  $\alpha(P_p, L)$  and using (7). This is a similar procedure as the one proposed in [12] to include pump power dependency. While 1D interpolation is applied in [12], 2D interpolation is used to include EDF lengths dependencies.

### 6.1.3 Experimental Measurements and Theoretical Expression Verification

For experimentally checking the accuracy of the proposed extended BBM, two gain curves at different saturation levels are measured for a EDF  $L_{ref} = 10$  m, and the tilt function  $T(\lambda, \lambda_{ref})$  is



calculated using (2). Also one of the two gain spectra is used as reference gain curve  $G^{dB}(\lambda, P_{in,ref}, P_{p,ref}, L_{ref})$  of the extended BBM (5) and (6).

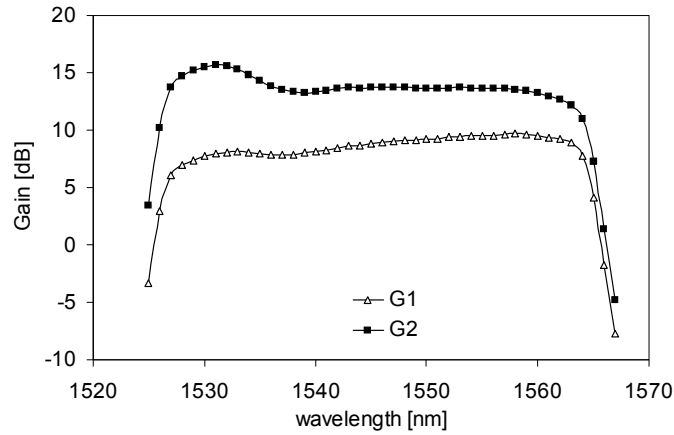


Figure 61: Gain curves at different saturation levels  $G^{dB}_1(\lambda)$  and  $G^{dB}_2(\lambda)$ .  $\lambda_{ref} = 1543.73$  nm,  $P_p = 12$  dBm,  $P_{in} = 0$  dBm for  $G^{dB}_1(\lambda)$  and  $-10$  dBm for  $G^{dB}_2(\lambda)$ .

Secondly, a set of signal gain curves versus input signal power are measured, at reference wavelength  $\lambda_{ref}$ , for a set of EDF lengths and pump powers. For this study:  $L = 2$  m, 10 m, 20 m; and  $P_p = 6$  dBm, 12 dBm, 20 dBm; were chosen. Figure 62 shows the values of  $G_0(P_p, L)$ ,  $P_{sat}(P_p, L)$  and  $\alpha(P_p, L)$  obtained from fitting the experimental measurements with (7).

Once all the experimental data is obtained, without knowing any detail of the amplifier characteristics or internal elements generating extra losses, the gain at reference wavelength  $G^{dB}(\lambda_{ref}, P_{in}, P_p, L)$  is obtained by interpolation of the experimental data shown in Figure 62 and using (7). Finally, using (5) or (6), previous  $T(\lambda, \lambda_{ref})$  and  $G^{dB}(\lambda, P_{in,ref}, P_{p,ref}, L_{ref})$ , the gain for any desired signal wavelength, signal power, pump power and EDF length,  $G^{dB}(\lambda, P_{in}, P_p, L)$ , can be obtained.

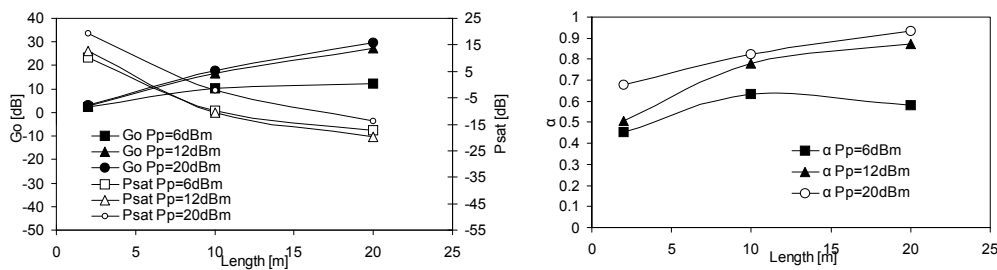


Figure 62: a)  $G_0(P_p, L)$  and  $P_{sat}(P_p, L)$  and b)  $\alpha(P_p, L)$  from the experimental measurements for 2, 10 and 20 m of EDF at  $P_p = 6, 12, 20$  dBm and reference wavelength  $\lambda_{ref} = 1543.73$  nm.

An extra set of gain spectra have been measured for checking the accuracy of the proposed BBM. While the reference wavelength, EDF length and pump power are:  $\lambda_{ref} = 1543.73$  nm,  $L_{ref} = 10$  m,  $P_{p,ref} = 12$  dBm; the measured and calculated gain spectra are compared at longer EDF lengths (15 m) and different signal wavelengths, signal power and pump powers in Figure 63a); and at shorter EDF lengths (2 m) in Figure 63b).

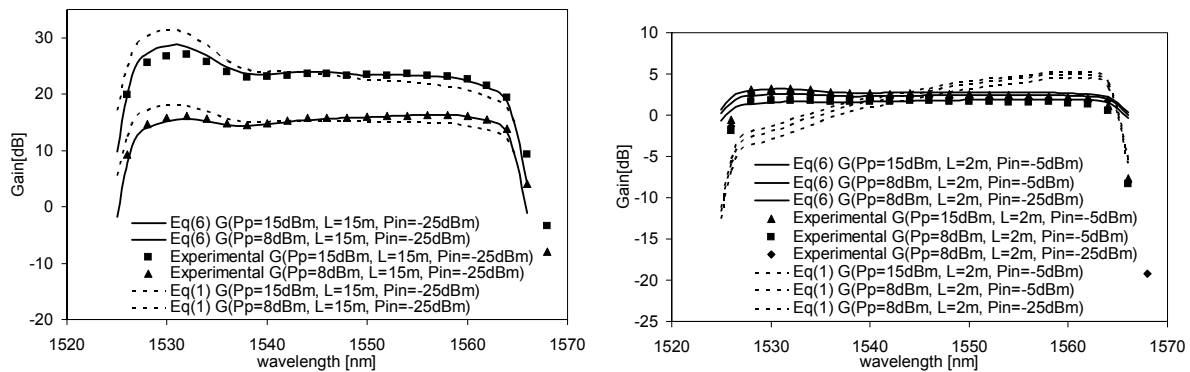


Figure 63: Comparison of experimental gain measurements, using (1) and Extended BBM (6) for 15 m EDF a) and 2 m EDF b) at different pump power and input signals.

As it can be seen in Figure 63a, the calculated gain with the extended BBM, (6), fits very well with the experimental measurements for 15 m of EDF, with differences under 0.5 dB at the 1535 - 1565 nm band; differences increase to 1.5 dB maximum at 1530 nm, the most critical and less used wavelength in system applications. The results obtained using (1) are also shown in Figure 63 for evaluating the relevance of the additional length dependent term, main difference between (1) and (6). For longer EDF lengths, Figure 63a, differences up to 5 dB can be found when neglecting the length dependent term.

Regarding the comparison at shorter EDF lengths, Figure 63b, the new BBM expression, (6), achieves significantly better results: differences under 0.8 dB in the whole spectrum (even under 0.3 dB between 1535 nm and 1560 nm). Also significant differences up to 4.8 dB in the 1530 - 1560 nm regions are found when the length dependent term is not considered (1).

#### 6.1.4 References

- 1 Agrawal G. P., "Fiber-Optic Communications Systems", NY 2002, Wiley
- 2 J. A. Lazaro, V. Polo, F. Bonada, P. Chanclou, C. Kazmierski, J. Prat, "Power Budget Improvement for Passive Outside Plant Long Reach High Density Access Network using High Bit Rate RSOA-ONUs", Proceedings ECOC'07.
- 3 J. A. Lazaro, J. Prat, P. Chanclou, G. M. Tosi, A. Teixeira, I. Tomkos, R. Soila, V. Koratzinos, "Scalable Extended Reach PON", Proceedings OFC'08, (invited) OThL2.
- 4 C. R. Giles, E. Desurvire, "Modeling erbium doped fiber amplifiers", J. Lightwave Technol, vol. 9, pp. 271-283, 1991.
- 5 Rebolledo M. A. et al, "Erbium-doped silica fiber modeling with overlapping factors", Applied Optics, vol. 33, pp. 5585-5593, 1994
- 6 D. Bonnedal, "EDFA Gain described with a Black Box Model", OSA TOPS on Optical Amplifiers and Their Applications, vol. 6, pp. 53-56, 1996
- 7 J. Burgmeier, A. Cords, R. März, C. Schäffer, B. Stummer, "A Black Box Model of EDFA's Operating in WDM Systems", J. Lightwave Technol., vol. 16, pp.271-1275, 1998.
- 8 E. Vanin, U. Persson, G. Jacobsen, "Spectral Functional Forms for Gain and Noise Characterization of Erbium-Doped Fiber Amplifiers", J. Lightwave Technol, vol. 20, pp. 243-249, 2002.
- 9 R. März, Integrated Optics: Design and Modeling. Boston, MA: Artech House, 1995.
- 10 A. Teixeira, D. Pereira, S. Junior, M. Lima, P. André, R. Nogueira, J. da Rocha, H. Fernandes, "Black Box Model of Erbium-Doped Fiber Amplifiers in C and L Bands", 2004.

- 11 X. Zhang and A. Mitchell, "A simple black box model for erbium-doped fiber amplifiers," *IEEE Photon. Technol. Lett.*, vol. 12, pp. 28-30, Jan. 2000.
- 12 G. Jacobsen, U. Persson, L. Gillner, E. Vanin, and S. Wingstrand, "Pump power dependent black box EDFA model", *J. Opt. Commun.*, vol. 21, pp. 675-681, 2000.

## 6.2 State of the art on bursty amplified systems

Optical Burst Switching (OBS) has been proposed as a technique to overcome issues related to WDM deployment (lack of fine granularity in wavelength routing and electronic speed bottleneck in SONET/SDH [1, 2]). In such networks, the data packets are assembled into bursts on the WDM channel and transported across the optical core to the destination. An inherent aspect of this methodology is the existence of long interburst idle intervals (from nanoseconds to seconds). However, this technology is in its early stages and several problems have to be surpassed, namely the amplifier transients. EDFA time response depends on both pump and signal powers. In next generation network, it is also possible to have continuous power variation due to add and drop function of different channels in WDM systems or in bursty systems. Trend of the new optical access networks seems to be that one to realize WDM and bursty network in down and up direction respectively. Here our attention will be concerted on burst mode transmission in amplified system; some example of solution to this problem will be presented and some test, produced in ISCOM, will be reported of EDFA transient effects on burst transmission.

To solve this problem, proposed solutions are:

- Automatic Gain Controlled [3];
- Optical Feedback Loop [4];
- Larger effective area of erbium doped fiber [5].

Nakaji et al. [3] studied gain dynamic at different pump wavelengths (980nm and 1480nm) to understand response speed necessary for pump power control. Due to the difference of gain dynamics for the two pumps, they targeted two different implementations of gain control circuit. Gain fluctuations in EDFA 1480nm pumped are suppressed through an high-speed ACG circuit based on a gain detector. Input and output signal are monitored for this aim (Figure 64, left). When EDFA gain changes ACG circuit imposes to 1480nm laser to change output power. In EDFA 980nm pumped, the high-speed ACG circuit is based on an optical delay time. In this case it is necessary monitoring input power to have the possibility to change pump power before that the input change in EDFA. That is obtained by inserting an optical delay

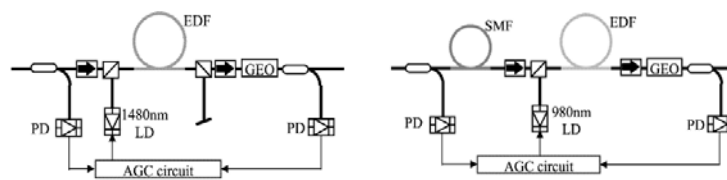


Figure 64: (H. Nakaji et al. / *Optical Fiber Technology* 9 (2003) 25–35) High speed ACG controller in EDFA 1480nm pumped (left) and 980nm pumped (right).

line (SMF in Figure 64, right) between power monitor and power input in EDF. When EDFA gain change ACG circuit change pump power too; this appears during the signal travelling in

SMF before EDF. So when signal arrives in EDF, 980nm has already changes its power and a correct gain is experienced.

Zhao at all [4] performed experiments on a gain control implementing a feedback loop. Important elements of this loop are a Fabry-Perot filter and two long period gratings (Figure 65); their resonance wavelengths are tuned bending the fiber section containing the grating. Grating losses change with resonance. Filter band has to stay in gain window of the EDFA and in attenuation window of the gratings. For different roundtrip loss of each wavelength it is possible to realize single or dual lasing operation and so a single or dual control laser. This structure reduces gain fluctuations thanks to a clamped gain.

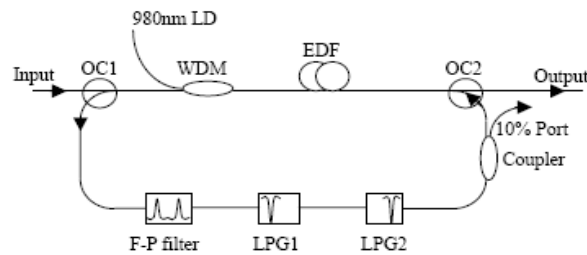


Figure 65: (C.-L. Zhao et al. / *Optics Communications* 225 (2003) 157–162)

Awaji at all [5] proposed to use an erbium doped fiber with larger effective area obtaining a reduce transient on for optical packet of 400ns at single wavelength or WDM signal. Advantage of this technique is the not necessity to use other component to monitoring power or to realize feedback loop. This solution is improved introducing a gain flattening filter (GFF) to flatten the gain for WDM signal (Figure 66). In their scheme the GFF is a mid-GFF with an over pumping scheme. Over pumping produced a saturated gain to reduce transient effects due to power changing. To reduce transient effects induced by wavelength change is necessary use the GFF too.

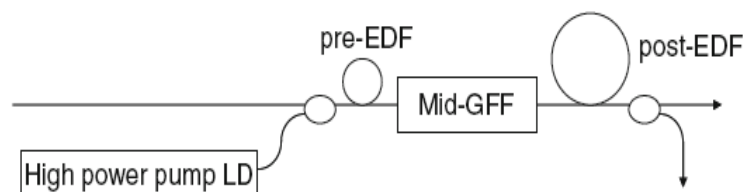


Figure 66: (Awaji, Furukawa, Wada, Kong, Chan, Man, *ONDM2007 Proc*)

## 6.2.1 References

- [1] R. Randhawa, J. L. Sohal: Investigations on burst length in optical burst switched networks, *Opt. Int. J. Lighth Electron. Opt.* (2008).
- [2] E. Zouganeli, A. Solem, H. Kjønberg, R. Andreassen, B. Feng, N. Stol, A. Sudbø, B. Helvik: Techno-economic evaluation of optical packet/burst switching, *ECOC 2005, Th.3.4.7*, 2005.
- [3] Nakaji, H., Nakai, Y., Shigematsu, M., Nishimura, *Optical fiber technology* 9 (2003) 25-35.
- [4] Zhao, C-L., Tam, H-Y., Guan, B-O., Dong, X., Wai, P. K. A., Dong, X. *Optics communications* 225 (2003) 157-162.
- [5] Awaji, Furukawa, Wada, Kong, Chan, Man, *Proc ONDM2007*.

### 6.3 Amplification in different kinds of amplification systems

Laser signal at 1555nm is amplitude modulated by electroabsorption modulator controlled by a Pulse Pattern Generator Anritsu MP1763B, as reported in Figure 67. Pulse Generator allows to create PRBS sequence spacing with zero sequence to obtain burst generation. In this configuration, we analyzed the burst signal travelling in EDFA versus optical input power in amplifier and versus optical pumping of doped fiber.

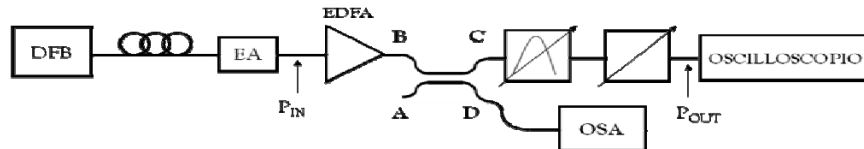


Figure 67: Test-bed set up

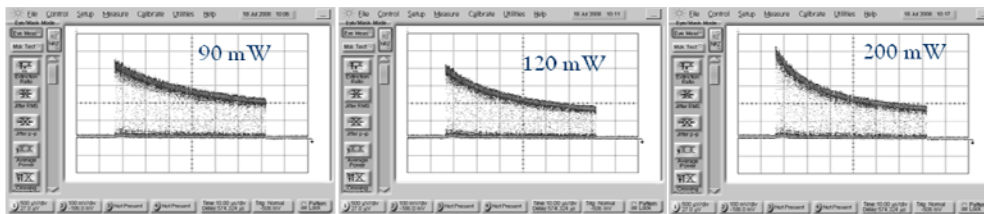


Figure 68: Transient effects vs. pump power.

Experimental results show that pump power increase generate a growth of packet distortion due to a stronger transient effect. In Figure 68 are pictured the effects due to a pump signal of 1100mA and 1600mW.

This configuration has been used to evaluate the behavior of two burst that run through a GC SOA. A signal produced by a DFB laser placed at 1500 nm, has been amplified by an EDFA and modulated by an electro-absorption modulator (EAM). At this point, with a 50% coupler two paths with different delays was introduced to guarantee two bursty signal with different characteristics. GC SOA was driven with current up to 200 mA and a temperature fixed to 25°C. The output was filtered and sent to the oscilloscope to evaluate the GC SOA behavior.

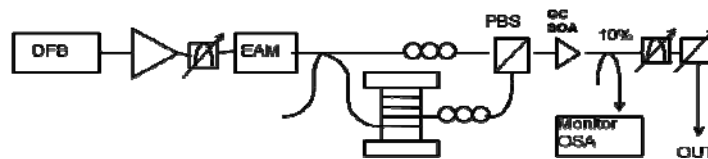


Figure 69: Experiment Set-Up.

A total burst composed by a first burst and a second burst take after the optical fibre, has been sent in input to a GC SOA; the input signal is shown in the following picture:

Varying the current that driver the SOA amplifier we have obtained different amplifier levels. The current was varied between 100 mA up to 200 mA. We show the output in the next figure:

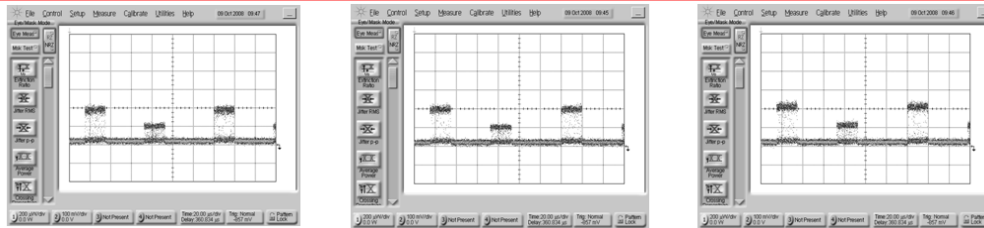


Figure 70: GC Output with different values of driver current.

These are the output signals after the filter and the attenuator using three different values of SOA driver current: 100 mA; 150 mA and 200 mA respectively.

Considering that the modern telecommunications adopt also Raman amplification as distributed technique, a comparison between RAMAN and EDFA amplification for packet based optical system at 10 Gb/s must be considered. The packets used are obtained by intercalating PRBS bits with zero bits with packet sizes equal to: 5000 bits, 10000 bits, 15000 bits and 20000 bits, having in all off time and equivalent to the previous burst size.

The implemented experimental setup consists of an external cavity laser peaking at 1550 nm, followed by a polarization controller and a Mach-Zehnder external modulator driven at 10 Gbit/s. After passing by an optical isolator the optical signal is injected into 45 km of standard single mode fiber (SSMF). As a receiver, a NEL photonic packet receiver an Agilent digital oscilloscope and an Anritsu BER tester were used. To achieve backward Raman amplification we use a Fitel HPU-CL12W pump set , containing 14 pump lasers, at the following wavelengths: 1410.0; 1410.2; 1416.9; 1417.3; 1424.2; 1429.8; 1437.9; 1444.3; 1452.1; 1458.1; 1465.5; 1472.6; 1494.8 and 1502.4 nm. The aggregate optical power is equal to 1029 mW. To achieve EDFA amplification, an identical scheme was implemented taking into account that the output power in both cases was equal to 0 dBm.

The obtained results are plotted in Figure 71 and Figure 72. Figure 71 depicts the results for the system BER with the two amplification schemes; Raman and EDFAs. The difference between the two configurations power penalties is 1.1 dB (at  $10^{-11}$ ), being more penalizing for the EDFAs amplification scheme. This could be mainly due to the ASE noise and to transient effect associated with the EDFAs.

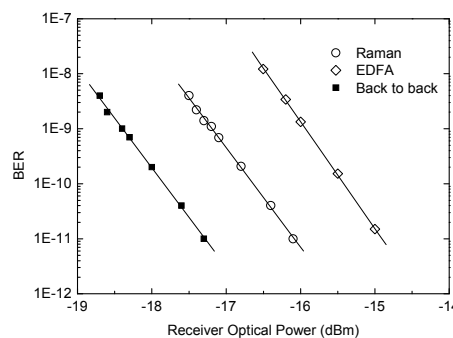


Figure 71: Experimental BER for the Raman and EDFA amplification, the back to back situation is also displayed. The lines are visual guides.

Figure 72 depicts the transient effects in the time domain by observing the bit sequence on the oscilloscope, for each amplification scheme.

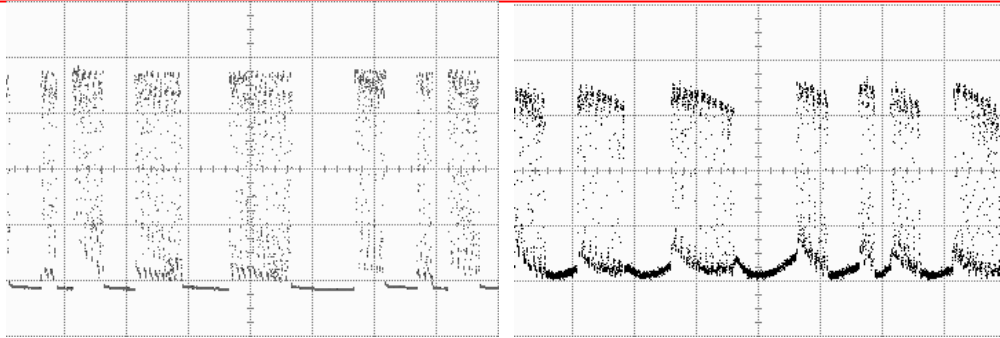


Figure 72: Bit sequence at the receiver: Left – Raman amplification, right– EDFA amplification. The vertical scale is arbitrary and the horizontal scale is 500 ns /div.

## 7. Monitoring (GET, Huawei)

### 7.1 Chromatic-Dispersion Monitoring based on PM-AM Conversion

A scheme for chromatic dispersion monitoring based on phase modulation-amplitude modulation (PM-AM) conversion is proposed. A nonlinear element (NLE) used as a phase modulator is introduced to improve the performance of the chromatic dispersion monitoring. The scheme is investigated numerically for 40-Gb/s data of NRZ, RZ and CSRZ. The monitoring range can be 1670-ps/nm and the sensitivity can be as high as 0.012-dB/(ps/nm) for NRZ data. The corresponding values for RZ50 and CSRZ are 680-ps/nm and 0.0046-dB/(ps/nm), 620-ps/nm and 0.0092-dB/(ps/nm), respectively.

#### 7.1.1 Introduction

In the high speed optical transmission system, optical impairments that signal suffered, such as ASE noise, chromatic dispersion (CD), self-phase modulation (SPM), polarization mode dispersion (PMD), cross talk, filtering effects, cross phase modulation (XPM) and four-wave mixing (FWM), etc., are increasing. It is becoming necessary to monitor and mitigate or eliminate them in order to maintain the optical signal quality acceptable. For CD monitoring (CDM), depending on the object detected the methods can be classified into two categories. One is the transmission media oriented no matter with or without the participation of optical signal itself and spectrum domain is concentrated. The other one is the optical signal itself oriented and temporal domain is concentrated. The former comprises the power or phase detection based on side band [3, 5, 9, 10], clock component detection [2, 4, 6, 11] or pilot tone [7, 8, 12, 13]. The operation time scale of micro-second is the prominent strongpoint of the medium oriented CDM. However, the applied scope of medium oriented CDM is limited to the coupling degree between its results and the deteriorated signal. The latter leads to the sample analysis and the complexity dramatically reduced in cost of the increased computation complexity. The reliability of the results is subject to the accuracy and the amount of the aggregate as well as the algorithm. To avoid the above disadvantages, we propose a novel CDM scheme which tries to use the whole signal as the investigation object and deduce a solid outcome as the reference for tunable chromatic dispersion compensator.

#### 7.1.2 Principle

The chromatic dispersion is rooted from the diverse speed for different wavelengths in transmission medium. The subsequent envelope of the signal will fluctuate consequently. It is unfeasible to extract the fluctuation directly due to the attribute of its transient character. A practical approach is to measure the power change through converting the fluctuation into the average power change.

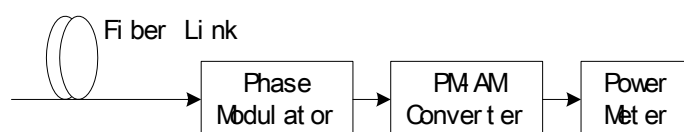


Figure 73: Conceptual block diagram for CDM



The schematic diagram of the proposed scheme is shown in Figure 73. The signal suffered from chromatic dispersion inputs into a segment of nonlinear medium (e.g. semiconductor optical amplifier (SOA)) where the temporal phase is modulated due to Kerr effect, while envelope of the signal is kept unchanged. The signal then inputs into an interferometer array where the phase change is converted into envelope change, i.e. phase modulation to amplitude modulation conversion. Finally, the detected average power is used as the index to find out the accumulated CD of the signal. The phase modulator is not essential, but by introducing it, the phase modulation will be strengthened, which will remarkably improve the final detection sensitivity and the chromatic dispersion range.

### 7.1.3 Theoretical Analysis

Phase change of the signal passed through a segment of fiber link with chromatic dispersion  $\phi_{CD}$  and the resultant phase change  $\phi_{CD+NL}$  due to the NLE are shown as equation (1) and (2), respectively.

$$\phi_{CD}(l_1, t) = -\frac{\text{sgn}(\beta_2)l_1|\beta_2|}{T_0^2 + l_1|\beta_2|} \cdot \frac{t^2}{T_0^2} + \frac{1}{2} \cdot \arctan \frac{l_1|\beta_2|}{T_0^2} \quad (1)$$

$$\phi_{CD+NL}(l_1, l_2, t) = \phi_{CD}(l_1, t) + T_0^2 \gamma P_0 l_2 (T_0^4 + \beta_2^2 l_1^2)^{-1/2} \exp\left(-\frac{T_0^2 t^2}{T_0^4 + \beta_2^2 l_1^2}\right) \quad (2)$$

Where  $l_1$  and  $l_2$  are the length of the fiber link and NLE, respectively, and  $t$  is measured in a reference frame moving with the pulse.  $T_0$ ,  $\gamma$  and  $P_0$  are the FWHM of the signal, nonlinear factor and the peak power of the pulse, respectively. For 1550-nm window,  $\beta_2$  is negative. So, equation (1) can be simplified as equation (3).

$$\phi_{CD}(l_1, t) = \frac{l_1|\beta_2|}{T_0^2 + l_1|\beta_2|} \cdot \frac{t^2}{T_0^2} + \frac{1}{2} \cdot \arctan \frac{l_1|\beta_2|}{T_0^2} \quad (3)$$

In PM-AM converter, assume two power-equal branches of the signal are synchronously summed up. Then the total phase change  $\phi(t)$  of the PM-AM converter output signal is

$$\phi(t) = \frac{\phi_{CD}(l_1, t) + \phi_{CD+NL}(l_1, l_2, t)}{2} \quad (4)$$

Although both of the pulse energy after the fiber segment and the NLE are the same as  $\int_{-T_0/2}^{T_0/2} \exp(-t^2/T_0^2) dt$ , the summed-up energy  $E_{PM-AM}$  is the function of the residual dispersion as

$$E_{PM-AM} = f(\beta_2 \cdot l_1) = T_0^2 (T_0^4 + \beta_2^2 l_1^2)^{-1/2} \cdot \int_{-T_0/2}^{T_0/2} \exp\left(-\frac{T_0^2 t^2}{T_0^4 + \beta_2^2 l_1^2}\right) \cos^2\left[\frac{\Delta\phi(t)}{2}\right] dt \quad (5)$$

where  $\Delta\phi(t) = \phi_{CD+NL}(l_1, l_2, t) - \phi_{CD}(l_1, t)$ . In order to increasing the sensitivity it is instructive to add an additional phase change  $\Delta\phi$  between the branches and shift the  $\Delta\phi(t)$  to around  $k\pi \pm \pi/2$ ,  $k$  is integer. Then equation (5) is transformed to (6)

$$E_{PM-AM} = T_0^2 (T_0^4 + \beta_2^2 l_1^2)^{-1/2} \cdot \int_{-T_0/2}^{T_0/2} \exp\left(-\frac{T_0^2 t^2}{T_0^4 + \beta_2^2 l_1^2}\right) \cos^2\left[\frac{\Delta\phi(t) + \Delta\phi}{2}\right] dt \quad (6)$$

### 7.1.4 Experiment and Discussion



Figure 74: Block diagram for CDM

The system configuration is illustrated as Figure 74. The signal is amplified to saturation power of the saturated SOA with pre-amplifier. In the saturated SOA, the phase is modulated due to the variation of the carrier density with the equation  $\partial\phi/\partial l = -\alpha g/2$  where  $\alpha$  is the line-width enhancement factor and  $g$  is the gain of the saturated SOA [1].

Two kinds of interferometer array are studied. One is based on Mach-Zehnder Interferometer (MZI) as shown in Figure 75(a); the other one is based on the multi-branch configuration as shown in Figure 75(b). In Figure 75(a), optical signal is equally or unequally divided into two branches with a splitter. One of them is going through a nonlinear element (NLE) such as a saturated SOA or a segment of high nonlinear fiber (HNLF) which is used as phase modulator. The time delay of the other branch is adjusted, so that the combination of the two branches at the succeeding coupler generates as a notable power change as possible. In the multi-branch configuration, the pre-amplifier EDFA following an optical filter with bandwidth 0.3nm increases the average power to 100mW which is about the saturated power of the nonlinear amplifier SOA B.

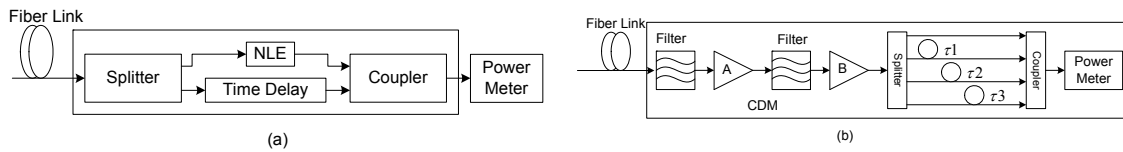


Figure 75: Two kinds of interferometer arrays: (a) active MZI and (b) multi-branch configuration.

#### A7.1.4.1 NRZ system

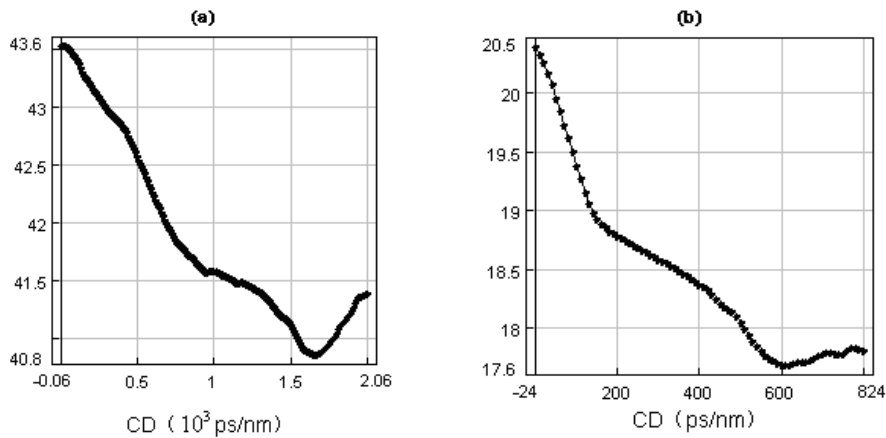


Figure 76: The average power as a function of accumulated chromatic dispersion (CD) for 40Gb/s NRZ data. The CDM configurations are based on (a) active MZI and (b) multi-branch.



The proposed scheme is first verified for 40-Gb/s NRZ signal. For CDM based on the integrated active-MZI, the time delay is set as 1-ps. The average power as a function of the accumulated CD is shown in Figure 76(a). The range is 1670-ps/nm and the sensitivity is 0.0016-dB/(ps/nm). In the multi-branch configuration, the time delays for the branches are  $\tau_1=8\text{ps}$ ,  $\tau_2=17\text{ps}$  and  $\tau_3=2\text{ps}$ , respectively. The range is 600-ps/nm. In the low region smaller than 170-ps/nm the sensitivity is about 0.012-dB/(ps/nm) which is higher than the sensitivity 0.003-dB/(ps/nm) in the high region larger than 170-ps/nm. This property is preferred since the requirement for high sensitivity is much higher when the residual chromatic dispersion is approaching zero. These two sensitivities are improved much better than that of the two-branch configuration where it is as low as foresaid 0.0016-dB/(ps/nm).

#### A7.1.4.2 40-Gb/s RZ system

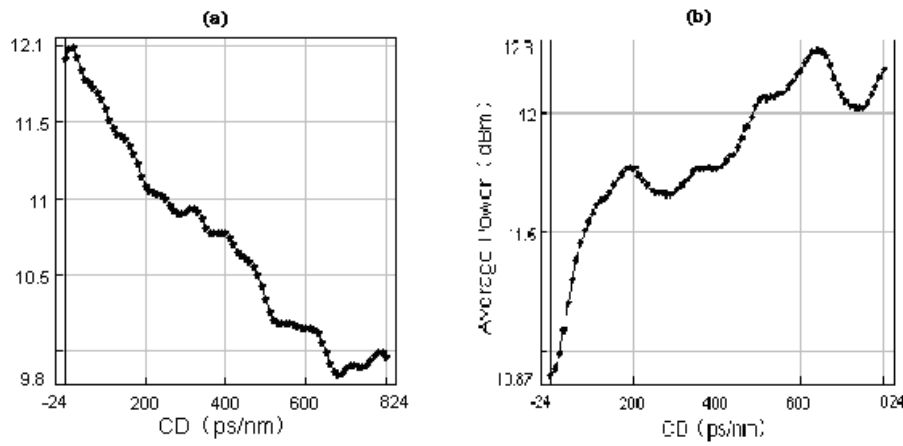


Figure 77: The average power as a function of accumulated chromatic dispersion (CD) for 40-Gb/s RZ50 data. The CDM configurations are based on (a) active MZI and (b) multi-branch.

The proposed scheme for RZ system is also verified. Figure 77 shows the average power as a function of CD for 40 Gb/s RZ50 signal. In Figure 77(a), the time delay for active MZI is 1-ps as well, and the range is 680-ps/nm and the sensitivity is 0.003-dB/(ps/nm). In Figure 77(b), the time delays for the multi-branch are  $\tau_1=3\text{ps}$ ,  $\tau_2=15\text{ps}$  and  $\tau_3=8\text{ps}$ , respectively. The range is 190-ps/nm and the sensitivity is 0.0046-dB/(ps/nm), which is much lower than that of the NRZ data.

### A7.1.4.3 40-Gb/s CSRZ system

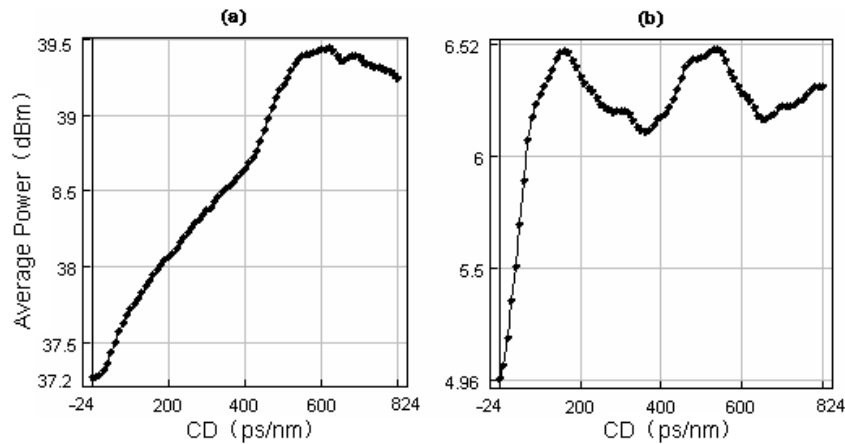


Figure 78: The average power as a function of accumulated chromatic dispersion (CD) for 40-Gb/s CSRZ data. The CDM configurations are based on (a) active MZI and (b) multi-branch.

The experimental results for 40-Gb/s CSRZ data are shown in Figure 78. As expected, the range of the two-branch configuration with time difference 1-ps is about 620-ps/nm, which is larger than 160-ps/nm of the multi-branch configuration with time delays  $\tau_1 = 0\text{ps}$ ,  $\tau_2 = 0\text{ps}$  and  $\tau_3 = 9\text{ps}$ . But the sensitivity of the former is 0.0035-dB/(ps/nm) which is smaller than 0.0092-dB/(ps/nm), the sensitivity of the latter.

### 7.1.5 Conclusion

The proposed scheme has been verified for NRZ, RZ and CSRZ modulation signals at 40-Gb/s. It should be noted that the performance values shown in Table 3 are merely specific configuration oriented. It is potential to improve the performance further more through other more effective configuration.

Table 3. Performance values of the proposed scheme for NRZ, RZ and CSRZ modulation signals at 40-Gb/s

40-Gb/s data	Asynchronous-MZI		Multi-branch Configuration	
	Range (ps/nm)	Sensitivity (dB/(ps/nm))	Range (ps/nm)	Sensitivity (dB/(ps/nm))
NRZ	1670	0.0016	600	0.012
RZ50	680	0.003	190	0.0046
CSRZ	620	0.0035	160	0.0092

### 7.1.6 References

1. Agrawal, G.P. and N.A. Olsson, Self-phase modulation and spectral broadening of optical pulses in semiconductor laser amplifiers. *Quantum Electronics, IEEE Journal of*, 1989. 25(11): p. 2297-2306.
2. Biao, F. and H. Rongqing, Fiber chromatic dispersion and polarization-mode dispersion monitoring using coherent detection. *Photonics Technology Letters, IEEE*, 2005. 17(7): p. 1561-1563.



3. Dimmick, T.E., G. Rossi, and D.J. Blumenthal, Optical dispersion monitoring technique using double sideband subcarriers. *Photonics Technology Letters*, IEEE, 2000. 12(7): p. 900-902.
4. Kuen Ting, T. and W.I. Way, Chromatic-dispersion monitoring using an optical delay-and-add filter. *Lightwave Technology, Journal of*, 2005. 23(11): p. 3737-3747.
5. Nezam, S.M.R.M., et al., Enhancing the monitoring range and sensitivity in CSRZ chromatic dispersion monitors using a dispersion-biased RF clock tone. *Photonics Technology Letters*, IEEE, 2004. 16(5): p. 1391-1393.
6. Pan, Z., et al. Chromatic dispersion monitoring and automated compensation for NRZ and RZ data using clock regeneration and fading without adding signaling. 2001.
7. Park, K.J.Y., C.J.; Lee, J.H.; Chung, Y.C., Performance comparisons of chromatic dispersion-monitoring techniques using pilot tones. *Photonics Technology Letters*, 2003.
8. Petersen, M.N.P., Z.; Lee, S.; Havstad, S.A.; Willner, A.E., Online chromatic dispersion monitoring and compensation using a single inband subcarrier tone. *Photonics Technology Letters*, 2002.
9. Qian, Y., et al., Chromatic dispersion monitoring technique using sideband optical filtering and clock phase-shift detection. *Lightwave Technology, Journal of*, 2002. 20(12): p. 2267-2271.
10. Rossi, G., T.E. Dimmick, and D.J. Blumenthal, Optical performance monitoring in reconfigurable WDM optical networks using subcarrier multiplexing. *Lightwave Technology, Journal of*, 2000. 18(12): p. 1639-1648.
11. Sung-Man, K. and L. Chang-Hee, The efficient clock-extraction methods of NRZ signal for chromatic dispersion monitoring. *Photonics Technology Letters*, IEEE, 2005. 17(5): p. 1100-1102.
12. Takushima, Y., et al., Experimental demonstration of in-service dispersion monitoring in 960-km WDM transmission system using optical frequency-modulation method. *Photonics Technology Letters*, IEEE, 2003. 15(6): p. 870-872.
13. Takushima, Y., et al., In-service dispersion monitoring in 32/spl times/10.7 Gbps WDM transmission system over transatlantic distance using optical frequency-modulation method. *Lightwave Technology, Journal of*, 2004. 22(1): p. 257-265.

## 7.2 Evolution of an OPM prototype for OSNR measurements

### 7.2.1 Introduction

TELECOM Bretagne has been working on a free-space based OPM prototype since 2005 in the framework of a collaboration coordinated by the PERDYN platform ([www.perdyn.fr](http://www.perdyn.fr)). The results achieved during the different phases of this work have been reported in the deliverables D-VD-T.3, D-JP-T.2, D-JP-T.3 of the e-Photon ONE+ NoE.

In this contribution we will briefly summarize the present status of the prototype and discuss the approach we are following in order to address the measurement of the in-band OSNR.

### 7.2.2 Status of the prototype

The key elements of the OPM prototype are a low PDL  $900 \text{ mm}^{-1}$  reflection relief grating and a 512 pixels InGaAs array with  $25 \text{ }\mu\text{m}$  pitch integrated in a commercial linear camera. The selected optical configuration corresponds to a couple of lenses with 30 and 250 mm focal lengths and an incident angle on the grating of 53 degrees. A control software featuring the generation of a table of monitored parameters (power level, wavelength, ITU channel number, out-of-band OSNR), the definition of alarm generation criteria, and the display of these alarms, was developed.

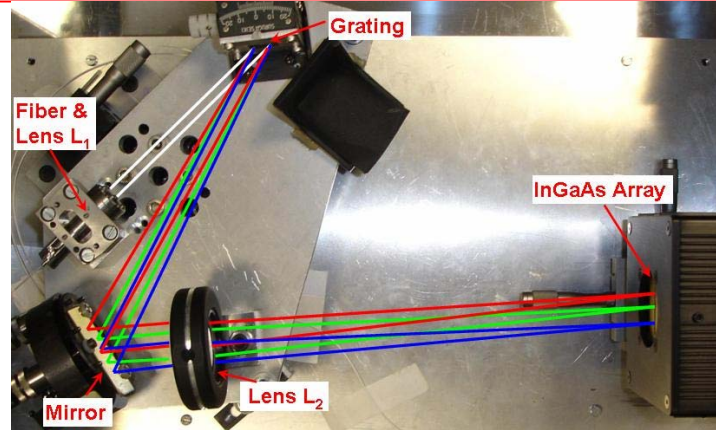


Figure 79 : View of the OPM prototype

Two channel profile reconstruction routines were developed, both based on the assumption of a Gaussian beam profile in the InGaAs array plane. The first one aims to reconstruct each WDM channel individually while the second one fits the acquired data with a sum of Gaussian functions. In order to limit the computing time, this collective reconstruction process is performed across a sliding window whose width is locally adjusted. We have shown that this second method provides a better measurement accuracy of the power and the peak wavelength of the channels. The operation of the OPM has been evaluated in presence of 40 Gbit/s NRZ channels with 100 or 50 GHz spacing.

Since the -3 dB width of our OPM is about 25 GHz, the validity of the Gaussian beam profile approximation will depend on the actual modulation format used at 40 Gbit/s. In particular it is not valid for CSRZ or RZ33% modulation formats. For these formats, one channel will be identified as a group of two (CSRZ format) or three (RZ 33% format) channels. This issue can be solved by controlling the OPM spectral resolution (either by optical means such as a variable aperture or by a digital post-processing of the data generated by the photodetector array) or by changing the shape of the reference functions in reconstruction routine. More details on these points will be given in a future deliverable.

The OSNR measurement represents another feature which should be improved in our OPM prototype. In the present version, the OSNR measurement is based on the peak and valley method, commonly used in Optical Spectrum Analyzers. Taking into account the resolution of our OPM, the OSNR can be measured for channels separated by 90 GHz from their neighbours. This method is then not suitable for a 50 GHz grid; moreover, its assumption of identical noise level in and out the multiplex bands is not valid when WDM channels are filtered by network elements; this is particularly the case with ROADM which are deployed now at an increasingly larger scale. In the next section we will discuss on the different options to introduce in-band OSNR monitoring in our prototype.

### 7.2.3 Introducing in-band OSNR measurement in the OPM prototype

Several techniques have been proposed to measure the in-band OSNR of a single optical channel:

- polarization nulling method [1], [2]
- low frequency beat noise measurement [3]
- uncorrelated beat noise measurement [4]
- orthogonal delayed-homodyne method [5]

- narrowband RF analysis at the half-clock frequency [6]
- sub-carrier multiplexing [7]
- pilot tones [8]
- orthogonal polarization heterodyne mixing [9]
- nonlinear loop mirror [10]
- high birefringent loop mirror [11]

In principle any of these methods may be associated to a power and wavelength monitor in order to provide power, wavelength and in-band OSNR monitoring according to the scheme shown in Figure 80. However it is clear that the insertion loss of a demultiplexer and a  $N \times 1$  switch is very prohibitive in terms of cost and compactness. Moreover the characteristics of the demultiplexer may impact the in-band OSNR measurement. Another possible drawback comes from the sequential procedure for the OSNR measurement which will make slower the monitoring of this parameter. As the speed required for the OSNR monitoring is rather slow ( $\sim 1$  second according to [12]), this point does not seem critical. Anyhow, the integration of the in-band OSNR measurement in a common WDM monitoring platform represents an attractive approach.

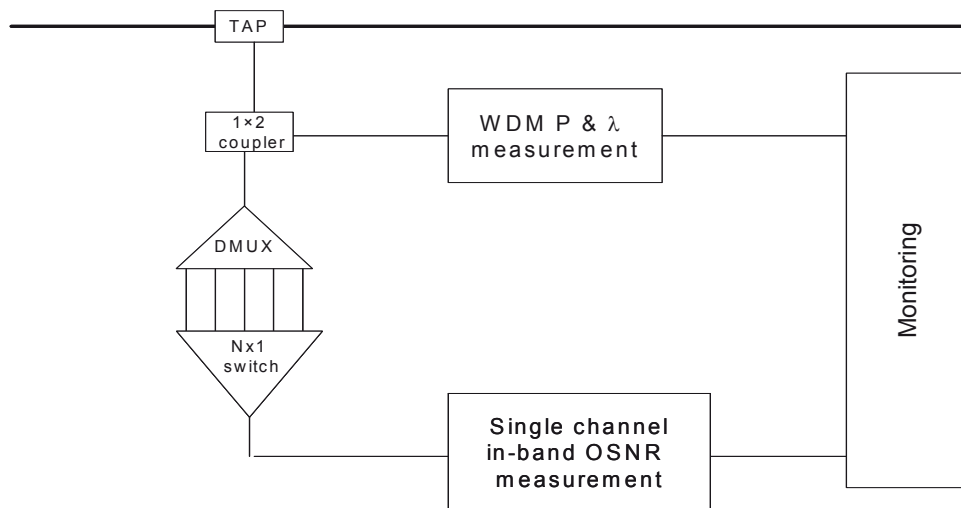


Figure 80 : Association of a multi-channel power & wavelength monitor with a single channel in-band OSNR monitor.

However most of the available methods seem difficult to integrate in the OPM structure that we developed: the fibre loop-based techniques use a specific per channel optical set-up and the techniques which involve an electrical signal analysis require an electrical bandwidth which is not compatible with the characteristics of the available detector arrays. Therefore, in spite of its limitations in presence of PMD, non-linear birefringence and PDL, the polarization nulling method seems to be the most suitable to be associated with our OPM prototype and could constitute a convenient trade-off in terms of cost and monitoring performance.

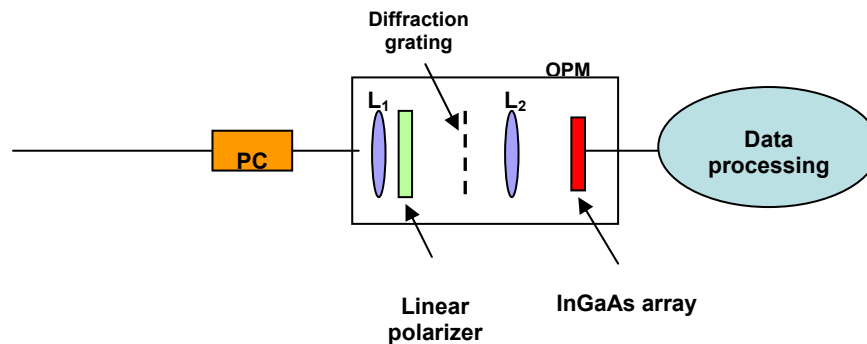


Figure 81 : Schematic of the OPM prototype modification to implement in-band OSNR measurement.

Figure 81 shows schematically how the OPM prototype has to be modified to include an OSNR measurement feature using the polarization nulling method. A polarization controller is placed before the input of the prototype and a linear polarizer is inserted in the OPM set-up, between the input lens  $L_1$  and the diffraction grating.

For a given channel, the input polarization is adjusted in order to minimize the channel power and then the linear polarizer is rotated by  $90^\circ$  and the corresponding channel power is acquired. These two power values allow calculating the in-band OSNR of this channel (assuming un-polarized noise). There are different options to make this procedure automatic, for instance by using a polarization beam-splitter and two detector arrays.

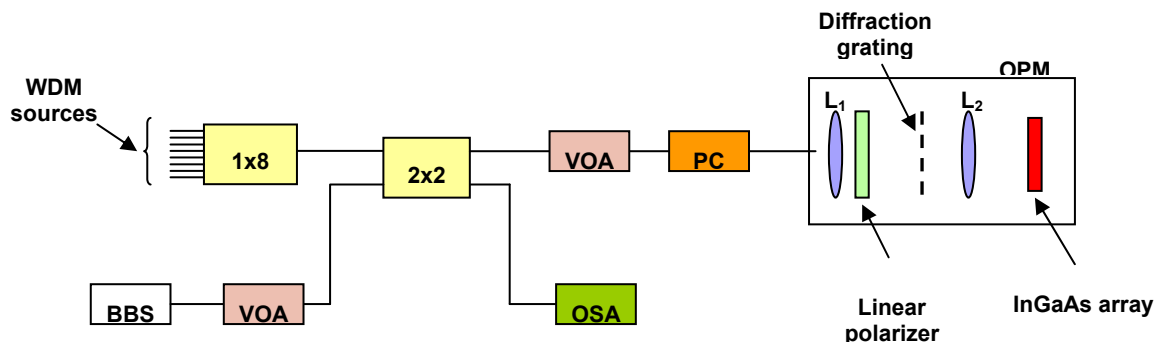


Figure 82 : Experimental set-up for the characterization of the in-band OSNR monitoring with the OPM.

We performed preliminary tests of the proposed configuration using the experimental set-up shown in Figure 82 which allows to compare the OSNR values measured with an Optical Spectrum Analyzer and the out-band and in-band OSNR values provided by the OPM. We checked that the polarization nulling method yields the same results than the present out-of band method in presence of a broadband noise source.

The next phase of our study will be focused on the evaluation of the feasibility of this approach in presence of a WDM multiplex. The issues to be addressed include the in-band OSNR measurement in presence of a narrow-band noise and the extension of the measurement algorithm for a group of 50 GHz-spaced channels with different polarization states.



#### 7.2.4 References

- [1] S. K. Shin et al., "A novel optical signal-to-noise ratio monitoring technique for WDM networks," OFC conference, March 2000, Vol. 2, pp. 182-184.
- [2] J. H. Lee et al., "A review of the polarization-nulling technique for monitoring Optical-Signal-to-Noise-Ratio in dynamic WDM networks," *Journal of Lightwave Technology*, Vol. 24, No. 11, November 2006.
- [3] M. Bakaul et al., "Low-cost in-band Optical-Signal-to-Noise Ratio monitoring using an optical interferometer," *IEEE* 2006, pp. 970-971.
- [4] W. Chen et al., "Optical Signal-To-Noise Ratio Monitoring using uncorrelated beat noise," *IEEE Photonics Technology Letters*, Vol. 17, No. 11, November 2005, pp. 2484-2486.
- [5] C. J. Youn et al., "OSNR monitoring technique based on orthogonal delayed-homodyne method," *IEEE Photonics Technology Letters*, Vol. 14, No. 10, October 2002, pp. 1469-1471.
- [6] H. Stuart, "Signal-to-Noise-Ratio monitoring of optical data using narrowband RF analysis at the half-clock frequency," OFC, 2003, pp. 407-409.
- [7] G. Rossi et al., "Optical performance monitoring in reconfigurable WDM optical networks using Subcarrier multiplexing," *Journal of Lightwave Technology*, Vol. 18, No. 12, December 2000, pp. 1639-1648.
- [8] H. C. Ji *et al.*, "Optical performance monitoring techniques based on pilot tones for WDM network applications," *Journal of Optical Networking*, Vol.3, No. 7, July 2004, pp. 510-533.
- [9] X. Chongjin, D. C. Kilper, L. Moller, and R. Ryf, "Orthogonal-Polarization Heterodyne OSNR Monitoring Insensitive to Polarization-Mode Dispersion and Nonlinear Polarization Scattering," *J. Lightwave Technol.*, vol. 25, pp. 177-183, 2007.
- [10] R. Adams, M. Rochette, T. Ng., and B. J. Eggleton, "All-Optical In-Band OSNR Monitoring at 40 Gb/s using a Nonlinear Optical Loop Mirror," *IEEE Photon. Technol. Letters*, vol.18, no.3, Feb. 2006.
- [11] E. Wong, J. Tan, and A. Nirmalathas, "Novel Scheme for Simultaneous Polarization Mode Dispersion and Optical Signal-to-Noise Ratio monitoring," in *ECOC 2005 Proc.*, vol. 3, pp. 697-698, 2005.
- [12] A. Texeira et al., "An Integrated View on Dynamic Monitoring and Compensation for Optical Networks: From Management to Physical Layer" submitted to *Photonics Networks Communications*.

## 8. Other transmission-related joint activities within BONE

### 8.1 *Polarisation-related phenomena in fibre Bragg gratings (UPVLC, FPMs)*

#### 8.1.1 *Introduction*

Fiber Bragg gratings (FBGs) have attracted considerable attention in the recent years because of their numerous applications in optical fiber technology [1]. Uniform FBGs are characterized by a constant periodic modulation of the core refractive index. They act as narrowband reflection filters centered around the Bragg wavelength. Phase-shifted FBGs are slightly more complex structures since they exhibit a transmission notch within the reflection band of the spectral response. They allow the achievement of specific telecommunication applications such as channel selection in a multichannel communication system [2], all-optical switching [3], pulse shaping [4] and tunable optical filtering [5]. They can also be advantageously used for sensor applications to measure the transverse load [6].

Both uniform and phase-shifted FBGs are commonly manufactured by transversally irradiating one side of an optical fiber with an intense UV interference pattern. It is generally admitted that this side-written fabrication process induces a small quantity of birefringence that combines with the intrinsic fiber birefringence and leads to polarization dependence within the grating [7, 8]. While this small amount of birefringence slightly affects the grating spectral response, it causes the orthogonal polarization modes to experience different couplings through the grating. In terms of polarization properties, it leads to polarization dependent loss (PDL), differential group delay (DGD) and particular normalized Stokes parameters evolutions with wavelength.

Monitoring the polarization properties of FBGs is of high interest to perceive their impact in transmission systems as well as to develop new demodulation techniques for simultaneous strain and temperature FBG sensors [9]. In the framework of the BONE network it has been done a complete analysis in that field, studying, both theoretically and experimentally, the wavelength dependency of PDL, DGD and normalized Stokes parameters associated with the transmitted spectrum of phase-shifted and uniform FBGs written into photosensitive single mode fiber. The Jones formalism and the solutions of the coupled mode equations have been used to derive theoretical expressions for the normalized Stokes parameters of phase-shifted FBGs. PDL and DGD evolutions with wavelength have been computed using the same mathematical formalism. It has been shown that all the measured polarization properties evolutions can be accurately and rapidly simulated using the derived relationships, which is valuable to design optical systems or to evaluate their performances. Moreover, several techniques to reduce the birefringence induced by the inscription process have been studied. Finally, the study of the polarization properties has been applied to the sensing of transversal forces on fiber Bragg gratings.

#### 8.1.2 *Influence of the grating parameters on the polarization properties of fiber Bragg gratings.*

As mentioned before, due to the lateral inscription process, photo-induced birefringence is present in fiber Bragg gratings (FBGs) written into photosensitive single mode fiber. The

birefringence value is generally too small to be perceived in the grating spectral response but it can lead to significant polarization dependent loss (PDL) values and differential group delay (DGD) evolutions. The evolution of the PDL and the DGD as a function of the grating parameters and the birefringence value have been theoretically analyzed [10]. It has been shown that the PDL and the DGD values with wavelength can be strongly enhanced by a modification of the grating parameters. For example, Figure 83 shows the influence of the grating length on the PDL and the DGD. Simulations carried out using the coupled mode theory and the Jones formalism have been confirmed by experiments conducted on FBGs written into photosensitive single mode fiber. Figure 84 shows the good agreement between theory and experiment for the PDL and the DGD evolutions of 1-cm long  $\pi$ -shifted fiber Bragg grating.

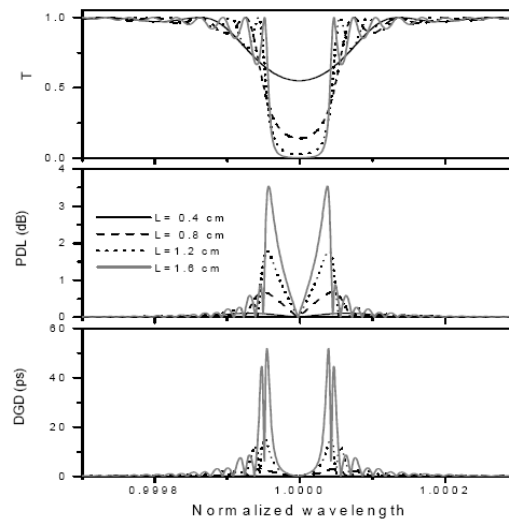


Figure 83: Evolution of the transmission, PDL and DGD curves as a function of the grating length.

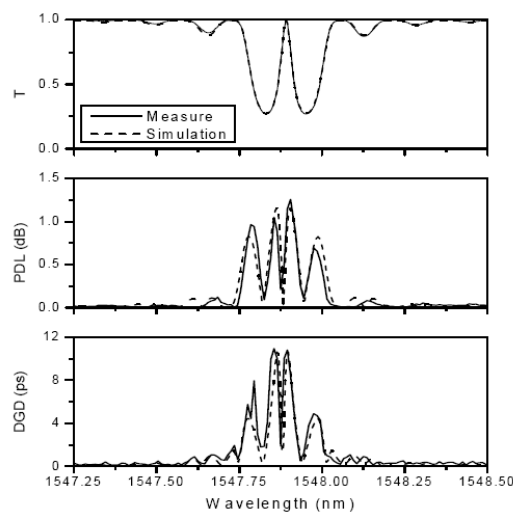


Figure 84: Comparison between experimental and simulated evolutions for a 1 cm long  $\pi$ -shifted FBG.

This work brings a complete characterization of polarization related phenomena in FBGs and presents a great interest for the evaluation of system performances and the design of gratings for specific applications, either for telecommunications or sensing purposes.

### 8.1.3 Reduction of birefringence in fiber Bragg gratings by using a twisted fiber for inscription.

For telecom applications, especially in the context of high bit rate transmissions where polarization dependent properties are critical, it is essential to obtain components with low Polarization Dependent Loss (PDL) and Differential Group Delay (DGD) values. The studies on the polarization properties of FBGs report that gratings can exhibit significant PDL and DGD values. In this context, it is therefore important to find solutions to reduce the PDL and DGD of these devices. It has been studied the possibility to reduce these values by using an original manufacturing technique that introduces polarization mode coupling into the FBG [11, 12]. This technique consists on use a manufacturing setup in which the grating is written in a twisted fibre along its axis; the fibre is then relaxed after the writing process. The degree of coupling is then related to the twist rate. As it can be observed in Figure 85, the values of DGD and PDL are greatly reduced by using this manufacturing technique.

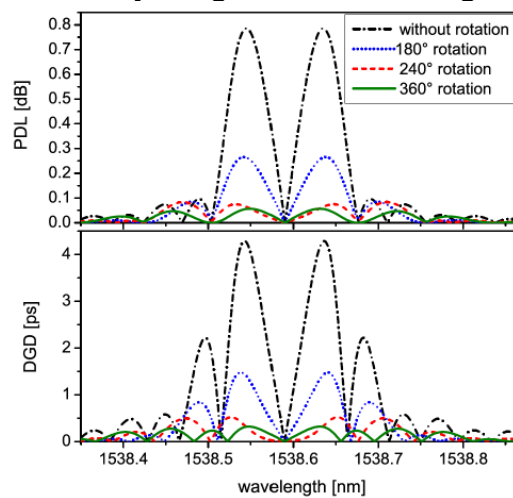


Figure 85: PDL and DGD of twisted FBG (simulation)

### 8.1.4 Application of the study of the polarization properties to sensing of transversal loads.

In this study it has been demonstrated that that the PDL and DGD curves of uniform FBGs written into standard single mode fiber contain the information to realize temperature-insensitive transverse strain sensors, which is not possible via amplitude spectral measurements [13-14]. In the experiments, FBGs were placed between two metal plates and the load was applied by a stepper motor that presses the upper rectangular compressing plate. The transverse force was applied in the range 0 N – 500 N by steps of 50 N. Figure 86 presents some results obtained in the transmitted spectrum of the PDL and DGD curves of a 5 mm long FBG. It can be observed that, for transverse force values ranging between 0 N and 300 N, the birefringence generated by the transverse load is too weak to obtain a discrimination between the  $x$  and  $y$  modes. However, the PDL and DGD evolutions present two main peaks whose amplitudes evolve as a function of the transverse force value. This strong amplitude variation can be advantageously used for sensing of transversal forces on FBGs.

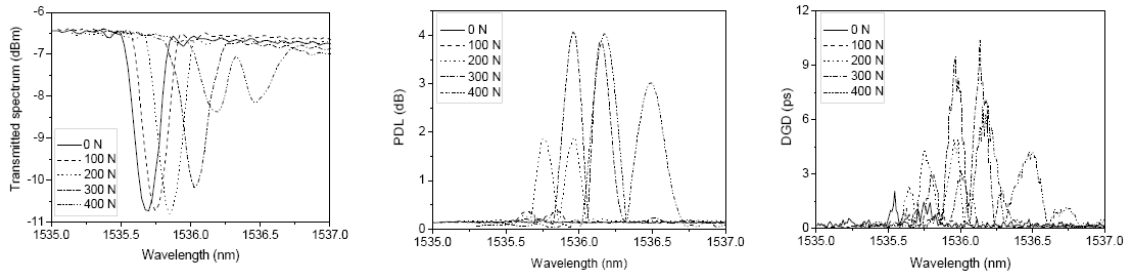


Figure 86: Transmitted spectrum, PDL and DGD evolutions as a function of the transverse force value.

### 8.1.5 References

1. A. Othonos, K. Kalli, Fiber Bragg gratings: fundamentals and applications in telecommunications and sensing (Artech House, Norwood, MA, 1999).
2. G.P. Agrawal, S. Radic, "Phase-shifted fiber Bragg gratings and their application for wavelength demultiplexing", IEEE Photon. Technol. Lett. **8**, 995-997 (1994).
3. A. Melloni, M. Chinello, M. Martinelli, "All-optical switching in phase-shifted fiber Bragg grating", IEEE Photon. Technol. Lett. **12**, 42-44 (2000).
4. G. Curatu, S. Larochele, C. Paré, P.A. Bélanger, "Pulse shaping with a phase-shifted fiber Bragg grating for antisymmetric pulse generation", in SPIE Proceedings of Photonics West, Optical Pulse and Beam Propagation **4271**, 20-26 January, San José, USA, 1-9 (2001).
5. Y. Lai, W. Zhang, L. Zhang, J.A.R. Williams, I. Bennion, "Optically tunable fiber grating transmission filters", Optics Letters **28**, 2446-2448 (2003).
6. M. LeBlanc, S.T. Vohra, T.E. Tsai, E.J. Friebele, "Transverse load sensing by use of pi-phase-shifted fiber Bragg gratings", Optics Letters **16**, 1091-1093 (1999).
7. T. Erdogan, V. Mizrahi, "Characterization of UV-induced birefringence in photosensitive Ge-doped silica optical fibers", J. Opt. Soc. Am. B **11**, 2100-2105 (1994).
8. A. M. Vengsarkar, Q. Zhong, D. Inness, W. A. Reed, P. Lemaire, S. G. Kosinski, "Birefringence reduction in side-written photoinduced fiber devices by a dual-exposure method," Opt. Lett. **19**, 1260-1262 (1994).
9. S.T. Oh, W.T. Han, U.C. Paek, Y. Chung, "Discrimination of temperature and strain with a single FBG based on the birefringence effect," Optics Express **12**, 724-729 (2004).
10. C. Caucheteur, S. Bette, R. Garcia-Olcina, M. Wuilpart, S. Sales, J. Capmany, P. Mégret, "influence of the grating parameters on the polarization properties of fiber bragg gratings", Journal of Lightwave Technology (Accepted), 2008.
11. S. Bette, C. Caucheteur, V. García-Muñoz, R. Garcia-Olcina, M. Wuilpart, S. Sales, J. Capmany, M. Muriel, P. Mégret, "Experimental demonstration of the reduction of PDL and DGD in fibre Bragg gratings by using a twisted-fibre for the inscription", European Conference On Optical Communications (ECOC), Vol. 3, Pp. 157-158, Paper We3b1, Brussels
12. Sébastien Bette, Christophe Caucheteur, Victor García-Muñoz, Raimundo Garcia-Olcina, Marc Wuilpart, Salvador Sales, Patrice Mégret, "Demonstration expérimentale de la réduction de la PDL et du DGD des réseaux de Bragg par inscription dans des fibres tournées", to be published in Journées Nationales d'Optique Guidée, Lannion (F), 20/10-22/10, 2008 (2008/10/20), 2008.
13. Sébastien Bette, Christophe Caucheteur, Raimundo Garcia-Olcina, Marc Wuilpart, Salvador Sales, Patrice Mégret, "Détermination De La Birefringence Induite Par Une Contrainte Mécanique Transverse A Partir De La Mesure Des Paramètres De Polarisation D'un Réseau De Bragg Fibre", to be published in Journées Nationales d'Optique Guidée, Lannion (F), 20/10-22/10, 2008 (2008/10/20), 2008., 2008.
14. C. Caucheteur, S. Bette, R. Garcia-Olcina, M. Wuilpart, S. Sales, J. Capmany, P. Mégret, "Polarization properties related to fiber Bragg gratings in the presence of birefringence: analysis and application to sensors", (invited) First Mediterranean Photonics Conference, Vol. 1, Pp. 21-25, Ischia, Italy, June 2008.

## 8.2 Algorithms for tuning and controlling local wavelength in coherent detection of multilevel PSK signals (UPC, HHI)

### 8.2.1 Introduction

In this joint activity, many approaches for the optical frequency estimation problem were considered. The designs we decided to take into account were included in both digital and analogue domains.

For the digital domain we investigated two approaches, the off-line processing and the real-time approach. Whereas for the analogue domain we took into account several designs coming from RF techniques [1], also with the ones tested in optical communications [2].

### 8.2.2 Off-line

For the off-line approach, the same receiver architecture is used, almost all times. A sketch of it is shown in Figure 87. Here the challenge is in the development of feed-forward processing algorithms that can compensate the frequency offset between local laser and received signal. Two remarkable references studying this are [3] and [4]. Ref. [3] shows a nice and easy approach to solve the problem, while [4] is more complex, but it can compensate a span of  $\pm 5$  GHz.

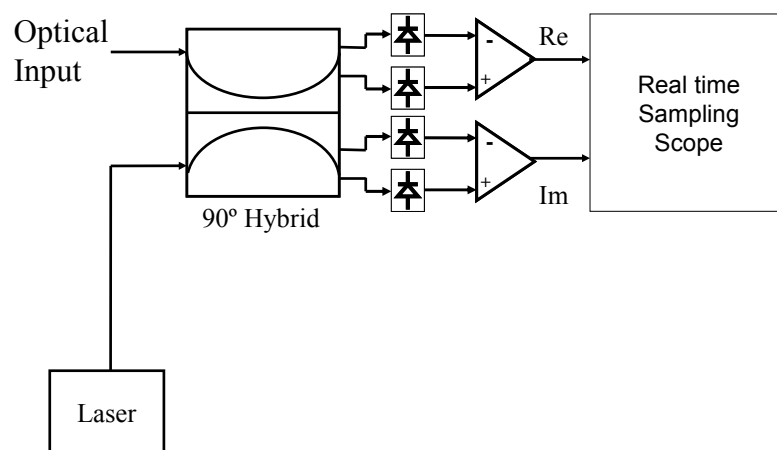


Figure 87: Schematic of a generic off-line receiver

### 8.2.3 Digital Realtime

Off-line processing is open and nice, but it is not implementable with the technology that nowadays we can use or handle. That is the reason why we are studying another digital approach, a real-time one. A schematic of that system could be the one displayed on Figure 88. In principle, the idea is to keep the frequency discrimination in the analog domain. Next an ADC (low-speed) is placed. It can be low-rate (up to 1 MSa/s) because of the low bandwidth of the error signal. Afterwards, comes the signal processing block, which can be a classical one (PI control) or a more advanced (nonlinear). Next, the signal output of the DSP is driven to the optical VCO.

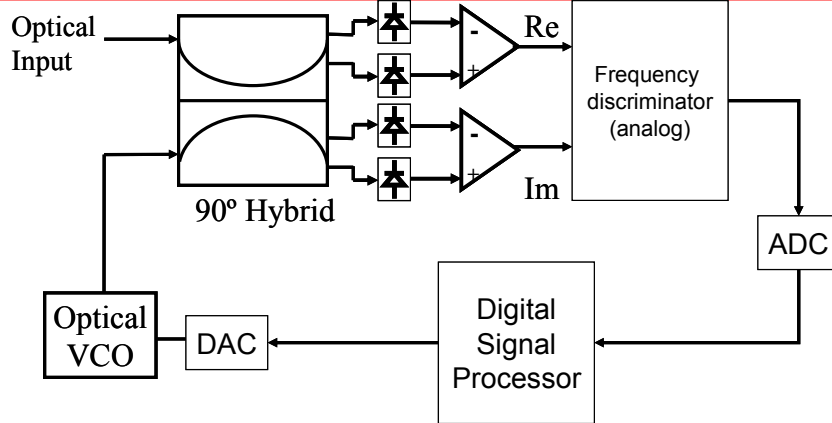


Figure 88: Schematic of a digital real-time loop

This approach is affected by several important parameters. The first one is the frequency discriminator implementation, while the second, and more important, is the overall loop delay.

Frequency discriminator is limiting the frequency range that we will be capable to track and compensate, and also its linearity will be limiting the performances of all the system.

The loop delay will limit the loop bandwidth, as it happens in the optical PLLs. So we will have a residual frequency error that we will not be able to compensate.

#### 8.2.4 Analogue approach

This is the main approach we are working on. We are focusing on the implementation of this architecture, but not discarding the others shown.

The frequency discriminator is just a delay-and-multiply architecture; that works pretty well [2]. However, for avoiding high amplitude changes at the electrical part, we are thinking about using a digital discriminator, replacing the analog multipliers by XOR gates.

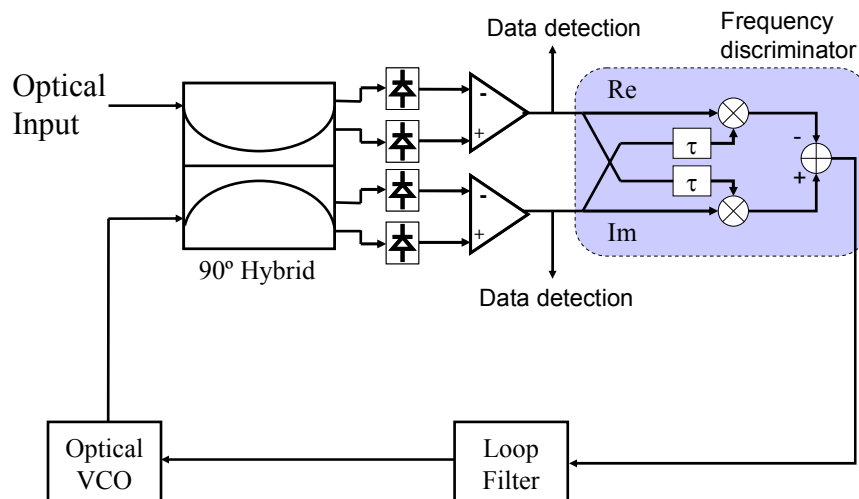


Figure 89: Scheme of the proposed analog frequency estimation loop

For the optical VCO, things are not so clear, and we have been thinking on 3 different approaches.

The first one, is a true optical VCO, very fast and reliable. Is an optical VCO that can be controlled like an electrical one. A schematic is shown in Figure 90. To our knowledge, it was first developed at PoliTo. However, its architecture is somewhat complex (and maybe high-cost). The objective is to control a Single SideBand (SSB) tone modulation of the local laser. That is the reason why an IQ modulator is used. Details of its performance and characterization for using it in optical phase-locking can be found on [5].

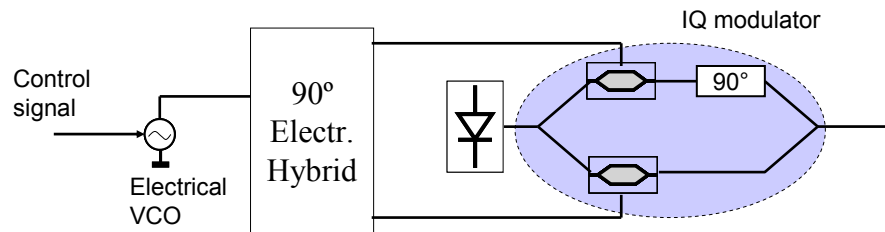


Figure 90: Diagram of the optical VCO

The other 2 are more simple approaches. One is based on tuning the current of the phase section of a GCSR laser. It presents some difficulties for setting an operating point, and could exhibit some hysteresis, depending on the range we are operating [6]. However, in our case we could use it. A DFB laser also can be used, working in a saturation point and modulating its adiabatic chirp for changing the wavelength. However it could give a high residual amplitude change.

In order to make an entire up-down design, first we have focused to the SSB optical VCO. The objective is to try the three VCO architectures and then decide which one is more convenient. But first of all we will focus on the first one.

The loop filter will be a standard Proportional-Integral filter. It is shown in Figure 91.

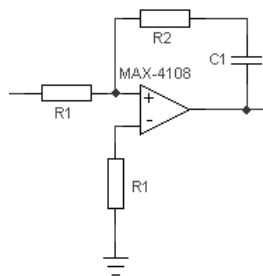


Figure 91: PI filter proposed.

#### A8.2.4.1 Simulations

Two sets of simulations were run. First of all, departing from the theoretical equations that came from loop linearization, we introduced it into Matlab, for numerical analysis. While these simulations were running, we build a VPI model and characterized the optical VCO model, and, after that, we implemented a VPI module for the full loop.

##### A8.2.4.1.1 Theoretical model

In order to see the analog approach performances, we have built the theoretical model equations, and introduced them in Matlab for numerical analysis. The transfer function, after loop linearization, can be expressed as:



$$H_S(S) = \frac{K \cdot K_p \cdot S + K \cdot K_i}{(1 + K \cdot K_p)S + K \cdot K_i}; \quad K = 8\pi K_{LO} \mathfrak{R}^2 R_L^2 P_S P_{LO}; \quad T = \frac{1 + K \cdot K_p}{K \cdot K_i}$$

where  $K_{LO}$  is the sensitivity of the optical VCO module (Hz/V),  $\mathfrak{R}$  is the photo-detector's responsivity,  $R_L$  is the load impedance,  $P_S$  is the received optical power,  $P_{LO}$  is the local oscillator optical power,  $K_p$  is the proportional gain of the loop filter,  $K_i$  is the integral gain of the loop filter, and  $T$  is the time constant of the system.

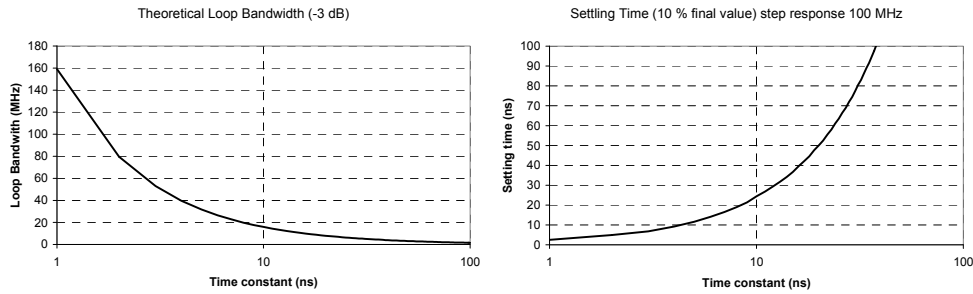


Figure 92: -3dB loop bandwidth (left), and settling time for a 100 MHz step response (right), as a function of the system's time constant

From this model, we evaluated the loop delay impact. The conclusion is that when loop delay is of the order of the time constant, then system performances dramatically decrease. This is shown in Figure 93, where the settling time at 10% for a low frequency step (100 MHz) was used as a measure of the performances of the loop.

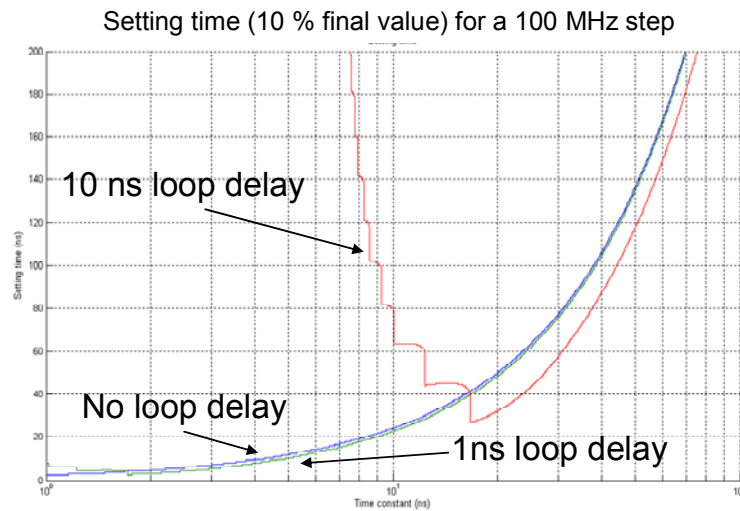


Figure 93: loop delay impact on loop setting time, for 10 ns and 1 ns loop delay.

A8.2.4.1.2 VPI model

While the theoretical model numerical analysis was running, we were implementing a VPI model for that analog approach. A schematic is shown in Figure 94.

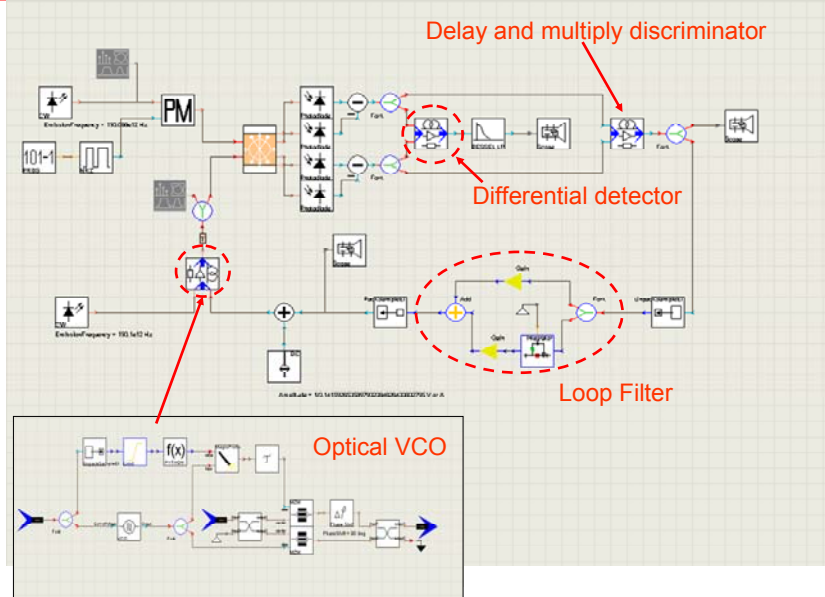


Figure 94: Schematic used in VPI simulations

The first simulations were for characterizing the different modules of the AFC loop. Precisely we did it for the optical VCO and the frequency discriminator.

Regarding the optical VCO, it was implemented by using 2 mach-zehnder modulators, with 30 dB ER, and biasing them at a null of its transfer function. Then, both were driven by the electrical VCO output, but with a 90° phase difference. After some runs, we obtained an optimal working point. At that point the optical VCO output power was of -9 dBm, with -12 dBm at the main component, and -34 dBm on the harmonic with more power (it was the optical carrier). The screenshots corresponding to these data, are shown in Figure 95.

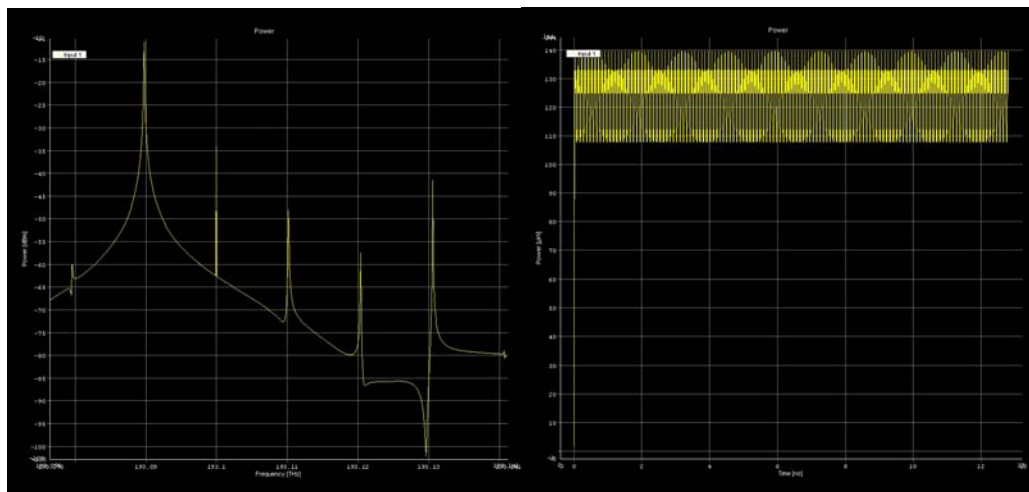


Figure 95: (left) optical spectrum at the output of the optical VCO. (right) the same signal in time domain.

Next we characterized the performances of the frequency discriminator. In Figure 96 four curves displaying its behaviour are shown. As we will see when we will talk about the loop implementation, for practical reasons we decided to use a 100 ps delay, which will allow us to work within a range of  $\pm 2$  GHz.

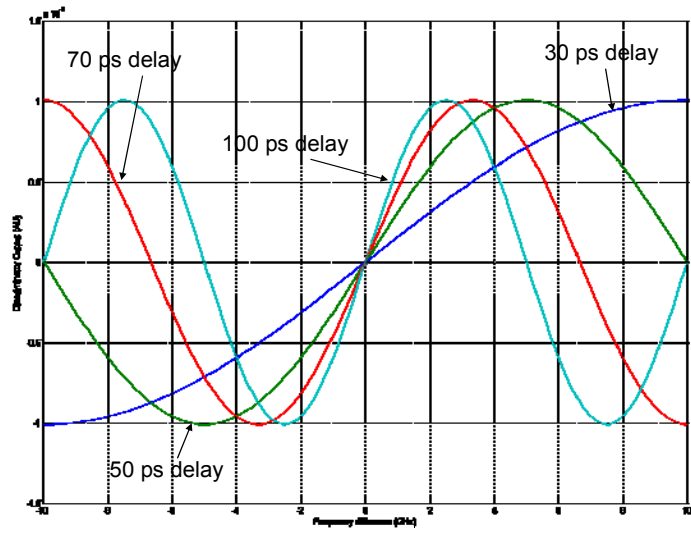


Figure 96: Frequency discriminator output as a function of the frequency difference between LO and received signal.

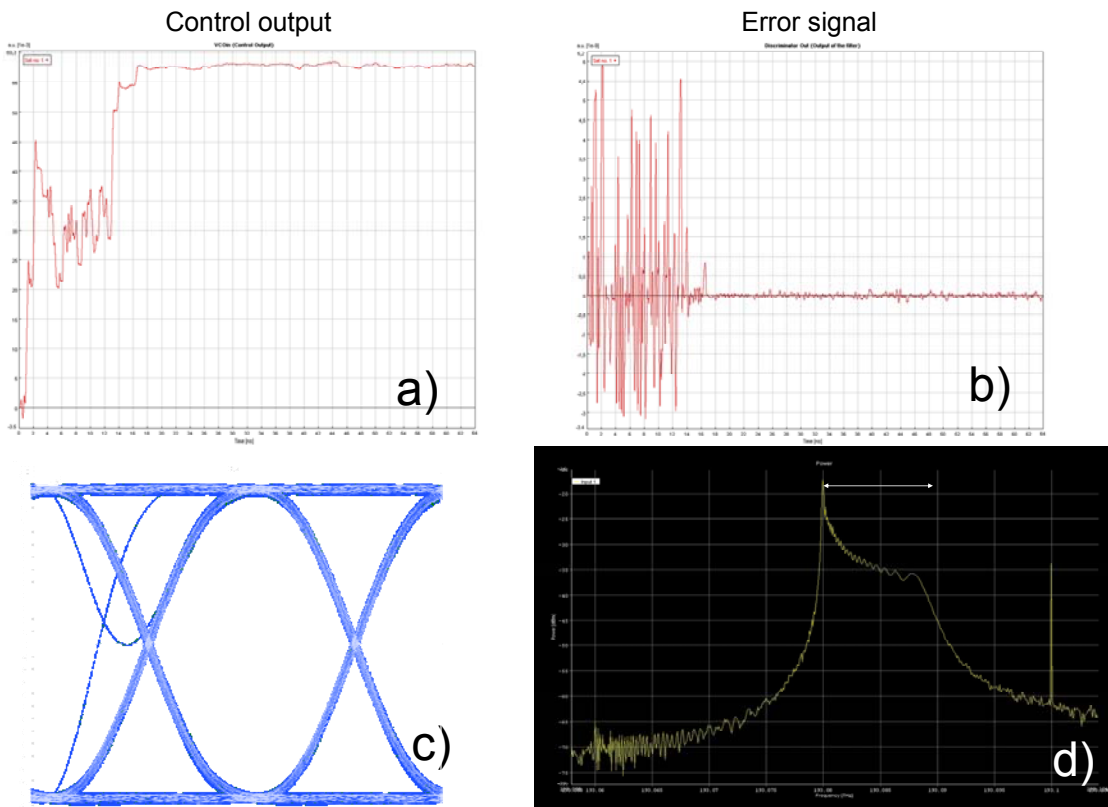


Figure 97: Output signal of the PI control (a), error signal (b), eye-diagram (c), and spectrum of the optical VCO output power when locking frequency (d).

After characterizing and optimizing such modules, we run several simulations of the loop. The general parameters where:



- Bitrate 10 Gbps
- DPSK modulation format
- 10x64 bit time window
- First order loop  $T \approx 3$  ps
- 2 GHz frequency step

As a first result, we obtained the inset figures displayed in Figure 97. There we can see the output signal of the PI control, the error signal (which starts ringing and finally is minimized), the data eye-diagram once demodulated, and a spectrum of the optical VCO output power.

We also evaluated the phase noise impact to the frequency control. We evaluated it in a range of values for common lasers. As we expected, it introduces a residual error, with gaussian statistics, that cannot be tracked nor compensated at all. The variance of such error is proportional to the laser linewidth, as we could expect.

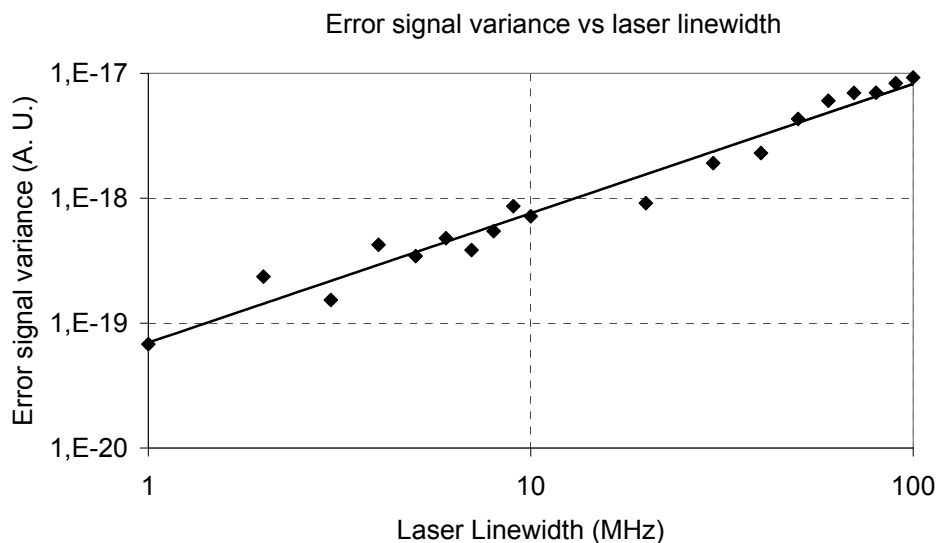


Figure 98: Error signal variance as a function of the laser linewidth

#### A8.2.4.2 Loop Implementation

Regarding the loop implementation, we have identified all main components. Figure 99 shows a schematic of the overall loop. Unfortunately, some of the components (like the analog multipliers) could not be bought in time, so we only characterized the ones we had. Another exchange between both institutions will lead to a prototype of such loop.

First of all, we characterized the filters after the RF 90° hybrid and that electrical hybrid. Please note that the electrical filters placed at each branch of the hybrid must have the same response. Results are shown in Figure 100 and Figure 101. In Figure 100, we can see the results of the electrical hybrid, which is the main limit for the tracking range of the loop. Taking a look at both, magnitude and phase difference responses, the range of operating frequencies are from 2 GHz to 4 GHz. That is the main reason why after the amps located at each output branch, a bandpass filter is placed.

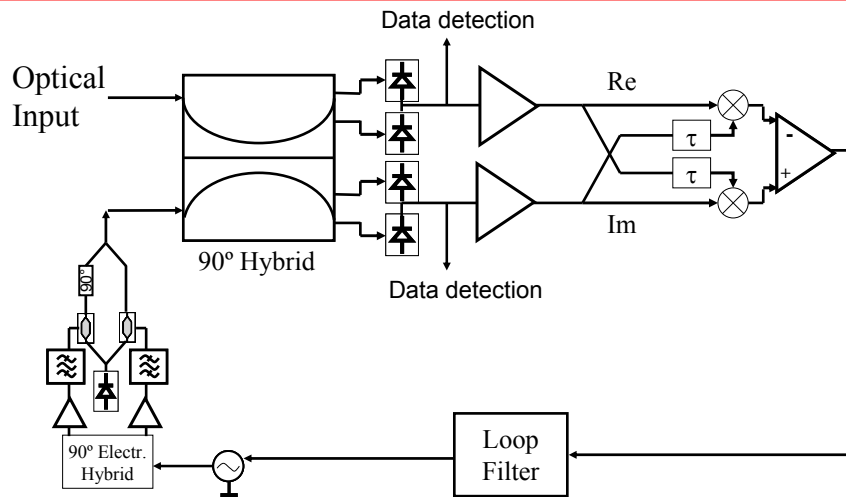


Figure 99: Schematic to be implemented

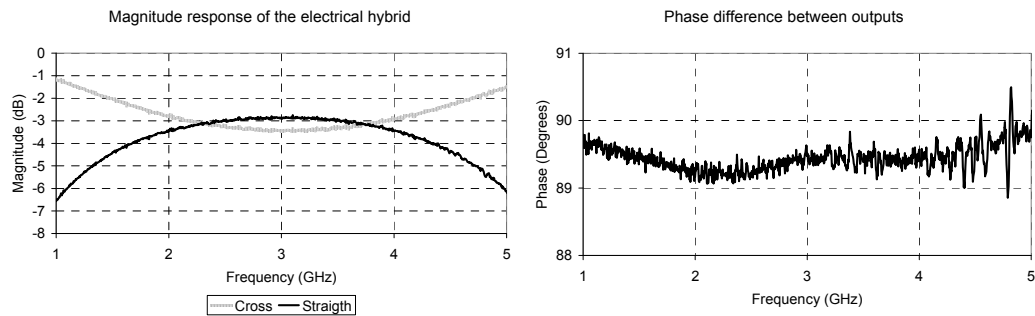


Figure 100: Magnitude response (left) and phase difference response (right) of the 90° electrical hybrid

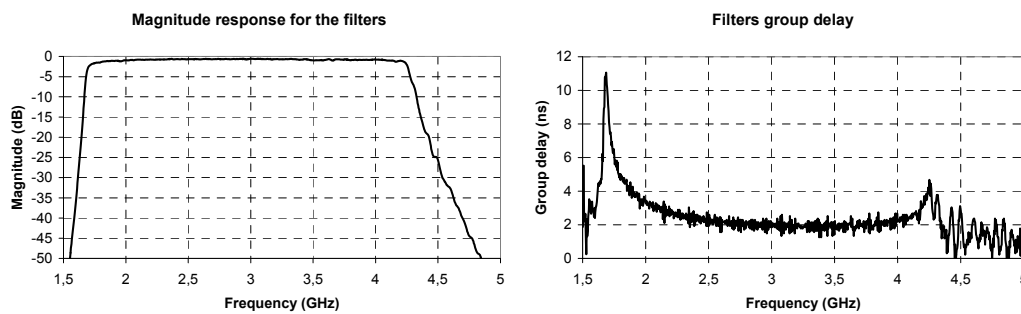


Figure 101: Magnitude (left) and group delay (right) responses for the filters placed at each branch of the 90° hybrid.

With these components and the IQ modulator, we made a first implementation of the optical VCO. Results are shown in Figure 102. For obtaining that figure, we activated the max-hold function and tuned the electrical VCO, for covering the full range of that optical VCO. Taking a look at Figure 102, we can see that such optical VCO, has a residual amplitude modulation, with a slope of 3 dB. Also, when approaching to the limit of  $\pm 4$  GHz a high peak appears at the opposite side of the spectrum. This peak corresponds to a worst case condition, and is 12.7 dB below the principal component.

**Max hold function for the output spectrum of the optical VCO**

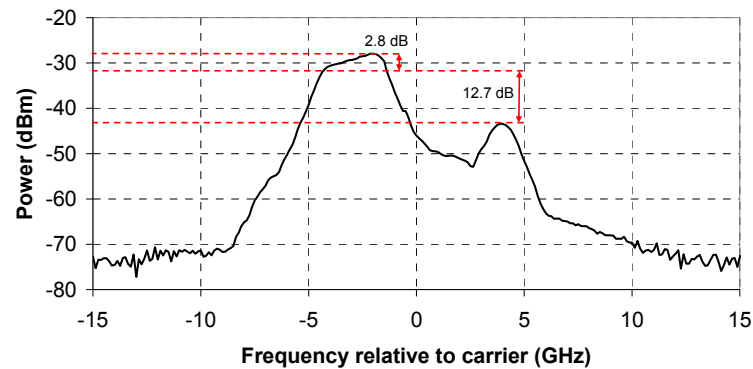


Figure 102: Max hold function for the output spectrum of the optical VCO.

With all these data, we can now compare to the other optical VCO approaches. Results are shown in Table 4. For the tunable laser source, we display results obtained by [6], from a GCSR laser, model NYW 30-009 from ALTITUN. For the DFB laser approach, we retrieved data obtained from measurements carried out with a Panasonic LNFE03YBE1UP at UPC premises.

**Table 4. Comparison between possible optical VCOs.**

	Linewidth	Tuning speed	Tuning range	Freq. slope	Residual Amp. change
SSB-IQ mod.	100 kHz	10 MHz	2 GHz	260 MHz / V	2.8 dB
GCSR	25 MHz	100 MHz	18 GHz	320 MHz / V	0.1 dB
DFB	1 MHz	1 GHz	-	1.4 GHz / V	7.4 dB

#### A8.2.4.3 Proof of concept off-line experiments

In order to see the potential improvement when using the AFC proposed, we carried out some off-line experiments. The setup used is depicted in Figure 103. It is a back-to-back version of a 10 Gbaud RZ-8PSK (30 Gbps) transmission system [7]. Here, the frequency estimation algorithms used where:

- Simple linear regression
- Feedforward version of the feedback loop
- Algorithm proposed in [3]

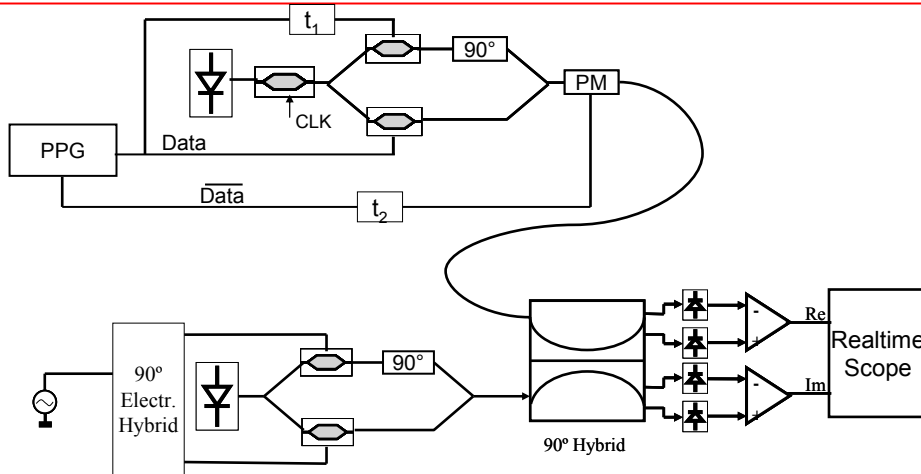


Figure 103: Experimental setup

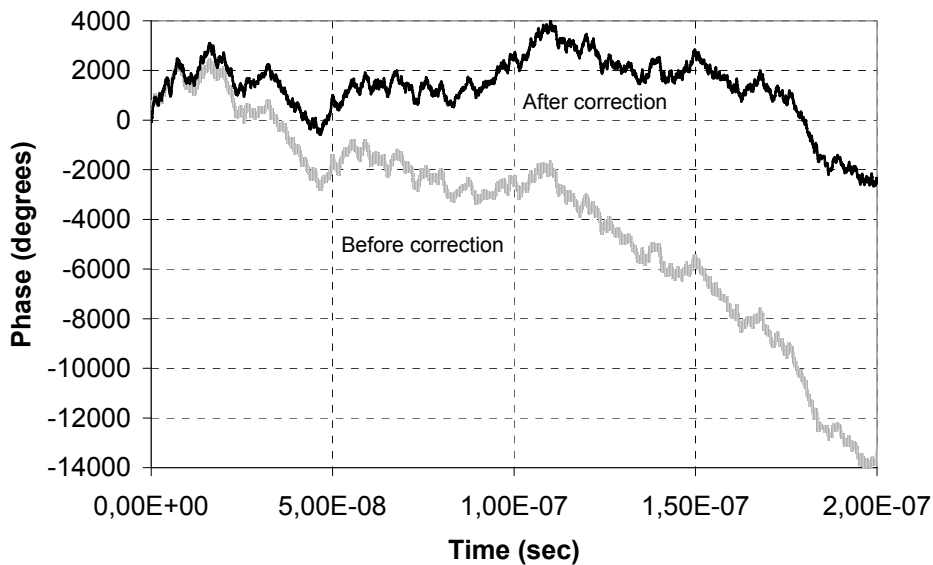


Figure 104: Received phase before and after linear regression correction

In Figure 105, we can see the estimation results. We compared between 4 different cases:

- No frequency difference
- 3 GHz of frequency difference
- 3.5 GHz of frequency difference
- 3 GHz of frequency difference and 10 dB side-lobe suppression ratio

There, we can see that for no frequency difference, both methods, linear fitting and the delay-and-multiply, work quite well, whereas the proposed in [3] is detecting the frequency difference corresponding to the sidelobe.

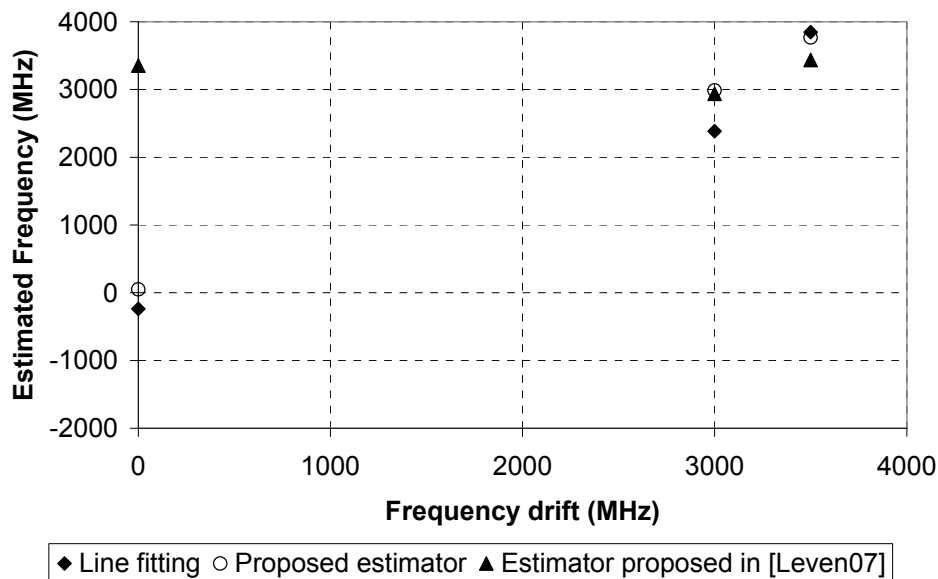


Figure 105: Estimated frequency vs frequency drift

### 8.2.5 References

- 1 F. D. Natali, "AFC Tracking Algorithms," IEEE Transactions on Communications, vol. 32, no. 8, Aug. 1984.
- 2 R. Noe, W. B. Sessa, R. Welter, L. G. Kazovsky, "New FSK Phase-Diversity Receiver in a 150 Mbit/s Coherent Optical Transmission System," IET Electronics Letters, vol. 24, no. 9, Apr. 1988
- 3 A. Leven, N. Kaneda, K. Ut-Va Koc, "Young-Kai Chen, Frequency Estimation in Intradynne Reception," IEEE Photonics Technology Letters, vol. 19, no. 6, Mar. 2007
- 4 L. Li, Z. Tao, S. Oda, T. Hoshida, J. C. Rasmussen, "Wide-range, Accurate and Simple Digital Frequency Offset Compensator for Optical Coherent Receivers," in Proc. OFC08, paper OWT4.
- 5 V. Ferrero, S. Camatel, "Optical Phase Locking techniques: an overview and a novel method based on Single Side Sub-Carrier modulation," OSA Optics Express, vol. 16, no. 2, Jan. 2008.
- 6 V. Polo, "Contribution to the dynamic tuning of tunable laser sources for modulation and optical packet routing in WDM and access networks," Universitat Politècnica de Catalunya Ph. D. Thesis, 2006.
- 7 R. Freund, D.-D. Groß, M. Seimetz, L. Molle, C. Caspar, "30 Gbit/s RZ-8-PSK Transmission over 2800 km Standard Single Mode Fibre without Inline Dispersion Compensation," in Proc. OFC08, paper OMI8.

### 8.3 Transmission performance of GbE transmission in wide area networks (FUB, ISCOM)

Gigabit Ethernet (GbE) transmission is evolving to become an end-to-end technology spanning across Local Area Network (LAN), Metropolitan Area Network (MAN) and Wide Area Network (WAN), with several impacts also in the backbone segment. Spreading of Ethernet technique in wider and wider networks will have to take into account photonics switching aspects, typical of backbone networks, and in particular of the Wavelength Division Multiplexing (WDM) technique. In order to verify the suitability of GbE transmission over wide area networks we investigate on the transmission performance of GbE links. ZE GbE was introduced to achieve optical networks with links shorter than 70 km, but when we assume point-to-point optically amplified links the maximum transmission distance is limited

by physical impairments as the reduced signal to noise ratio and distortions due to the saturation gain caused by the burst nature of Ethernet transmission.

In this report we show experimental results on GbE transmission with EDFA optical amplification in different configurations for a maximum distance of 350 km, and we also include the All Optical Wavelength Conversion.

In Figure 106 we report the three experimental set-ups. In particular, in Figure 106(a) we have a GbE transmission in a link 200 km long when the Optical Amplifier (OA) is located after 100 km. In Figure 106(b) the OA is located near the transmitter and the link is 150 km; in this case, an Optical Filter is deployed in order to reduce the ASE contribution. In Figure 106(c) two EDFAs and an Optical Filter are deployed, achieving a transmission over a link 350 km long.

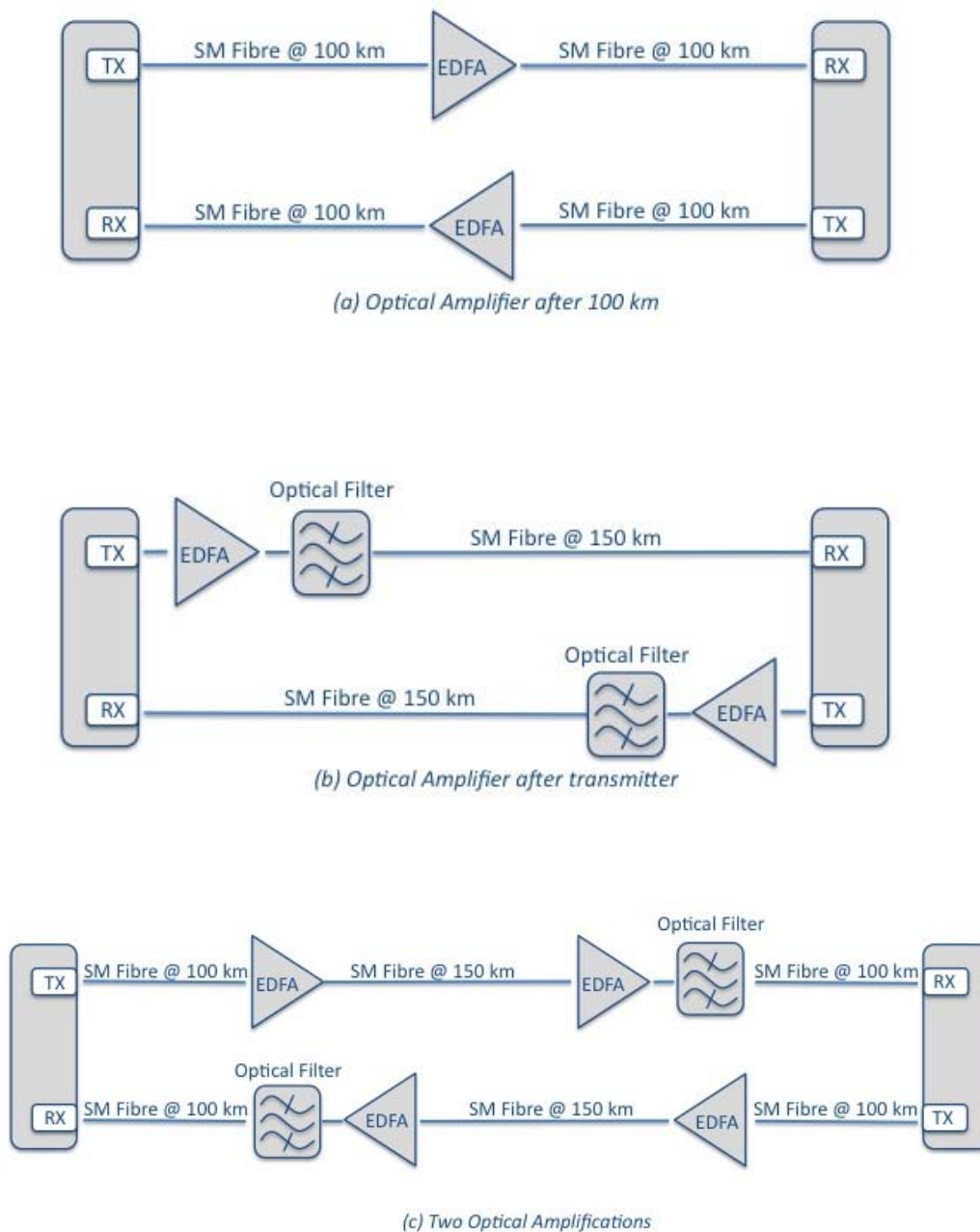


Figure 106: Experimental Setup



In Figure 107 we report the Throughput vs Input Receiver Power for a 200 km link, when the OA is located after 100 km. The sharp step behaviour of curve is clearly shown and it is due to the synchronization process that requires a minimum input power of signal. When the synchronisation starts the transmission performance is perfect and the Analyzer does not reveal any data loss for input power higher than -25.4 dBm, also for long time measurements, showing an error probability close to zero.

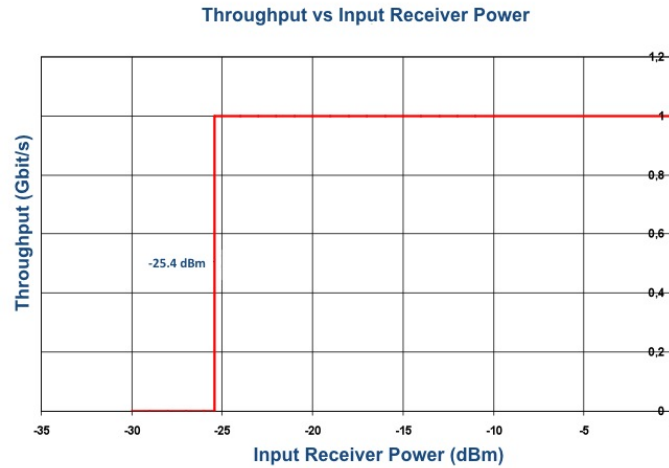


Figure 107: Throughput vs Input Power in a link 200 km long

In Figure 108 we report the Throughput vs Input Receiver Power when the OA is located after the transmitter. In this case an optical filter is necessary to limit the ASE contribution. Also in this case a sharp step behaviour is shown.

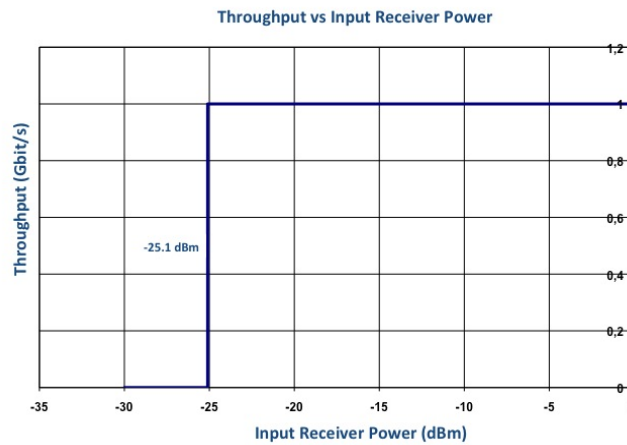


Figure 108: Throughput vs Input Receiver Power in a link 150 km long

In Figure 109 we report Throughput vs Input Receiver Power when two OAs and an optical filter are deployed in a link 350 km long (as shown in Figure 106(c)).



Figure 109: Throughput vs Input Receiver Power in a link 350 km long

In all measurements, when the Input Power at the receiver is about -25 dBm, the links and the interfaces go up and the throughput is equal to 1 Gbit/s. This confirms that GbE transmission is well suitable as transport support also for long distance and this enables GbE to operate as carrier technique.

To verify the compatibility of GbE transmission with backbone all optical processing techniques we experimentally investigate on the All Optical Wavelength Conversion (AOWC) of GbE signals. Details of this activity, that includes some restoration operation and QoS tests, are reported within the Deliverable of WP11. Here we only report some physical aspects and we summarize affirming that AOWC does not induce any floor degrading effects.

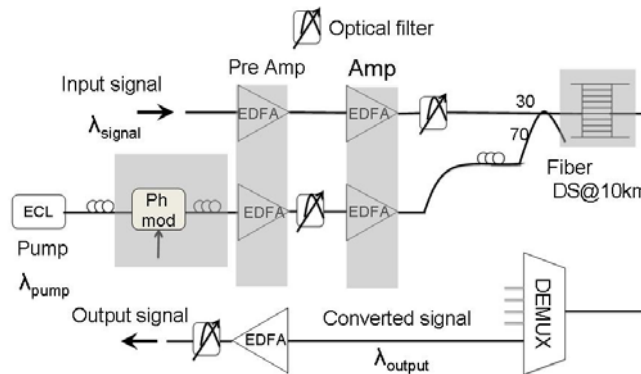


Figure 110: Wavelength converter set-up: Ph Mod phase modulator to control Brillouin effect.

The AOWC is based on the FWM in a DS fibre and the scheme is reported in Figure 110. The input signal ( $\lambda_1=1553.30$  nm) is amplified by a dual optical amplificatory stage and it is mixed inside the DS fiber (10 km long) with the amplified pump coming from an external cavity laser (ECL) ( $\lambda_p=1553.76$  nm). The signal power at the DS fiber input is 6 dBm and 7.6 dBm for signal and pump respectively. The output wavelength is selected by means of the optical demultiplexer (DEMUX) that permits to switch between  $\lambda_1$  and the converted  $\lambda_2$ .

In Figure 111 we report the optical spectrum at the output of the DS fiber that shows the signal replicas generated with high efficiency by means of the FWM effect; in our experiment we use the wavelength at 1554.12 nm for  $\lambda_2$ . The efficiency of such a process can be much

high and it depends on the pump power; furthermore, it is a wide bandwidth effect since it can be achieved in all the C bandwidth.

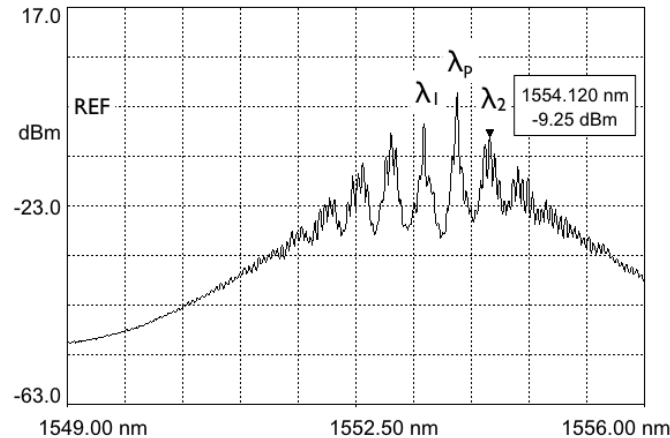


Figure 111: Optical spectrum at the DS fiber output. Resolution: 0.05 nm, 10.0 dB/div

## 8.4 Reliability Analysis of Optical Modules for Future Optical transmission Networks (Ericsson, KTH)

Reliability of optical networks depends on reliability of components. This in turn strongly depends on the detailed design of the structures, processes and technologies used to fabricate them. Reliability testing and investigation must start at the beginning of the design phase to expose any potential weaknesses of the design. This report reviews the reliability testing that was undertaken on an optical PIN Receiver module and subsequent testing for network reliability to expose the failure modes and hence resulted in a redesign of the module. This approach across all components and modules eliminates failure modes early in the design process and ensure long term reliability of the optical network.

### 8.4.1 Introduction

The reliability of the entire communications network is dependent on the reliability of each device used in that network. Even though redundant transmission systems allow higher reliability, the maintenance costs can be minimized if reliable components are used. Investigations carried out on optical devices and modules indicate that they have failure mechanisms that are accelerated by both temperature and moisture. In many of the proposed applications, the devices will be located in environments that are subject to both high temperature and potentially high humidities. Information about the accelerating effect of both temperature and humidity is therefore essential to ensure that the devices are fit-for-purpose.

Reliability in Design and new technologies in optical communications is essential as businesses and consumers expect uninterrupted service and fault free operation. Costs associated with the failure of optical components can be significant. The relative costs of correcting field failures and redesigning are significantly higher than the initial cost of design of the optical component. There is also an additional need to integrate full electronic controls into the earlier designs of simple optical components. Increased complexity and capability, leads to increased failure modes. This paper reviews the reliability testing that was undertaken on an optical PIN Receiver module and on an optical network carrying traffic.



### 8.4.2 Reliability of optical PIN Receiver

The drive to ensure reliable optical networks has resulted in several standards having been defined by Telcordia Technologies. This section highlights the reliability testing undertaken on a PIN Receiver module used in long haul and metro networks and the effect this has had on understanding the failure modes and consequent redesign of the module to eliminate the failure mode. This product design is based upon a PIN photodiode with a low-noise transimpedance amplifier (TIA), which has low power consumption, high sensitivity and high gain [1].

The module were tested for qualification and reliability required by Telcordia GR-468-CORE and MIL-STD-883 demonstrating the performance, reliability and integrity of the device. The tests included mechanical shock, vibration, temperature cycling and high temperature storage testing, solderability, fiber pull, damp heat, low temperature storage and ESD threshold. Electrical and optical performance tests were conducted prior to and after each reliability test. The change in product performance resulting from the environmental exposure was measured and compared with the established acceptance criteria. Complete results of few of the tests, including electrical/optical performance data, environmental conditions, actual test profiles and summary are provided in this paper. These tests were performed in compliance with GR-468-CORE [2], using the test methods and conditions described therein on a subgroup of at least eleven test samples. The test sequence consisted of the detector module reliability tests identified below in Table 5.

*Table 5. Receiver Qualification Details*

<b>Test</b>	<b>Conditions</b>
Mechanical Shock	5 times/axis with TEC 500g, 1.0ms
Vibration	Condition A, 20g, 20 - 2,000Hz, 4 min/cyc, 4cycles/axis
Fiber Pull	1 kg; 3 times; 5 seconds
High Temp. Storage	85°C 2000 Hours
Low Temp. Storage	-20°C 2000 Hours
Temperature Cycling	-40°C to 85°C, 100 Cyc. Pass/Fail 500 Cyc. for Info.
Damp Heat	85°C/85%RH 1000 hrs

The vibration test was conducted on the PIN Receiver samples in accordance with MIL-STD-883, Test Method 2007 Test Condition A. Each test sample was subject to an electrical/optical performance test after which it was exposed to four cycles of vibration per axis, in each of three mutually perpendicular axes. The vibration profile covered the frequency range of 20 to 2000 Hz and was 4 minutes per cycle in duration. Prior to the start of the vibration test, the vibration controller was programmed with the required test profile and a



vibration survey was performed to ensure the vibration level was essentially identical across the mounting surface of the test samples. Once the vibration profile was verified and the fixture was surveyed, the qualification samples were prepared for testing. The vibration was induced into each test sample by mounting them two at a time onto a square test plate. The test plate containing the two test samples were then rotated on the face of the circular adapter plate in order to expose all test samples to the three different lines of force (X, Y & Z).

The mechanical shock test was conducted on the same PIN Receiver samples that had undergone vibration and was performed in accordance with MIL-STD-883, Test Method 2002 as required by GR-468-CORE. Each test samples was subject to an electrical/optical performance test after which it was exposed to five, 500 G, 1.0 ms shock pulses per axis in both positive and negative direction for each of 3 mutually perpendicular axes. This resulted in the application of a total of 30 shock pulses per test sample.

This procedure required that an acceptable shock pulse be established prior to formal qualification testing by mounting an accelerometer to the test fixtures and subjecting that test fixtures to a series of "trial" pulses in order to attain a compliant pulse. Once the number of cushions, proper drop height and charge pressure was determined, the configuration was recorded in the worksheet and a sample waveform was digitally captured to evidence the compliant pulse.

The mechanical shock was induced into each test sample by mounting them onto a square test plate that was, in turn, mounted onto a cube. Three test plates were used for this test, with each plate mounted in a different orientation on the surface of the 8 inch cube. The 3 test plates were then rotated about the cube in order to expose all test samples to the six different lines of force (X1, X2, Y1, Y2, Z1, & Z2).

Once each test samples was exposed to a complete series of shock pulses (30 total) they were returned to the test station for final electrical/optical performance testing.

The mechanical shock and vibration tests performed on a subgroup of 25 devices resulted in a total of three device failures; two occurring in vibration and one occurring in mechanical shock. The occurrence of these device failures does not adversely affect the qualification status of the product since the Telcordia, GR-468-CORE sampling plan allows for 2 failures in any one test when using a sample size of 25.

An extensive evaluation on each of the failed devices was undertaken. In each case, the failed device was subject to failure mode analysis (FMA) that resulted in the establishment of firm corrective action implemented and verified to ensure similar failures would not occur in future production.

The high temperature storage test was conducted in accordance with GR-468-CORE. Each test sample was subject to an electrical/optical performance test after which it was subject to 4000 hours of exposure to at least +85°C. During this test period, the test samples were subject to 5 interim electrical/optical performance tests at the 96, 480, 768, 1032 and 1512 hour marks. Once 4000 hours of exposure were completed, all test samples were subject to a final electrical/optical performance test.

Figure 112 shows the results of the high temperature aging test at 85<sup>0</sup> C performed on the module for over 4000 hours indicating that they had passed as the sensitivity change was within ±0.5 dB.

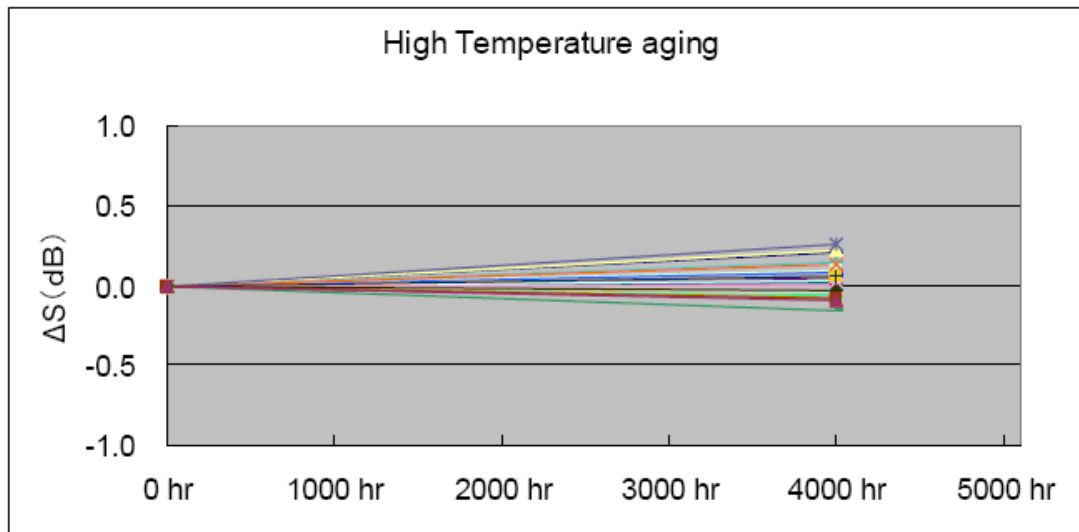


Figure 112: Results from the High Temperature Aging test on the Receiver module.

### 8.4.3 Failure Mode Analysis

The specific findings and corrective actions resulting from the failure mode analysis are described below.

#### A8.4.3.1 Vibration Test Failure 1:

This device failed when a small solder ball had become dislodged due to the vibration from the housing assembly. The solder ball then came to rest inside an internal cavity near the RF connector pin enabling it to short the RF signal to case ground. As a result the following corrective actions have been implemented to prevent future failures. The previous method of attaching components to the housing assembly using an uncontrolled amount of solder has been changed to use “solder preforms”. The use of solder preforms in lieu of solder paste ensures that a necessary and consistent amount of solder is applied to the component/board interface which precludes the formation of solder balls.

#### A8.4.3.2 Vibration Test Failure 2

This device failed as a result of the failure of an alternate PIN diode used within receiver. Failure mode analysis lead to the conclusion that poor metallization on the PIN diode itself resulted in the use of excess bonding force during the application of the bond wire to the PIN diode. The effect of the additional force was to overstress the semiconductor material of the PIN diode in a manner that created a latent defect within the PIN diode that revealed itself later during the vibration test.

#### A8.4.3.3 Damp Heat Test Failure

Damp heat storage testing consists of storing the device in an ambient temperature of 85°C with relative humidity at 85%. To comply with Telcordia GR-1221, uncontrolled environment requirements, the device is stored for a minimum of 2000 hours in this environment. The evaluation of the eleven samples that were tested found that four receivers had failed during the 1000 hours of damp heat exposure required for Telcordia qualification. The failure observed was that the responsivity was lower than as shipped. This signature is consistent



with insufficient light getting to the PIN. Suspected failure mechanism is epoxy used to fix fibre in alignment to the photodiode. The epoxy swelling at the fiber ferrule caused misalignment of the fiber. The package was non-hermetic. The results confirmed that the epoxy fixing process coupled to a non-hermetic package is an inherent weakness in the design.

The shortcomings were overcome with newer designed packages which were hermitically sealed and laser welded, not epoxied. These were tested in the damp heat chamber and passed proving that they will withstand high humidity conditions.

#### **8.4.4 Network Reliability tests**

The receiver module with the above problem and two receiver modules with a new redesign was used in three different transponder cards and tested for test traffic through the cards. Tests show plots relating to the redesigned receiver module having no traffic errors and one plot with a large drop showing traffic errors, thereby affecting the optical network reliability. The plots from data on the network show how the failed component affected network reliability and traffic.

The evidence suggests that the use of the product with the old design placed in uncontrolled environments, especially where they might be exposed to high temperatures and humidity could cause network reliability problems by inducing traffic errors. Hence the new design has been used for both controlled and uncontrolled environment to ensure network reliability.

#### **8.4.5 Conclusion**

Review of the reliability testing on an Optical Receiver module and the subsequent tests in an optical network has been undertaken in his paper. The review has highlighted some of the design issues and failure modes that were exposed due to the Reliability testing. This caused traffic errors to be induced in the optical network in which this module was used. This had resulted in a redesign of the module earlier on the design process and showed no traffic errors in the network with the redesign of the module. This approach across all components and modules ensures long term reliability of the optical network.

Work will continue between KTH and Ericsson in comparing the FIT rate for the above receivers and also splitters used in transmission systems and this will be used to review and estimate the reliability of various transmission systems.

#### **8.4.6 References**

1. D. O. Caplan, "Laser communication transmitter and receiver design", J. Optical Fiber Communication. Rep. 4, 225 (2007).
2. Generic Reliability assurance requirements for optoelectronic devices used in telecommunications equipment," Bellcore, GR-468-CORE, Dec. (1998).



## 9. Conclusions

This document has reported the progress that has been achieved during the first year of VCE-T. The integration strategy that has been followed has first been outlined. The central feature of this strategy has been the formation of Focus Groups to investigate separately research topics which are common among several VCE-T partners. The Focus Groups which are currently active relate to (a) key issues on 100 Gb/s transmission, (b) optical signal regeneration, (c) signal amplification, and (d) monitoring. Beside the activities of these Groups though, there have been several other joint activities within Y1 of the project, on topics spanning from device work through transmission to reliability analysis studies.

It is anticipated that a larger number of joint activities will be initiated within the second year of the project. An early indication of this serves the fact that there have already been a number of applications for mobility actions submitted to the WP management. These mobility actions are on the topics of signal regeneration and unrepeated signal transmission using maximum likelihood sequence estimation algorithms.

It is planned that there will be a further two WP-wide meetings in Year 2. The first of these will take place in summer 2009 and is planned to be collocated with an event that will be attended by several partners (details are to be confirmed), whereas the second meeting will be collocated with the BONE Annual meeting, which again will ensure a large number of attendees. In the meantime, the VCE-T Advisory Board will be monitoring the progress achieved towards integration throughout the year, and will take corrective actions if required. To this end, the Advisory Board will be reviewing the quarterly reports submitted by the various partners, and will discuss any issues either on telephone conferences or via email.



## Table of Figures

Figure 1: Proposed Transmitter design .....	14
Figure 2: Power levels vs coupling coefficient. Circles: Power Level 3, Crosses: Power Level 2, Solid line: Power Level 1, Dashed lines: required quadratic levels relative to Power Level 3.....	15
Figure 3: Basic link model .....	16
Figure 4: BER vs Electrical and Optical filter 3-dB cut-off frequencies for 100 GBps 4-ary ASK.....	16
Figure 5: BER vs OSNR for 100, 160 and 200 Gbps 4-ary ASK.....	16
Figure 6: BER vs Residual Dispersion for 100, 160 and 200 GBps 4-ary ASK (OSNR = 45 dB).....	16
Figure 7: BER vs OSNR for a 128.1 GBps 8-ary ASK utilizing pulses of different temporal widths.....	17
Figure 8: $\log_{10}(\text{BER})$ vs Optical and Electrical filters' 3dB bandwidth for 128.1 GBps 8-ary ASK (OSNR = 45 dB, Pulse Width= 75% Symbol Slot).....	17
Figure 9: BER vs SMF length for 128.1 GBps 8-ary ASK 9 channel system (OSNR = 45 dB, Pulse Width= 75% Symbol Slot). .....	18
Figure 10: Maximum number of spans for different PMD values (source: Acreo).....	23
Figure 11: Maximum reach without intermediate ROADMs for different PMD values (high order PMD, one outcome) (source: TID).....	24
Figure 12: Maximum reach with intermediate ROADMs for different PMD values (high order PMD, one outcome) (source: TID) .....	24
Figure 13: Maximum reach without ROADM in absence of PMD as a function of number of channels and for different launch power per channel. Considering a maximum booster power of +17 dBm (source: POLITO). .....	24
Figure 14: DQPSK Simulation Scheme in VPI Transmission Maker (source: ACREO).....	25
Figure 15: DQPSK Receiver Scheme in VPI Transmission Maker (source: TID).....	25
Figure 16: Optical links with intermediate ROADMs in VPI Transmission Maker (source: TID).....	26
Figure 17: DQPSK Transmitter Scheme in OptSim (source: POLITO). .....	26
Figure 18: DQPSK Modulator Scheme in OptSim (source: POLITO).....	27
Figure 19: DQPSK Receiver Scheme in OptSim (source: POLITO). .....	27
Figure 20: Maximum reach without ROADM in absence of PMD as a function of number of channels and for different launch power per channel. Considering a maximum booster power of +17 dBm (source: POLITO). .....	28
Figure 21: PM-QPSK Simulation Scheme in OptSim (source: POLITO). The UsrLib block in the middle of the layout is a custom block for simulating the 90-degree optical hybrid and the local oscillator. Then, it is followed by four balanced photodiodes. The UsrLib block on the	



right is for simulating the DSP processing of the four electrical signals coming out of the system.....	28
Figure 22: PM-QPSK transmitter Simulation Scheme in OptSim: the four data stream reaching the PM-QPSK modulator. (source: POLITO).....	29
Figure 23: PM-QPSK modulator with the laser source in OptSim (source: POLITO). ....	29
Figure 24: QPSK modulator in OptSim (source: POLITO).....	30
Figure 25: Schematic of a typical optical regenerator based on SPM. ....	33
Figure 26: Illustration of the three possible TF types for the SPM-based regenerator: non-monotonic evolution (A), locally flat evolution (B), or monotonous variation (C).....	33
Figure 27: Definition of the parameters used to parameterize the power TF of the regenerator. Left: Definition of the input ( $ER_{in}$ ) and output ( $ER_{out}$ ) extinction ratios. Right: Example showing these corresponding parameters on a model TF. ....	34
Figure 28: Contour map of a 2R regenerator based on a HNLF with 2.1 dB/km attenuation. ....	34
Figure 29: Effect of dispersion slope on the (a) temporal and (b) spectral profile of pulses at the output of the HNLF. ....	35
Figure 30: Power TFs for varying values of S. (a) Point X. (b) Point Y. (c) Point Z. ....	36
Figure 31: Energy yield at P1 in as a function of the dispersion slope.....	36
Figure 32: Set-up of the experimental device .....	37
Figure 33. Comparison of real (left) and simulated (middle) optical output.....	39
Figure 34 Transfer function and the measure of noise reduction (right) .....	39
Figure 35: BTB and propagated BER measurements vs received power for ITU Ch 46 and 54. ....	40
Figure 36. Measured (dot line) and simulated (continuous line) characteristics of the first four replicas of the Comb1 (superior series) and of Comb2 (inferior series).....	40
Figure 37. Different configuration of Comb2 obtained emphasizing via PC4 and PBS the SOP of E2. In the tree cases we take different wavelength for E2 in the surroundings of the maximum efficiency frequency ( $E2= 1531.4, 1533, 1534.5\text{nm}$ ) .....	41
Figure 38. Set-Up used for the experiments. FC first component, HC orthogonal component. Output spectrum (on the right) referred to First Component. ....	42
Figure 39: Noise (on the left) and regenerated signal (on the right).....	43
Figure 40: BER measurements.....	43
Figure 41: Experimental set-up and corresponding channel properties.....	44
Figure 42: Experimental TF obtained for the four channels in both the absence and presence of the interfering channels. The arrows indicate the corresponding operating input powers. Inset graphs detail variations at low input powers (logarithmic scale). Input powers measured at the fiber inputs.....	45
Figure 43: Single- and multi-channel spectra obtained at fiber output ports X and Y, and output channels (all channels operating at nominal input operating powers).....	46



Figure 44 . BER measurements of the four channels in the absence and presence of interfering channels. The additional BER curve for Channel 3 corresponds to the degraded signal case. Corresponding eye diagrams of the input degraded and output regenerated data stream.....	47
Figure 45: 2R unit set- up and optical spectrum at the DS output. ....	49
Figure 46 : Clock Recovery Unit set-up. ....	49
Figure 47: Re-Timing Unit set-up.....	50
Figure 48: Comparison between experimental transfer function, dotted line, of Ch. 47 with simulation, continuous-line. Noise compression in a Non-Return-to-Zero 10 Gbit/s coded signal .....	51
Figure 49: BTB and propagated BER measurements vs received power for ITU Ch 46 and 54. ....	51
Figure 50: a) Clock recovered at the output of SOA2. b) Retiming of the incoming signal. ..	52
Figure 51. Schematic diagram of the operation of a MZI-based 2R regenerator. ....	52
Figure 52. Relative transmission of the MZI upper output port as a function of the induced phase shift in the SOA (black line). The insets schematically show how input (I/P) amplitude noise is ‘squeezed’ on the MZI output (O/P) port when the induced phase shift is close to pi radians. ....	53
Figure 53. (a) Schematic diagram of ‘push-pull’ MZI operation. (b) The slow recovery of the ‘push’ phase is cancelled by the ‘pull’ phase change, creating a high-bandwidth switching window.....	54
Figure 54: (a) Packaged and pigtailed SOA-MZI optical gate, (b) corresponding motherboard design and (c) twin SOA silicon submounts, (d) packaged and pigtailed prototype device containing four SOA-MZI optical gates on a single photonic chip, (e) corresponding motherboard design and (f) quad array of SOAs used for constructing each double SOA-MZI gate within the chip. ....	55
Figure 55: 2R regeneration with GC-SOA.....	56
Figure 56: RZ to NRZ format conversion.....	57
Figure 60: Values of the tilt curve $T(\lambda, \lambda_{\text{ref}})$ for different lengths of the EDF HE980 for a pumping wavelength of 1480nm. The reference wavelength is $\lambda_{\text{ref}}= 1543.73\text{nm}$ , $P_p=12\text{ dBm}$ and $P_{\text{in}}=0$ and $-10\text{ dBm}$ for each EDF length.....	64
Figure 61: Gain curves at different saturation levels $G_1^{\text{dB}}(\lambda)$ and $G_2^{\text{dB}}(\lambda)$ . $\lambda_{\text{ref}} = 1543.73\text{ nm}$ , $P_p = 12\text{ dBm}$ , $P_{\text{in}} = 0\text{ dBm}$ for $G_1^{\text{dB}}(\lambda)$ and $-10\text{ dBm}$ for $G_2^{\text{dB}}(\lambda)$ . ....	66
Figure 62: a) $G_0(P_p, L)$ and $P_{\text{sat}}(P_p, L)$ and b) $\alpha(P_p, L)$ from the experimental measurements for 2, 10 and 20 m of EDF at $P_p = 6, 12, 20\text{ dBm}$ and reference wavelength $\lambda_{\text{ref}} = 1543.73\text{ nm}$ . ....	66
Figure 63: Comparison of experimental gain measurements, using (1) and Extended BBM (6) for 15 m EDF a) and 2 m EDF b) at different pump power and input signals.....	67
Figure 64: (H. Nakaji et al. / Optical Fiber Technology 9 (2003) 25–35) High speed ACG controller in EDFA 1480nm pumped (left) and 980nm pumped (right).....	68
Figure 65: (C.-L. Zhao et al. / Optics Communications 225 (2003) 157–162).....	69
Figure 66: (Awaji, Furukawa, Wada, Kong, Chan, Man, ONDM2007 Proc) .....	69



Figure 67: Test-bed set up.....	70
Figure 68: Transient effects vs. pump power.....	70
Figure 69: Experiment Set-Up. ....	70
Figure 70: GC Output with different values of driver current. ....	71
Figure 71: Experimental BER for the Raman and EDFA amplification, the back to back situation is also displayed. The lines are visual guides.....	71
Figure 72: Bit sequence at the receiver: Left – Raman amplification, right– EDFA amplification. The vertical scale is arbitrary and the horizontal scale is 500 ns /div. ....	72
Figure 73: Conceptual block diagram for CDM .....	73
Figure 74: Block diagram for CDM.....	75
Figure 75: Two kinds of interferometer arrays: (a) active MZI and (b) multi-branch configuration. ....	75
Figure 76: The average power as a function of accumulated chromatic dispersion (CD) for 40Gb/s NRZ data. The CDM configurations are based on (a) active MZI and (b) multi-branch.....	75
Figure 77: The average power as a function of accumulated chromatic dispersion (CD) for 40-Gb/s RZ50 data. The CDM configurations are based on (a) active MZI and (b) multi-branch. ....	76
Figure 78: The average power as a function of accumulated chromatic dispersion (CD) for 40-Gb/s CSRZ data. The CDM configurations are based on (a) active MZI and (b) multi-branch. ....	77
Figure 79 : View of the OPM prototype .....	79
Figure 80 : Association of a multi-channel power & wavelength monitor with a single channel in-band OSNR monitor. ....	80
Figure 81 : Schematic of the OPM prototype modification to implement in-band OSNR measurement.....	81
Figure 82 : Experimental set-up for the characterization of the in-band OSNR monitoring with the OPM. ....	81
Figure 83: Evolution of the transmission, PDL and DGD curves as a function of the grating length.....	84
Figure 84: Comparison between experimental and simulated evolutions for a 1 cm long $\pi$ -shifted FBG. ....	84
Figure 85: PDL and DGD of twisted FBG (simulation) .....	85
Figure 86: Transmitted spectrum, PDL and DGD evolutions as a function of the transverse force value.....	86
Figure 87: Schematic of a generic off-line receiver.....	87
Figure 88: Schematic of a digital real-time loop.....	88
Figure 89: Scheme of the proposed analog frequency estimation loop .....	88
Figure 90: Diagram of the optical VCO.....	89



Figure 91: PI filter proposed. ....	89
Figure 92: -3dB loop bandwidth (left), and setting time for a 100 MHz step response (right), as a function of the system's time constant.....	90
Figure 93: loop delay impact on loop setting time, for 10 ns and 1 ns loop delay. ....	90
Figure 94: Schematic used in VPI simulations .....	91
Figure 95: (left) optical spectrum at the output of the optical VCO. (right) the same signal in time domain.....	91
Figure 96: Frequency discriminator output as a function of the frequency difference between LO and received signal.....	92
Figure 97: Output signal of the PI control (a), error signal (b), eye-diagram (c), and spectrum of the optical VCO output power when locking frequency (d).....	92
Figure 98: Error signal variance as a function of the laser linewidth .....	93
Figure 99: Schematic to be implemented .....	94
Figure 100: Magnitude response (left) and phase difference response (right) of the 90° electrical hybrid.....	94
Figure 101: Magnitude (left) and group delay (right) responses for the filters placed at each branch of the 90° hybrid.....	94
Figure 102: Max hold function for the output spectrum of the optical VCO. ....	95
Figure 103: Experimental setup .....	96
Figure 104: Received phase before and after linear regression correction .....	96
Figure 105: Estimated frequency vs frequency drift.....	97
Figure 106: Experimental Setup.....	98
Figure 107: Throughput vs Input Power in a link 200 km long.....	99
Figure 108: Throughput vs Input Receiver Power in a link 150 km long.....	99
Figure 109: Throughput vs Input Receiver Power in a link 350 km long.....	100
Figure 110: Wavelength converter set-up: Ph Mod phase modulator to control Brillouin effect.....	100
Figure 111: Optical spectrum at the DS fiber output. Resolution: 0.05 nm, 10.0 dB/div.....	101
Figure 112: Results from the High Temperature Aging test on the Receiver module.....	104